Merck

Progress in Inorganic Thin Films

Introduction

Richard Sullivan, Ph.D.
Global Product Manager
- Materials Synthesis

Welcome to *Material Matters*™ 16.1, which presents significant advances to materials for inorganic thin films and their applications. This issue discusses critical attributes and process optimization of two-dimensional and thin-film materials and highlights their applications in electronic displays, solar cells, antipathogenic coatings, and additive manufacturing.

In our first article, **Professor Hyun Jae Kim (Yonsei University, South Korea)** and colleagues relate the current state and development challenges of display backplane technology. They review the effect of incorporating various oxide thin-film materials and solution-processing techniques on device performance of oxide semiconductor thin-film transistors (TFTs) compared to current vacuum processing techniques. The ability to improve oxide semiconductor TFTs by optimizing structural engineering parameters is also considered in this review article.

Ever since the discovery of the extraordinary properties of single-layer graphene, researchers have strived to identify the next two-dimensional (2D) material to replicate or improve graphene's performance. **Dr. H. S. S. Ramakrishna Matte (Centre for Nano and Soft Matter Sciences, India)** and colleagues overview a novel class of materials known as inorganic graphene analogs. Facile solution processing parameters for thin-film synthesis are also reviewed for applications in flexible electronics, energy storage, and sensors.

Prof. Yabing Qi (Okinawa Institute of Science and Technology, Japan) and **Dr. Zonghao Liu (Huazhong University of Science and Technology, China)** discuss the recent advances in fabrication techniques for highly promising thin-film photovoltaic (PV) perovskite solar cells (PSCs). Fabrication techniques and engineering strategies that improve power conversion efficiency (PCE) while imparting long-term thermal and operational stability are emphasized to enable scaled-up production and commercialization of perovskite solar modules (PSM).

Additive manufacturing, also known as 3D printing, greatly enables manufacturing customizability. However, access to improved material chemistries is essential to achieving precise layer-by-layer deposition needed to fabricate a new generation of devices. One process under development for inorganic additive manufacturing is cold gas-dynamic spray (CGDS) processing. Here, **Professor Danielle Cote (Worcester Polytechnic Institute, USA)** and colleagues review the cold spray process and its application in antipathogenic coatings, energy (nuclear and battery) coatings, and military and aerospace coatings in repair and manufacturing.

Each article in this publication is accompanied by a list of relevant Sigma-Aldrich materials available from Merck. For additional product information, visit us at **SigmaAldrich.com/matsci**. Please bother us with your new product suggestions, as well as thoughts and comments for *Material Matters*™ at **SigmaAldrich.com/technicalservice**.

About the Cover

Innovative inorganic thin-film materials have already begun to drive sweeping changes in energy, electronics, biomedical, and manufacturing industries where their comparatively low cost and uncomplicated processing techniques allow for facile scaling through printing, coating, deposition, and spraying. With these advanced films, valuable material properties can be achieved while introducing physically conformal and/or mechanically flexible behavior, allowing new types of devices to be imagined. The cover art depicts a flexible thin-film transistor, which enables flexible display technologies. The top-right corner of the cover conveys the advancement of thin films as hierarchical, layered structures with each layer building on the performance level of the previous.

Table of Contents

Articles

Featured Products

Your Material Matters

Bryce P. Nelson, Ph.D.
Materials Science Initiative Lead

Dr. Jaewoo Kim's group recently developed a boron nitride nanotube powder (BNNT) that is lightweight, strong, chemically and thermally stable, and bio-safe. Their continuously operable thermal treatment production method incorporates innovative precursors to enabling synthesis of as much as a ton of material per year while also being cost-competitive to other production methods.[1–2]

Two purities of BNNT produced using this method are now available from Merck, **912085** (90%) and **919500** (80%). The outer diameter of these materials is 30–50 nm, with an average length of ~10 µm (aspect ratio of 200–330). As compared to higher aspect ratio BNNT, these products are easily dispersed in solvent for facile integration into composites and thin films.

Dr. Kim's group developed a reliable analysis to ensure high purity material. Scanning electron microscopy (SEM) is utilized to map area of BNNT versus other particle impurities. The density of the sample is then used to calculate the weight percent BNNT. The boron:nitrogen stoichiometry based on energy-dispersive X-ray spectroscopy (EDS) product samples was reported in an almost 1:1 ratio, confirming BNNT purity.

These cutting-edge materials can be used in application areas such as electronics, piezoelectrics,[3] energy and catalysis,[4–5] aerospace, and biomedical device development. As an additive for polymer composites, BNNT has been observed by Dr. Kim's group to enhance thermal conductivity by up to a factor of three as compared to conventional filler materials. While a myriad of applications of BNNT are being explored, the potential of BNNT has already been demonstrated for specific applications: separators for secondary batteries with high thermal stability,[6] coatings/materials for hypersonic aircraft,[7] space engineering materials (e.g. space habitats and spacecraft),[8] and membranes for osmotic power generation.[9]

References

(1) Kim, J.; et al. *Acta Materialia* **2011**, *59*, 2807–2813.
(2) Kim, J.; et al. *Materials* **2014**, *7*, 5789–5801.
(3) Kim, J.; et al. US Pat. Appl. No. 16690942 2019.
(4) Kim, J.; et al. *I&EC Research* **2019**, *58*, 20154–20161.
(5) Grant, J. T.; et al. *Science* **2016**, *354* (6319), 1570–1573.
(6) Kaneko, K.; et al. *Carbon* **2020**, *167*, 596–600.
(7) Chen, X.; et al. *Sci. Rep.* **2017**, *7*, 11388.
(8) Misra, A. K.; et al. *J. Aerosp. Eng.* **2013**, *26*, 459–490.
(9) Siria, A.; et al. *Nature* **2013**, *494*, 455.

Name	Cat. No.
Boron nitride nanotubes	912085-500MG
	912085-100MG
	919500-1G
	919500-250MG

Recent Progress in Oxide Semiconductor Based Thin-Film Transistors for Next-Generation Display
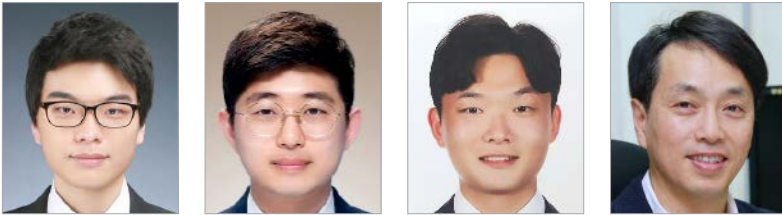
Byung Ha Kang, Kyungho Park, Jong Bin An, Hyun Jae Kim*

School of Electrical and Electronic Engineering, Yonsei University, 50 Yonsei-ro, Seodaemun-gu, Seoul 03722, Republic of Korea
* Email: hjk3@yonsei.ac.kr

Introduction

At the same time that the 3rd industrial revolution gave rise to the current 4th industrial revolution of information and communication technology, display technology rapidly developed from cathode-ray tubes (CRTs) to flat panel displays (FPDs) that use liquid crystal displays (LCDs) and organic light emitting diode (OLED) displays. Recently, the realization of immersive ultra-high resolution for augmented/virtual reality (AR/VR) and flexible, foldable, stretchable, and wearable capabilities are the predominant trends in display research and development.

To fully realize ultra-high resolution and flexible display technology, further development of backplane technology will be required. Because the thin-film transistor (TFT), which acts as a switch to control each pixel, is a crucial component of the backplane, the characteristics, performance, quantity, process conditions, and substrate have a direct effect on display resolution and flexibility. Generally, there are three types of TFTs applied to the display backplane, and they can be classified based on the active layer of material. The main TFT types are amorphous silicon (a-Si) based TFTs, low temperature polycrystalline silicon (LTPS) based TFTs, and oxide semiconductor based TFTs. So far, a-Si based TFT and LTPS based TFT have mainly been used for display backplanes. The relatively low (0.5–1 cm^2/Vs) field effect mobility of a-Si based TFT has led to the introduction of LTPS (a crystallized a-Si fabricated with an excimer laser. This improves mobility to 10–200 cm^1/Vs, making high-resolution possible. While an improvement, these TFTs are still difficult to apply to flexible displays. Flexible displays require a plastic substrate with a low glass transition temperature due to the difficulty in controlling grain boundaries, low large-area uniformity, and high process temperature. Oxide semiconductor based TFTs such as indium gallium zinc oxide (IGZO) were developed in 2004, offering a potential solution to the limitations. The IGZO TFT has advantages such as high mobility (~10 cm^2/Vs) despite its amorphous state, high uniformity over a large area, low leakage current (low power consumption), and high transparency (> 80%) in the visible light region.[1-3] Consequently, IGZO TFTs were used in commercialized LCD backplanes in 2012 and OLED display backplanes in 2013.[4]

In line with the development of OLED displays as a mainstream component of FPDs, oxide semiconductor based TFTs have also evolved to become an essential element of display backplane technology. Furthermore they are expected to become the basis for micro-light emitting diode (μ-LED) displays, quantum nano emitting diode (QNED) displays, and for many next-generation displays, such as immersive, free-form, transparent, and ultra-large displays. Various studies have been conducted to develop ultra-high resolution and flexible displays based on oxide semiconductor TFTs during the last several years. Therefore, we will review recent studies for achieving flexible oxide based TFTs, including both high mobility for ultra-high resolution and low-temperature process. Each subject will be divided into vacuum-processed and solution-processed TFTs.

Research on High-Performance Oxide Semiconductor Based TFT for Immersive Display

As previously mentioned, the display industry is gradually improving the resolution and frame speed of displays to better support immersive content. To satisfy the performance requirements of a display with a resolution of Super Hi-Vision (7,680 × 4,320) and a frame rate of 240 Hz, TFTs with a minimum mobility of 30 cm^2/Vs or higher are required.[5-6] However, the mobility of commercialized IGZO TFTs is around 10 cm^2/Vs, which limits implementation of high-performance displays.[7-8] Currently, various studies are underway to improve the mobility of oxide based TFTs and overcome this limitation.

In general, oxygen vacancies in the oxide semiconductor supply carriers that enable effective charge transport. To improve the electrical characteristics of TFT, the concentration of these vacancies must be optimized. In 2016, Wang et al. adjusted the deposition process parameters of tin-doped zinc oxide (TZO) to control the oxygen vacancy concentration, resulting in improved mobility. This method was conducted by adjusting the oxygen partial pressure of the plasma to 0%, 10%, 20%, and 30% during the sputtering process. A TZO TFT fabricated under 0% oxygen partial pressure produced excess carriers due to a number of oxygen vacancies in the active layer. However, by gradually increasing the oxygen partial pressure, they showed improved transfer characteristics with an on/off ratio of more than 10^7 and a subthreshold swing (SS) of about 0.3 V/dec on average. Among them, a TZO TFT fabricated at 10% oxygen partial pressure showed a low off current of 3 pA, an on/off ratio of 2×10^7, SS of 0.33 V/dec, and high mobility of 66.7 cm^2/Vs. As the oxygen partial pressure increased, the interface-state density was reduced, and the electrical properties were improved due to suppression of excess carriers and a decrease in the surface roughness.[9]

In a study to control oxygen vacancy, a method to control cation doping and deposition process parameters was used. A typical method for controlling properties through cation doping uses a material with high standard electrode potential (SEP) compared to metal ions in an oxide semiconductor. Candidate groups with high SEP include Mg, Sr, Y, Zr, Ba, Hf, and Nd.[10-15] In 2015, Peng et al. reported improved electrical characteristics by doping neodymium, which has a high standard electrode potential, into indium oxide (In_2O_3) where excess carriers exist. Nd is a material with a strong binding force with oxygen (703 kJ/mol) and has the advantage of effectively controlling oxygen vacancies in the active layer. The formed indium neodymium oxide (InNdO) TFT showed a mobility of 20.4 cm^2/Vs under the annealing condition of 450 °C.

The production of solution-processed oxide semiconductor thin films is divided into nanoparticle based methods and metal salt precursor based methods. Nanoparticle based thin films can be formed at low temperature and have excellent device performance, but are not primarily used as display backplanes due to their non-uniformity and low reliability. Therefore, in this review, we focus on the solution-processed oxide semiconductor TFT fabricated using the metal salt precursor based method. However, the metal salt precursor solution-processed oxide semiconductor based TFT must overcome low mobility compared to the vacuum-processed oxide semiconductor based TFTs currently used for commercial display manufacturing.

There are a wide variety of proposed technologies that can be used to overcome the low mobility of solution-processed oxide semiconductor TFTs. The first method is to introduce specific materials as supply carriers to the active layer of TFT to improve mobility.[16] One example is the introduction of potassium superoxide (KO_2) (**Cat. No. 278904**) to improve the mobility of zinc tin oxide (ZTO) TFT based in a solution process. As shown in **Figure 1A**, KO_2 is divided into positive and negative ions in the solution. Potassium cations increase the electron concentration by supplying electrons to the ZTO thin film, and the anions cause a decrease in oxygen vacancies. As a result, the mobility of ZTO TFT treated with KO_2 increased from 5.57 cm^2/Vs to 8.74 cm^2/Vs, as shown in **Figure 1B**.

A)

KO$_2$:ZTO solution synthesis   KO$_2$:ZTO thin-film spin coating   Device fabrication

B)
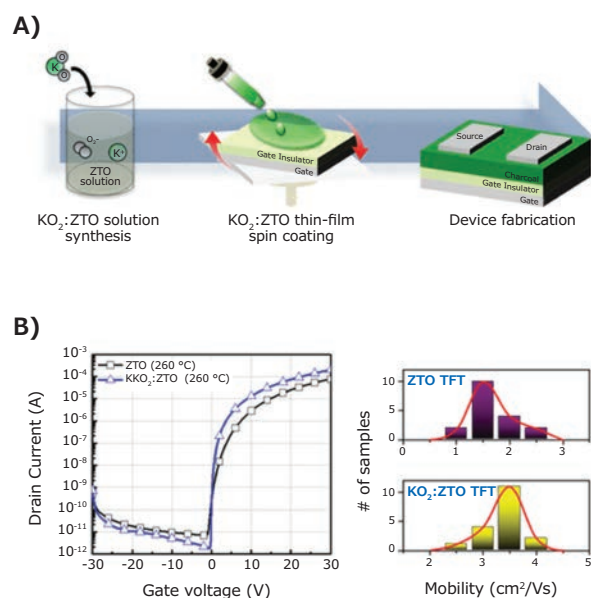
Figure 1. A) Schematic diagram of the manufacturing process of KO$_2$:ZTO. B) Comparison of transfer characteristics and mobility of ZTO TFT and KO$_2$:ZTO TFT.

A)

B)

Post annealing at 280 °C

C)

Post annealing at 230 °C
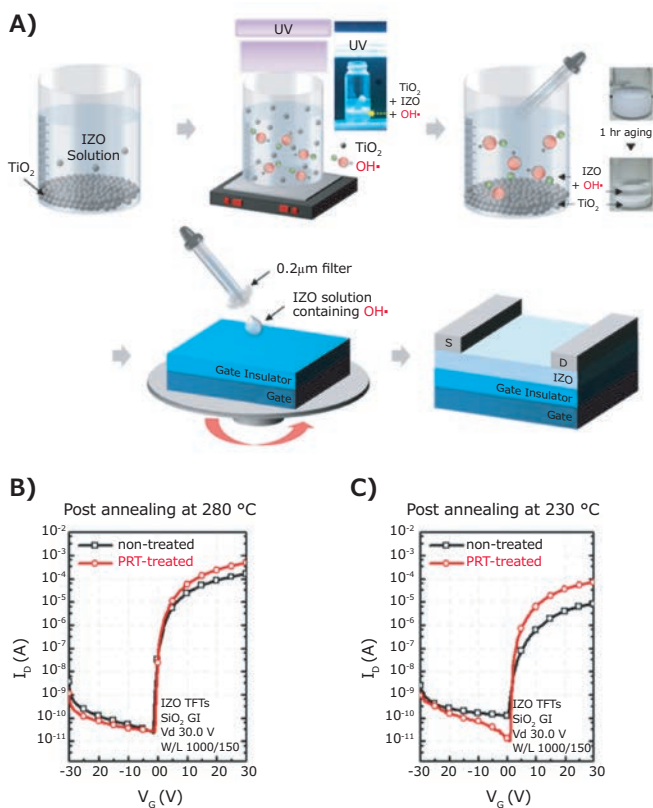
Figure 2. A) Schematic diagram of the manufacturing process of TiO_2:IZO TFT. Comparison of transfer characteristics between IZO TFT and TiO_2:IZO TFT with annealing temperature of B) 280 °C and C) 230 °C.

Similarly, **Figure 2** shows a study to improve the mobility of solution-processed IZO TFT by adding titanium dioxide (TiO_2) (**Cat. No. 1667585**).[17] As shown in **Figure 2A**, when TiO_2 is added to the IZO solution and then irradiated with ultraviolet light, hydroxyl radicals are formed through a photocatalytic reaction with water accelerating the decomposition of organic compounds with large hydroxyl radicals and forming smaller organic molecules. The decomposed small organic molecules have a low mass and boiling point, reducing defects in the active oxide layer. The IZO TFT with reduced defects showed an increase in mobility from 2.78 cm^2/Vs to 7.82 cm^2/Vs, as shown in **Figure 2B**.

Unlike the two methods introduced above, which add specific materials, the next method improves mobility through structural engineering. **Figure 3** represents a solution-processed oxide semiconductor TFT with high mobility and excellent reliability based on the corrugated heterojunction oxide active layer structure.[18] To control the electron concentration accumulated through charge modulation in the vertical region of the heterojunction, a corrugated active layer structure was formed by alternately using thin and thick ITZO/IGZO. This optimized heterojunction ITZO/IGZO TFT showed a high mobility of 50 cm^2/Vs.

Research on flexible oxide semiconductor based TFTs for free-form display

In order to make a flexible, free-form displays a reality, the backplane must be fabricated on a flexible substrate such as plastic rather than conventional glass. Representative flexible

A)

B)

C)
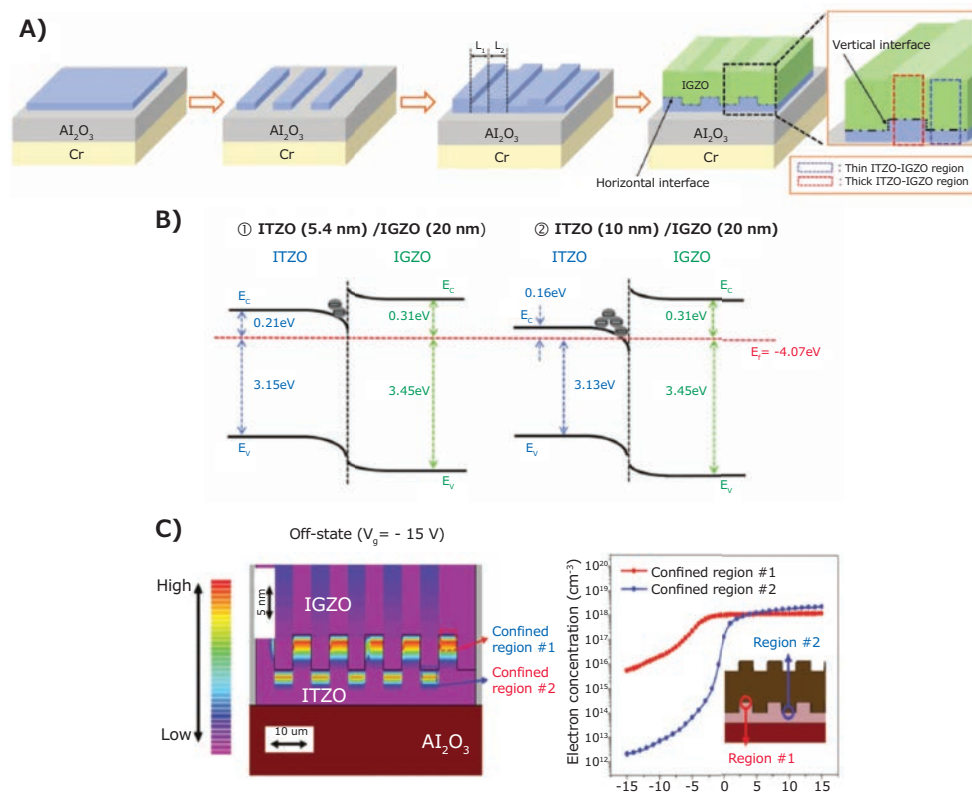
Figure 3. A) Schematic diagram of corrugated heterojunction oxide semiconductor TFT. B) Energy band of ITZO/IGZO active layer by ITZO thickness. C) TCAD simulation result for the current density of the off-state TFT. Reprinted with permission from reference 18, copyright 2018 Wiley.

substrates include polyethylene terephthalate (PET) (**Cat. No. GF14511215**), polyethylene naphthalate (PEN) (**Cat. No. GF23662043**), polyethersulfone (PES) (**Cat. No. GF98128109**), polyimide (PI) (**Cat. No. GF66798589**), with glass transition temperatures of about 80 °C , 120 °C , 220 °C , and 360 °C , respectively. Although the process temperatures for a device must be lower than the glass transition temperature of the substrate are typically processed at temperatures above 300 °C. Thus achieving a flexible, free-form display remains difficult due to the limitations and high cost of flexible plastic substrates, able to endure high process temperatures. As a result, it will be necessary to develop methods that obtain outstanding electrical characteristics and reliability using lower process temperature processed TFTs. This section introduces technologies that have the achieved process temperature below 250 °C through material, process, and structural engineering.

As more research to improve the flexibility of oxide TFTs based on the vacuum process have been reported, many of these methods of lowering the process temperature have included applying the flexible materials to the active layer and structure modification. For example, Kim et al. developed an open-air plasma treatment (OPT), which allows for dramatically decreased process temperature.[19] OPT not only decomposes weak metal-oxygen bonds by collision of ions included in ultraviolet (UV) and plasma, but also creates strong metal-oxygen bonds through the reaction of radicals (NO•, O•, OH•) and thermal treatment by

plasma. As a result, IGZO TFTs fabricated from OPT for 3 s at a low temperature below 300 °C showed electrical performances similar to conventional IGZO TFTs, allowing fabrication on a PI substrate, as shown in **Figure 4B** and **Figure 4C**.

Researchers have reported new approaches to fabricate flexible oxide TFTs in addition to the low temperature process. Kim et al. demonstrated hybrid oxide TFTs with excellent mechanical characteristics by doping a polytetrafluoroethylene (PTFE) with the Young's modulus of 0.3 GPa on IGZO, as shown in **Figure 4D** and **Figure 4E**.[20] The Young's modulus of the IGZO:PTFE formed by plasma polymerization was 85 GPa, less than the IGZO Young's modulus of 140 GPa. Additionally, since the fluorine (F) included in IGZO:PTFE has a strong electronegativity, it exhibits hydrophobicity by minimizing the number of coordination on the surface. As a result, the stability improved in ambient atmosphere compared to conventional TFTs.

Recently, Jang et al. IGZO TFTs fabricated on flexible plastic substrates applied on an etch-stopper (ES)-split active layer (SP) structure to improve the mechanical characteristics, as shown in **Figure 4F**.[21] In this study, nitrogen trifluoride (NF_3)/hydrogen (H_2) plasma dry etching was performed during the formation of ES-SP IGZO TFTs. At this time, the F atoms contained in the plasma remained in the ES and then flowed into both the ES-IGZO interface and bulk during the annealing process. Due to the previously mentioned characteristics of
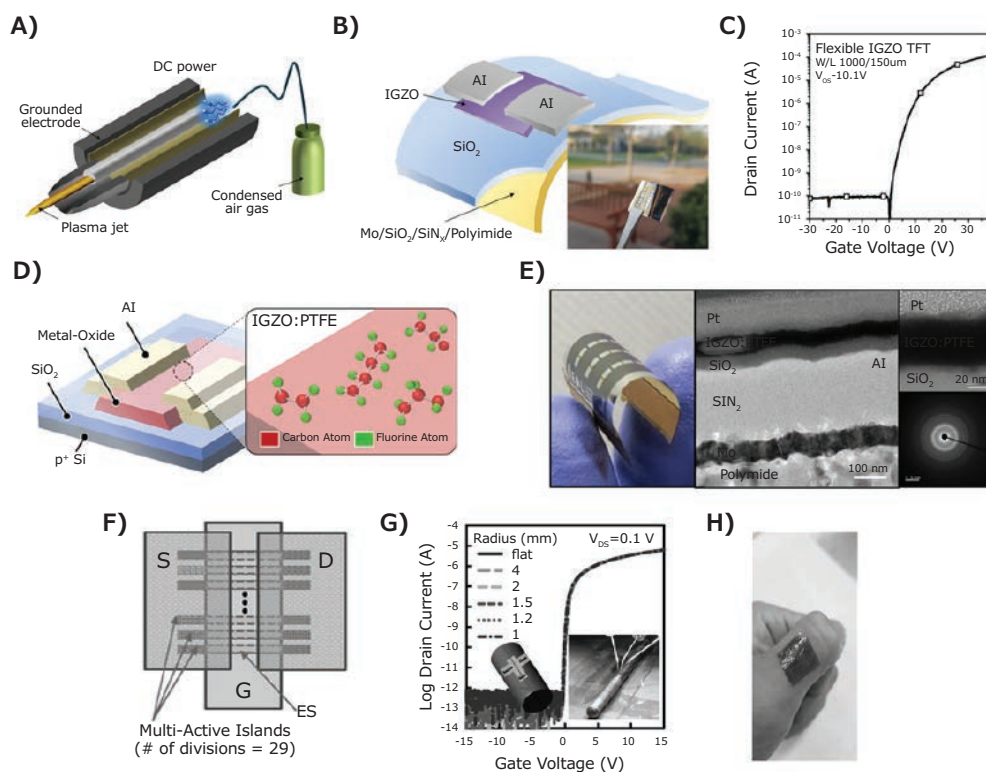
Figure 4. A) Schematic of OPT system. B) Schematic and C) the transfer characteristic of the IGZO TFT on the PI substrate. D) Schematic of the IGZO:PTFE TFT fabricated by co-sputtering. E) Photograph, the cross-sectional HR-TEM image, and diffraction patterns of IGZO:PTFE TFTs on the PI substrate. F) Structure of the ES-SP IGZO TFT. G) Transfer characteristics of ES-SP IGZO TFTs with various radius. H) Photograph of flexible IGZO TFT arrays. Reprinted with permission from reference 21, copyright 2017 Wiley.

the F atom, it showed superior mechanical characteristics after bending up to 5,000 times at a radius of 1 mm by reducing the unsaturated bonds at the ES and IGZO interfaces as well as oxygen vacancies and hydrogen bonding in the IGZO, as shown in **Figure 4G** and **Figure 4H**.

Unlike vacuum-processed oxide semiconductors, solution-processed oxide semiconductors are formed through decomposition, hydrolysis, dihydroxylation, and condensation reactions, requiring annealing temperature above 400 °C.[22] Due to the higher annealing temperature compared to vacuum-processed oxide TFTs, research on solution-processed oxide TFTs has been focused on low annealing temperature oxide semiconductors.

Next, we will review the materials engineering of solution-processed oxide TFTs at low processing temperatures. Previously, several methods of reducing the formation temperature of oxide semiconductors have been proposed using different precursors. Among these, oxide TFTs fabricated by metal alkoxide precursors have been reported to have excellent electrical characteristics, including field effect mobility of 10 cm^2/Vs with a processing temperature of 230 °C.[23] Also, studies have shown that the processing temperatures can be reduced by doping precursors with various metal and non-metal materials.[24–27] For example, when fabricating solution-processed IZO TFTs, precursors doped with the F atom show field effect mobility of 4.1 cm^2/Vs at a processing temperature of 200 °C. The F atom fills oxygen vacancies in oxide films, increasing the carrier concentration and strengthening bonding states of oxide films even at low processing temperatures.[28]

Unlike doping of inorganic materials in solution, the flexibility of the solution-processed oxide TFTs can be improved by doping with organic materials. As shown in **Figure 5A** and **Figure 5B**, In$_2$O$_3$ TFTs achieved a field effect mobility of above 10 cm^2/Vs at a processing temperature of 225oC by doping a poly(4-vinylphenol) (PVP) (**Cat. No. 436224**), a flexible insulating polymer.[29] PVP has two advantages: i) high solubility in the In$_2$O$_3$ solution, ii) enhanced flexibility through the hydroxyl group in the PVP, which can easily bind to the metal-oxygen lattice. Therefore, there is almost no change in the field effect mobility even after bending 100 times at a radius of 10 mm.

In addition to the already mentioned studies, other reports note that an additive capable of combustion can be added to the solution to cause an exothermic reaction on its own.[30–32] As shown in **Figure 5C** and **Figure 5D**, when an organic fuel(acetylacetone (**Cat. No. 10916**) or urea (**Cat. No. U5128**) and an oxidizer (in the form of a metal nitrate salt) (**Cat. No. L060050**) was mixed, the oxidation reaction reduced the energy barrier height to form an oxide thin film.[30] Different types of additives display different degrees of combustion required to reduce the energy barrier height, so the effect of lowering the processing temperature was also different, as shown in Figure 5E. In **Figure 5F**, the electrical characteristics of IGZO TFTs fabricated at the same processing temperature of 300 °C tend to vary depending on the additives, with a field
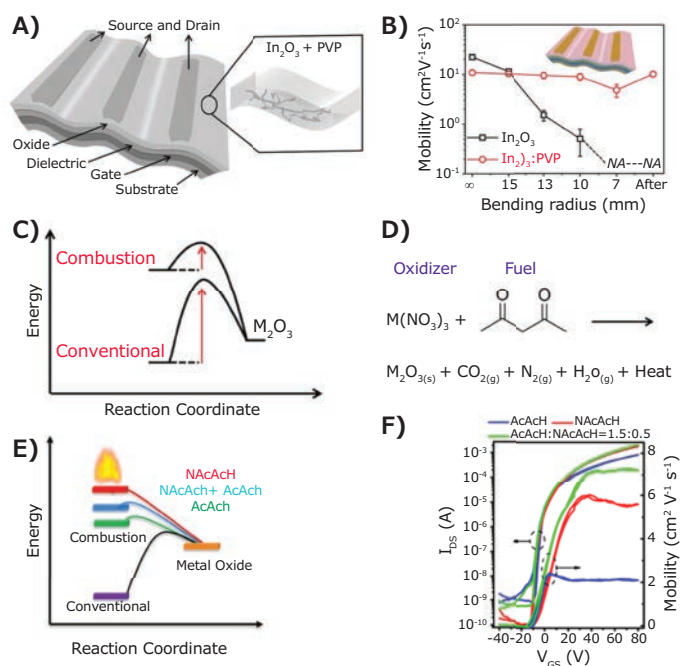
Figure 5. A) Schematic of solution-processed PVP doped In$_2$O$_3$ TFTs. B) Dependence of the field effect mobility on bending radius of both conventional In$_2$O$_3$ and PVP doped In$_2$O$_3$ TFTs. Reprinted with permission from reference 29, copyright 2015 Wiley. C) Schematic of reaction coordinate comparing the energy barrier height for combustion and conventional solution process. D) Example of combustion reaction using an organic fuel and an oxidizer. Reprinted with permission from reference 30, copyright 2013 American Chemical Society. E) Comparing the energy barrier height according to additives. F) Transfer characteristics of IGZO TFTs depending on additives. Reprinted with permission from reference 31, copyright 2018 American Chemical Society.

effect mobility of 5.7 cm^2/Vs under optimized conditions.[31] In this method, since the amount of emitted heat, gases, and impurities depends on the proportion of additives, optimization through appropriate trade-off was emphasized.

So far, we have introduced methods for precursor engineering of the dissolved materials in solution. However, most of the solvents that are used in oxide semiconductor solutions are based on organic alcohol species and contain many impurities. Therefore, recent research investigated a carbon-free water solvent to enable lower process temperatures.[33–34] **Figure 6A** and **Figure 6B** show the results of a study in which water solvent based ZnO solution was annealed at 180 °C to fabricate TFTs on flexible PEN substrates, achieving excellent mobility of 11 cm^2/Vs.[33] This is because the metal-amine of the amine-hydroxyl readily decomposes using a water-based solvent and carrying out dehydration and condensation reactions at relatively low energy. **Figure 6C** and **Figure 6D** show the results of a study in which water solvent based In$_2$O$_3$ TFTs were annealed at 100 °C and fabricated on PEN substrates, showing the mobility of 3.14 cm^2/Vs.[34] Using the thermogravimetric analysis (TGA) measurement, researchers confirmed that thermal decomposition occurred at a lower temperature than the alcohol based solvent, and that by-products were effectively removed through a sharp decrease in mass.
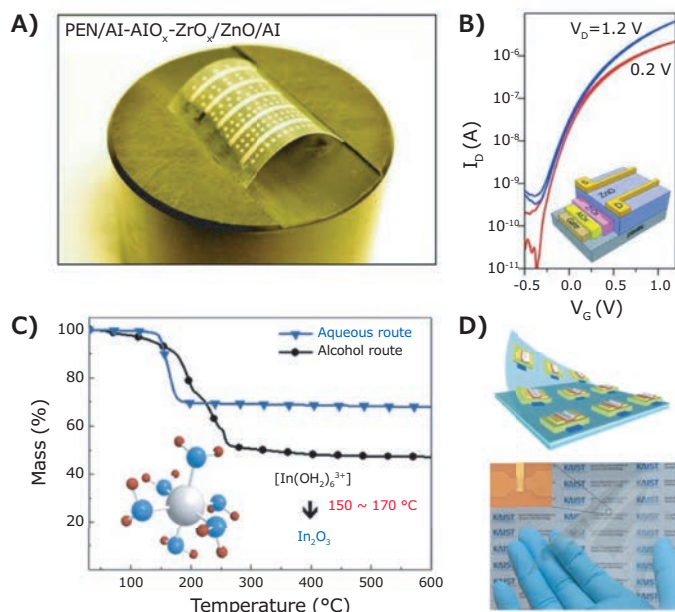
Figure 6. A) Image and B) transfer characteristics of solution-processed flexible ZnO TFT. Reprinted with permission from reference 33, copyright 2013 Wiley. C) Comparison of the TGA measurement on water and alcohol based In_2O_3 solution and D) image of the water solvent based flexible In_2O_3 TFT. Reprinted with permission from reference 34, copyright 2013 Nature Publishing Group.

Lastly, in terms of process, low temperature solution-processed oxide semiconductor based TFT studies can be classified according to the type of energy source that supplies the activation energy required to form an oxide thin film. In using conventional heat treatment, high temperature is applied to the flexible substrate, which may cause damage to the substrate. Other forms of energy that can be used include optical, chemical, and physical energy sources. Photoactivation, plasma treatment, microwave treatment, and high-pressure annealing have most frequently been reported as representative energy sources for low temperature annealed solution-processed oxide semiconductor TFTs. Among them, photo-energy treatment will be discussed here. The photo-energy treatment process can support a wide range of process windows by controlling variables such as wavelength, intensity, time, and irradiation method (lamp or laser).

Photo-energy causes vibrating atoms and molecules to break or rearrange their bonds. A study on room-temperature fabricated IGZO TFTs using a deep ultraviolet (DUV) photochemical activation process initiated active research on the annealing of solution-processed oxide thin films using various wavelengths of ultraviolet light.[35] As the DUV was irradiated, alkoxy groups in the oxide thin film were removed, and the quality of the thin film was improved by a more robust metal-oxygen bond. As a result, it showed a mobility of 7 cm²/Vs.

Another study reported solution-processed oxide thin-film formation using instantaneously irradiating light energy from a Xenon flash lamp, as shown in **Figure 7A**.[36] The ZnO thin

film was annealed at 90 °C and irradiated with pulse light of a wavelength of 350–950 nm. Light irradiation in the form of a lamp is advantageous for large-area processes and improves yield since the post-treatment is completed in 15 s. The thin film forms rapidly, and the electrical performance was almost similar to that of the ZnO TFT annealed at 165oC for 40 min, meaning that the metal-oxygen bonds were firmly formed in 15 s. In **Figure 7B**, a solution-processed IGZO TFT with a mobility of 7.7 cm²/Vs was fabricated by simultaneously applying near infrared (NIR) and DUV light energy at room temperature and sequentially applying a flash light.[37] In detail, NIR and DUV light caused decomposition, hydrolysis, and dehydration reactions in the oxide thin film, and the number of robust metal-oxygen bonds increased with irradiation by the flash light. In addition to the lamp-type photo-energy treatment, laser-type treatment, which can apply energy to only selective areas accurately and quickly, has also been developed. An In_2O_3 TFT annealed at 150 °C was fabricated using a krypton fluorine (KrF) excimer laser; the region that received laser beam irradiation selectively showed semiconducting properties. The unexposed region showed insulating properties.[38] The TFTs fabricated by this technology showed higher mobility (13 cm²/Vs) than that of In_2O_3 TFT annealed at 250 °C. **Figure 7C** represents the schematic process of fabricating an IGZO TFT by inkjet deposition, post-treatment with 200 °C annealing, and selective NIR laser spike irradiation with a wavelength of 1,064 nm. The transfer characteristics are shown in **Figure 7D** by number of laser irradiations.[39] Additionally, the laser-irradiated solution-processed IGZO TFT mobility was 1.5 cm²/Vs, demonstrating that the performance improves compared to the heat-only treatment process.
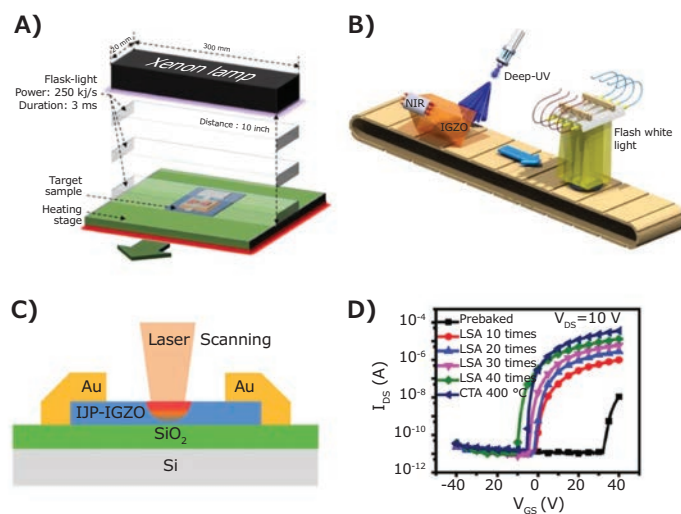
Figure 7. A) Schematic process of photo-energy treatment using Xenon flash light lamp. Reprinted with permission from reference 36, copyright 2015 Springer. B) Sequential process of NIR, DUV, and flash lamp photo-energy treatment. Reprinted with permission from reference 37, copyright 2019 American Chemical Society. C) Structure and D) transfer characteristics of IGZO TFT fabricated by inkjet process and NIR laser spike treatment. Reprinted with permission from reference 39, copyright 2017 Springer.

Conclusion

In summary, vacuum-processed oxide semiconductor TFTs will require further development to achive sufficient mobility to become viable for use in next-generation immersive, flexible, and free-form displays. In particular, TFTs will need to achieve a mobility of at least 30 cm²/Vs or more as well as mechanical reliability when fabricated on flexible substrates for widespread adoption. Beyond the display backplane, vigorous research and development on vacuum-processed TFTs must be conducted for commercialization in various electronic devices such as integrated logic circuits, memory devices, bio-sensors, photo-sensors, and gas-sensors. On the other hand, further development of solution-processed oxide semiconductor TFTs will also be needed to match the electrical performance and stability vacuum-processed oxide TFTs. Also, low temperature fabrication processes that utilize additional energy sources will need to be developed. Although many challenges still exist, the cost and environmental advantages of solution-processed oxide TFTs compared to the vacuum-processed TFTs are expected to drive their widespread introduction and adoption of printing processes.

Reference

(1) Klasens, H. A.; Koelmans, H. *Solid-State Electron*. **1964**, *7*, 701.
(2) Nomura, K.; Ohta, H.; Takagi, A.; Kamiya, T.; Hirano, M.; Hosono, H. *Nature* **2004**, *432*, 488.
(3) Kim, W.-G.; Tak, Y. J.; Kim, H. J. *J. Inf. Disp.* **2018**, *19*, 39.
(4) Park, J. W.; Kang, B. H.; Kim, H. J. *Adv. Funct. Mater.* **2020**, *30*, 1904632.
(5) Kamiya, T.; Nomura, K.; Hosono, H. *Sci. Technol. Adv. Mater.* **2010**, *11*, 044305.
(6) Kim, H. J.; Park, K.; Kim, H. J. J. Soc. Inf. Disp. 2020, 28, 591.
(7) Lee, H.; Chang, K. S.; Tak, Y. J.; Jung, T. S.; Park, J. W.; Kim, W.-G.; Chung, J.; Jeong, C. B.; Kim, H. J. *J. Inf. Disp.* **2017**, *18*, 131.
(8) Bebiche, S.; Wang, S.; Lei, L.; Wong, M.; Kwok, H.-S. *SID Symposium Digest of Technical Papers* **2018**, 1587.
(9) Han, D.; Zhang, Y.; Cong, Y.; Yu, W.; Zhang, X.; Wang, Y. *Sci Rep* **2016**, *6*, 38984.
(10) Lim, H. S.; Rim, Y. S.; Kim, D. L.; Jeong, W. H.; Kim, H. J. Electrochem. *Solid State Lett.* **2012**, *15*, H78.
(11) Banger, K. K.; Peterson, R. L.; Mori, K.; Yamashita, Y.; Leedham, T.; Sirringhaus, H. *Chem. Mat.* **2014**, *26*, 1195.
(12) Jun, T.; Song, K.; Jung, Y.; Jeong, S.; Moon, J. *J. Mater. Chem.* **2011**, *21*, 13524.
(13) Park, J.-S.; Kim, K.; Park, Y.-G.; Mo, Y.-G.; Kim, H. D.; Jeong, J. K. *Adv. Mater.* **2009**, *21*, 329.
(14) Hong, S.; Park, S. P.; Kim, Y.-G.; Kang, B. H.; Na, J. W.; Kim, H. J. *Sci. Rep.* **2017**, *7*, 16265.
(15) Lin, Z.; Lan, L.; Xiao, P.; Sun, S.; Li, Y.; Song, W.; Gao, P.; Ning, L. H.; Peng, J. *Appl. Phys. Lett.* **2015**, *107*, 112108.
(16) Jung, T. S.; Lee, H.; Kim, H. J.; Lee, J. H.; Kim, H. J. *ACS Appl. Mater. Interfaces* **2018**, *10*, 44554.
(17) Kang, J. K.; Park, S. P.; Na, J. W.; Lee, J. H.; Kim, D.; Kim, H. J. *ACS Appl. Mater. Interfaces* **2018**, *10*, 18837.
(18) Lee, M.; Jo, J. W.; Kim, Y. J.; Choi, S.; Kwon, S. M.; Jeon, S. P.; Facchetti, A.; Kim, Y. H.; Park, S. K. *Adv. Mater.* **2018**, *30*, 1804120.
(19) Tak, Y. J.; Hilt, F.; Keene, S.; Kim, W.-G.; Dauskardt, R. H.; Salleo, A.; Kim, H. J. ACS Appl. Mater. Interfaces 2018, 10, 37223.
(20) Na, J. W.; Kim, H. J.; Hong, S.; Kim, H. J. *ACS Appl. Mater*. **2018**, *10*, 37207.
(21) Lee, S.; Shin, J.; Jang, J. *Adv. Funct. Mater.* **2017**, *27*, 1604921.
(22) Kim, G. H.; Shin, H. S.; Ahn, B. D.; Kim, K. H.; Park, W. J.; Kim, H. J. *J. Electrochem. Soc.* **2009**, *156*, H7.
(23) Banger, K.; Yamashita, Y.; Mori, K.; Peterson, R.; Leedham, T.; Rickard, J.; Sirringhaus, H. *Nat. Mater.* **2011**, *10*, 45.
(24) Park, S. Y.; Kim, B. J.; Kim, K.; Kang, M. S.; Lim, K. H.; Lee, T. I.; Myoung, J. M.; Baik, H. K.; Cho, J. H.; Kim, Y. S. *Adv. Mater.* **2012**, *24*, 834.
(25) Kim, K.; Park, S. Y.; Lim, K.-H.; Shin, C.; Myoung, J.-M.; Kim, Y. S. *J. Mater. Chem.* **2012**, *22*, 23120.
(26) Banger, K. K.; Peterson, R. L.; Mori, K.; Yamashita, Y.; Leedham, T.; Sirringhaus, H. *Chem. Mater.* **2014**, *26*, 1195.
(27) Han, S.-Y.; Nguyen, M.-C.; Nguyen, A. H. T.; Choi, J.-W.; Kim, J.-Y.; Choi, R. *Thin Solid Films* **2017**, *641*, 19.
(28) Seo, J.-S.; Jeon, J.-H.; Hwang, Y. H.; Park, H.; Ryu, M.; Park, S.-H. K.; Bae, B.-S. *Sci. Rep.* **2013**, *3*, 2085.
(29) Yu, X.; Zeng, L.; Zhou, N.; Guo, P.; Shi, F.; Buchholz, D. B.; Ma, Q.; Yu, J.; Dravid, V. P.; Chang, R. P. *Adv. Mater.* **2015**, *27*, 2390.
(30) Hennek, J. W.; Smith, J.; Yan, A.; Kim, M.-G.; Zhao, W.; Dravid, V. P.; Facchetti, A.; Marks, T. J. *J. Am. Chem. Soc.* **2013**, *135*, 10729.
(31) Chen, Y.; Wang, B.; Huang, W.; Zhang, X.; Wang, G.; Leonardi, M. J.; Huang, Y.; Lu, Z.; Marks, T. J.; Facchetti, A. *Chem. Mater.* **2018**, *30*, 3323.
(32) Li, J.; Zhou, Y.-H.; Zhu, W.-Q.; Zhang, J.-H.; Zhang, Z.-L. *Mater. Sci. Semicond. Process.* **2019**, *93*, 201.
(33) Lin, Y. H.; Faber, H.; Zhao, K.; Wang, Q.; Amassian, A.; McLachlan, M.; Anthopoulos, T. D. *Adv. Mater.* **2013**, *25*, 4340.
(34) Hwang, Y. H.; Seo, J.-S.; Yun, J. M.; Park, H.; Yang, S.; Park, S.-H. K.; Bae, B.-S. *NPG Asia Mater.* **2013**, *5*, e45.
(35) Park, S.; Kim, K. H.; Jo, J. W.; Sung, S.; Kim, K. T.; Lee, W. J.; Kim, J.; Kim, H. J.; Yi, G. R.; Kim, Y. H. *Adv. Funct. Mater.* **2015**, *25*, 2807.
(36) Kim, D. W.; Park, J.; Hwang, J.; Kim, H. D.; Ryu, J. H.; Lee, K. B.; Baek, K. H.; Do, L.-M.; Choi, J. S. *Electron. Mater. Lett.* **2015**, *11*, 82.
(37) Moon, C.-J.; Kim, H.-S. *ACS Appl. Mater. Interfaces* **2019**, *11*, 13380.
(38) Dellis, S.; Isakov, I.; Kalfagiannis, N.; Tetzner, K.; Anthopoulos, T. D.; Koutsogeorgis, D. C. *J. Mater. Chem. C* **2017**, *5*, 3673.
(39) Huang, H.; Hu, H.; Zhu, J.; Guo, T. *J. Electron. Mater.* **2017**, *46*, 4497.

High Purity Oxides

Name	Composition	Form	Purity	Cat. No.
Bismuth(III) oxide	Bi_2O_3	powder	99.999% trace metals basis	202827-10G 202827-50G 202827-250G
Copper(II) oxide	CuO	powder	99.999% trace metals basis	203130-5G 203130-25G
Europium(III) oxide	Eu_2O_3	powder and chunks	99.999% trace metals basis	323543-1G 323543-5G
Iron(III) oxide	Fe_2O_3	powder	≥99.995% trace metals basis	529311-5G 529311-25G
Germanium(IV) oxide	GeO_2	powder	99.999% trace metals basis	483001-10G 483001-50G
Mercury(II) oxide	HgO	powder	99.999% trace metals basis	203793-2G 203793-10G
Holmium(III) oxide	Ho_2O_3	powder	99.999% trace metals basis	229679-1G 229679-10G
Indium(III) oxide	In_2O_3	powder	99.998% trace metals basis	203424-5G 203424-25G
Lanthanum(III) oxide	La_2O_3	powder	99.999% trace metals basis	203556-100G
Nickel(II) oxide	NiO	solid	≥99.995% trace metals basis	481793-5G 481793-25G
Lead(II) oxide	PbO	powder and chunks	99.999% trace metals basis	203610-10G 203610-50G
Lead(IV) oxide	PbO_2	powder	99.998% trace metals basis	518131-10G

Name	Composition	Form	Purity	Cat. No.
Antimony(III) oxide	Sb_2O_3	powder	99.999% trace metals basis	**202649-10G** **202649-50G**
Scandium(III) oxide	Sc_2O_3	powder	99.995% trace rare earth metals basis	**294020-500MG** **294020-5G**
Selenium dioxide	SeO_2	solid	99.999% trace metals basis	**204315-10G** **204315-50G**
Samarium(III) oxide	Sm_2O_3	powder	99.999% trace rare earth metals basis	**394394-25G**
Terbium(III,IV) oxide	Tb_4O_7	powder	99.999% trace metals basis	**204579-2G**
Yttrium(III) oxide	Y_2O_3	powder	99.999% trace metals basis	**204927-10G** **204927-50G**
Zinc oxide	ZnO	powder	99.999% trace metals basis	**204951-25G** **204951-125G**

Flexible Substrates

PET

Name	Form	Surface Resistivity (Ω/sq)	L × W × thickness	Cat. No.
Indium oxide coated PET	film	-	300 mm x 300 mm x 0.25 mm	**GF25214475-1EA** **GF25214475-2EA** **GF25214475-5EA** **GF25214475-10EA** **GF25214475-20EA**
	film	≤10	150 mm x 150 mm x 0.2 mm	**700177-5PAK** **700177-10PAK**
Indium tin oxide coated PET	sheet	60	1 ft × 1 ft × 5 mil	**639303-1EA** **639303-5EA**
	sheet	100	1 ft × 1 ft × 5 mil	**639281-1EA** **639281-5EA**
	sheet	300	1 ft × 1 ft × 5 mil	**749796-1EA** **749796-5EA**
	sheet	250	1 ft × 1 ft × 5 mil	**749761-1EA** **749761-5EA**
	sheet	60	1 ft × 1 ft × 7 mil	**749729-1EA** **749729-5EA**
Polyethylene Terephthalate	sheet	-	300 mm x 300 mm x 2 mm	**GF14511215-1EA** **GF14511215-2EA** **GF14511215-5EA**

PEN

Name	Form	L × W × Thickness	Cat. No.
Polyethylene Naphthalate	film	150 × 150 x 0.125 mm	**GF16154412-1EA** **GF16154412-2EA** **GF16154412-5EA** **GF16154412-10EA** **GF16154412-20EA**
	film	150 × 150 x 0.05 mm	**GF32830770-1EA** **GF32830770-2EA** **GF32830770-5EA** **GF32830770-10EA** **GF32830770-20EA**
	film	150 × 150 x 0.0013 mm	**GF23662043-1EA** **GF23662043-2EA** **GF23662043-5EA** **GF23662043-10EA** **GF23662043-20EA**

PES

Name	Form	L × W × Thickness	Cat. No.
Polyethersulfone	film	250 × 250 x 0.1 mm	**GF18849965-1EA** **GF18849965-2EA** **GF18849965-5EA** **GF18849965-10EA** **GF18849965-20EA**
	film	250 × 250 x 0.05 mm	**GF60096326-1EA** **GF60096326-2EA** **GF60096326-5EA** **GF60096326-10EA**
	film	300 × 300 x 0.25 mm	**GF12484144-1EA** **GF12484144-2EA** **GF12484144-5EA**
	film	300 × 300 x 0.5 mm	**GF34092626-1EA** **GF34092626-2EA**
	film	300 × 300 x 0.025 mm	**GF98128109-1EA** **GF98128109-2EA** **GF98128109-5EA**

PI
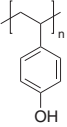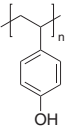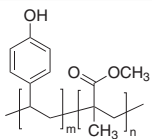
Name	Form	L × W × Thickness	Cat. No.
Polyimide	film	300 × 300 x 0.075 mm	GF97243476-1EA GF97243476-2EA GF97243476-5EA GF97243476-10EA
	film	300 × 300 x 0.025 mm	GF01413818-1EA GF01413818-2EA GF01413818-5EA GF01413818-10EA
	film	300 × 300 x 0.05 mm	GF63250848-1EA GF63250848-2EA GF63250848-5EA GF63250848-10EA
	film	300 × 300 x 0.125 mm	GF66798589-1EA GF66798589-2EA GF66798589-5EA GF66798589-10EA GF66798589-20EA

PTFE

Name	Form	Particle Size (µm)	Transition Temp.	Cat. No.
Poly(tetrafluoroethylene)	beads	-	-	81377-50G
	powder (free-flowing)	≤12	T_m 321 °C	430943-5G 430943-100G
	powder	35	T_m 321 °C	468096-5G 468096-100G
	powder	>40	T_m 327 °C T_g 130 °C	182478-100G 182478-250G
	dispersion	-	-	665800-100ML 665800-500ML
	powder (free-flowing)	1	T_m 321 °C	430935-5G 430935-100G

Poly(4-vinylphenol) (PVP)

Name	Structure	Purity/Molecular Weight	Cat. No.
Poly(4-vinylphenol)		M_w ~11,000	436216-5G 436216-25G
		average M_w ~25,000	436224-5G 436224-25G
Poly(4-vinylphenol-co-methyl methacrylate)		M_n 3,000-5,000 Da average M_w 8.000-12,000 Da	474576-50G

Metal Oxide Nanoparticle Inks

Name	Work Function	Viscosity At 20 °C	Cat. No.
Tungsten oxide nanoparticle ink, 25 wt. %	-	8 cP	807753-5ML 807753-25ML 807753-50ML
Zinc oxide nanoparticle ink	-	-	793361-5ML 793361-25ML 793361-50ML
Zinc oxide nanoparticle ink, 2.5 wt. %	-4.3eV	8-14 cP	807613-5ML 807613-10ML 807613-50ML
Zinc oxide nanoparticle ink, 2.5 wt. %	-4.3eV	2.4-3.8 cP	807648-10ML 807648-50ML
Zinc oxide nanoparticle ink, 2.5 wt. %	-3.9eV	1.6-2.6 cP	808253-10ML 808253-50ML
Aluminum-doped zinc oxide nanoparticle ink, 2.5 wt. %	-4.3eV	1.9-3.1 cP	807729-10ML 807729-50ML

Name	Work Function	Viscosity At 20 °C	Cat. No.
Aluminum-doped zinc oxide nanoparticle ink, 2.5 wt. %	-3.9eV	8-14 cP	808180-5ML 808180-10ML 808180-50ML
Tin(IV) oxide nanoparticle ink, 2.5 wt%	-	4 cP	901071-10ML 901071-50ML
Tin(IV) oxide nanoparticle ink, 2.5 wt%	-	3.5 cP	901079-10ML 901079-50ML
Tungsten oxide (WO_{3-x}) nanoparticle ink	-	-	793353-5ML 793353-25ML 793353-50ML
Zinc oxide ink for inkjet printing	4.0 ± 0.1 eV	10.5 mPa.s ±3.0 mPa.s	901091-25ML
Zinc oxide ink for spin coating/slot-die coating	4.0 ± 0.1 eV	<4 mPa.s	901081-25ML
Molybdenum oxide nanoparticle ink	-	1-3 cP	900151-10ML

High Purity Metal Nitrate Salts

Name	Composition	Form	Purity	Cat. No.
Silver nitrate	$AgNO_3$	solid crystalline	99.9999% trace metals basis	204390-1G 204390-10G 204390-50G 204390-250G 204390-2KG
		solid powder	≥99.999% trace metals basis	792276-10G
Copper(II) nitrate hydrate	$Cu(NO_3)_2 \cdot xH_2O$	crystals and lumps	99.999% trace metals basis	229636-5G 229636-25G 229636-100G
Cobalt(II) nitrate hexahydrate	$Co(NO_3)_2 \cdot 6H_2O$	crystals and lumps	99.999% trace metals basis	203106-10G 203106-50G
Iron(III) nitrate nonahydrate	$Fe(NO_3)_3 \cdot 9H_2O$	solid	≥99.999% trace metals basis	529303-25G
Aluminum nitrate nonahydrate	$Al(NO_3)_3 \cdot 9H_2O$	crystals and lumps	99.997% trace metals basis	229415-10G 229415-100G
Gallium(III) nitrate hydrate	$Ga(NO_3)_3 \cdot xH_2O$	crystals and lumps	99.999% trace metals basis	229644-5G 229644-50G
		crystalline	99.9% trace metals basis	289892-5G 289892-25G 289892-100G 289892-1KG
Calcium nitrate hydrate	$Ca(NO_3)_2 \cdot xH_2O$	crystals and lumps	99.997% trace metals basis	202967-10G 202967-50G
Lead(II) nitrate	$Pb(NO_3)_2$	solid crystals and lumps	99.999% trace metals basis	203580-10G 203580-50G
		solid	≥99.95% trace metals basis	467790-50G 467790-250G
Potassium nitrate	KNO_3	crystalline	99.999% trace metals basis	542040-10G 542040-50G
		crystalline	99.99% trace metals basis	204110-50G 204110-250G
Nickel(II) nitrate hexahydrate	$Ni(NO_3)_2 \cdot 6H_2O$	solid	99.999% trace metals basis	203874-20G 203874-100G 203874-500G
Europium(III) nitrate pentahydrate	$Eu(NO_3)_3 \cdot 5H_2O$	crystals and lumps	99.9% trace metals basis	207918-1G 207918-10G 207918-50G
Cerium(III) nitrate hexahydrate	$Ce(NO_3)_3 \cdot 6H_2O$	crystals and lumps	99.999% trace metals basis	202991-25G 202991-125G
		crystals and lumps	99.99% trace metals basis	392219-25G 392219-100G
Zinc nitrate hydrate	$Zn(NO_3)_2 \cdot xH_2O$	powder and chunks	99.999% trace metals basis	230006-25G 230006-250G
Manganese(II) nitrate hydrate	$Mn(NO_3)_2 \cdot xH_2O$	crystals and lumps	99.99% trace metals basis	203742-25G 203742-100G
Cadmium nitrate tetrahydrate	$Cd(NO_3)_2 \cdot 4H_2O$	solid	99.997% trace metals basis	229520-10G
Neodymium(III) nitrate hexahydrate	$Nd(NO_3)_3 \cdot 6H_2O$	crystalline	99.9% trace metals basis	289175-25G 289175-100G
Gadolinium(III) nitrate hexahydrate	$Gd(NO_3)_3 \cdot 6H_2O$	crystals and lumps	99.999% trace metals basis	217190-10G
		solid	99.99% trace metals basis	451134-10G 451134-50G
		crystals and lumps	99.9% trace metals basis	211591-25G 211591-100G
Magnesium nitrate hexahydrate	$Mg(NO_3)_2 \cdot 6H_2O$	solid	99.999% trace metals basis	203696-10G 203696-50G
Bismuth(III) nitrate pentahydrate	$Bi(NO_3)_3 \cdot 5H_2O$	-	99.999% trace metals basis	254150-25G
Copper(II) nitrate hemi(pentahydrate)	$Cu(NO_3)_2 \cdot 2.5H_2O$	crystalline	≥99.99% trace metals basis	467855-50G 467855-250G

Name	Composition	Form	Purity	Cat. No.
Europium(III) nitrate hydrate	$Eu(NO_3)_3 \cdot xH_2O$	solid	99.99% trace metals basis	**254061-1G** **254061-10G**
Barium nitrate	$Ba(NO_3)_2$	solid	99.999% trace metals basis	**202754-25G** **202754-100G**
Palladium(II) nitrate solution	$Pd(NO_3)_2$	10 wt. % nitric acid	99.999% trace metals basis	**380040-10ML** **380040-50ML**
Terbium(III) nitrate pentahydrate	$Tb(NO_3)_3 \cdot 5H_2O$	solid	99.9% trace metals basis	**325945-5G** **325945-25G**
Dysprosium(III) nitrate hydrate	$Dy(NO_3)_3 \cdot xH_2O$	crystals and lumps	99.9% trace metals basis	**298158-25G** **298158-100G**
Lanthanum(III) nitrate hexahydrate	$La(NO_3)_3 \cdot 6H_2O$	solid	99.999% trace metals basis	**203548-25G** **203548-100G** **203548-500G**
		solid	99.99% trace metals basis	**331937-5G** **331937-100G** **331937-500G**
Praseodymium(III) nitrate hexahydrate	$Pr(NO_3)_3 \cdot 6H_2O$	crystalline	99.9% trace metals basis	**205133-10G** **205133-50G** **205133-250G**
Rhodium(III) nitrate hydrate	$N_3O_9Rh \cdot xH_2O$	-	~36% rhodium (Rh) basis	**83750-250MG** **83750-1G**
Erbium(III) nitrate pentahydrate	$Er(NO_3)_3 \cdot 5H_2O$	crystals and lumps	99.9% trace metals basis	**298166-25G** **298166-100G**
Lanthanum(III) nitrate hydrate	$La(NO_3)_3 \cdot xH_2O$	(powder, crystals or chunks)	99.9% trace metals basis	**238554-100G** **238554-500G**
Indium(III) nitrate hydrate	$In(NO_3)_3 \cdot xH_2O$	crystals and lumps	99.999% trace metals basis	**254215-10G** **254215-50G**
		powder and chunks	99.99% trace metals basis	**326127-10G** **326127-50G**
		crystals and lumps	99.9% trace metals basis	**326135-10G** **326135-50G**
Samarium(III) nitrate hexahydrate	$Sm(NO_3)_3 \cdot 6H_2O$	crystalline	99.999% trace metals basis	**518247-5G** **518247-25G**
		powder and chunks	99.9% trace metals basis	**298123-25G** **298123-100G**
Ytterbium(III) nitrate pentahydrate	$Yb(NO_3)_3 \cdot 5H_2O$	crystals, granules or chunks	99.999%	**217220-5G** **217220-25G**
		crystals and lumps	99.9% trace metals basis	**209147-10G** **209147-50G**
Terbium(III) nitrate hexahydrate	$Tb(NO_3)_3 \cdot 6H_2O$	crystals and lumps	99.999% trace metals basis	**217212-2G** **217212-10G**
Cesium nitrate	$CsNO_3$	crystals and lumps	99.999% trace metals basis	**203041-10G** **203041-50G**
		powder	99.99% trace metals basis	**202150-10G** **202150-50G**
Yttrium(III) nitrate tetrahydrate	$Y(NO_3)_3 \cdot 4H_2O$	powder	99.999% trace metals basis	**217239-10G** **217239-50G**
		powder and chunks	99.99% trace metals basis	**331309-10G** **331309-100G**
Neodymium(III) nitrate hydrate	$Nd(NO_3)_3 \cdot xH_2O$	crystalline	99.99% trace metals basis	**217204-25G**
Strontium nitrate	$Sr(NO_3)_2$	crystals and lumps	99.995% trace metals basis	**204498-10G** **204498-50G**
Chromium(III) nitrate nonahydrate	$Cr(NO_3)_3 \cdot 9H_2O$	crystalline	≥99.99% trace metals basis	**379972-5G**
Scandium(III) nitrate hydrate	$Sc(NO_3)_3 \cdot xH_2O$	solid	99.999% trace metals basis	**529788-1G**
Lutetium(III) nitrate hydrate	$Lu(NO_3)_3 \cdot xH_2O$	solid	99.999% trace metals basis	**542067-5G**
Bismuth(III) nitrate pentahydrate	$Bi(NO_3)_3 \cdot 5H_2O$	-	≥99.99% trace metals basis	**467839-50G** **467839-250G**

Inorganic Graphene Analogs: Solution Processing and Applications

Kenneth Lobo and H. S. S. Ramakrishna Matte*

Energy Materials Laboratory, Centre for Nano and Soft Matter Sciences, Jalahalli, Bengaluru, India 560013
*Email: matte@cens.res.in, krishnamatte@gmail.com

Introduction

Nanomaterials have steadily established their presence in day-to-day life owing to their many-fold efficiency over bulk materials and due to the advancements in processing that have rendered them remarkably attractive. Solution processing is a strategy that offers several advantages over ambient processing, enabling easy incorporation of nanomaterials in diverse applications. In electronics, solution-processed nanomaterials have benefits over conventional lithographic approaches, including speed and simplicity in device fabrication for use in optoelectronics, sensing, energy conversion, and storage. Nanomaterials span various dimensionality, such as zero-dimensional perovskites and metal oxides, and one-dimensional like single-walled carbon nanotubes.[1-3] Two-dimensional (2D) materials have generated a remarkable level of interest following the ground-breaking publications on single-layer graphene in 2004. Since then, the field of 2D materials has grown into a large family of materials that encompasses a wide range of physicochemical properties.

Graphene provides excellent conductivity through electrons' ballistic transport, whereas hexagonal boron nitride and clays possess interesting dielectric properties. On the other hand, semiconducting transition metal dichalcogenides (TMDs) like MoS_2 (**Cat. No. 808652**) show an indirect to direct transition in bandgap from 1.2 eV to 1.9 eV with exfoliation from bulk crystals to monolayers. Besides these materials, other inorganic graphene analogs (IGAs), including layered double hydroxides (LDH), metal organic frameworks and covalent organic frameworks (MOFs and COFs), MXenes, elemental graphene analogs like pnictogens, and others are driving new research trends in a plethora of applications. Micromechanical cleavage of bulk crystals was the initial approach adopted for obtaining these materials in mono- and few-layers. This has since diversified into several other synthesis protocols through both top-down and bottom-up approaches. Each method provides its own advantages with suitable procedures established that enable tunability of properties to suit a specific application. One highly effective top-down synthesis protocol employed for scalable production of IGAs is liquid phase exfoliation (LPE) of bulk crystals in a suitable liquid media. The method yields stable dispersions that have the potential to enable facile solution-processing.[4] The exfoliation process is often carried out using high-speed shear mixing, ultrasonication, wet ball milling, or high-pressure homogenization to shear the bulk crystals immersed in a liquid phase and yield stable nanosheets. Suitable design of parameters like initial concentration of bulk precursor, process time, volume, power, and other factors for high-yield and feasibility has increased production rates to hundreds of liters per hour.[5]

Dispersions of 2D Materials

Several 2D materials have been processed into dispersions, as shown in **Figure 1A**. It is critical to understand the factors influencing the dispersibility of IGAs in liquid media to optimize production. LPE is a two-step process; shear forces are applied to bulk crystals to overcome the van der Waals forces operating between layers resulting in exfoliation of nanosheets, following which they are stabilized against restacking. Various approaches are deployed for exfoliation and stabilization of nanosheets, as shown in **Figure 1B**. Dispersions in aqueous media are often obtained using additives like surfactants, polymers, or salts. Surfactant molecules reduce the interfacial tension and enable the interaction between nanosheets and water while also charging them and enhancing their stability by electrostatic means. In this regard, several other non-ionic

surfactants such as Pluronic F-68 (**Cat. No. 914428**) and P-123 (**Cat. No. 915858**) have also been investigated.[6,7] Several polymers have been used for steric stabilization of nanosheets and enable the straightforward application of exfoliated material into nanocomposites. The use of these additives provides a method to produce mono- and few-layers of IGAs; however, their presence can hinder performance in certain applications. An alternative to additive-stabilized dispersions is the use of solvents that could interact suitably with the dispersed nanosheets for efficient exfoliation and stabilization. The solvent - nanosheet interaction and physical parameters of the solvent are known to influence its performance. Studies on graphene dispersibility indicate it is similar to that of carbon nanotubes, owing to strong interactions between the solvent and nanotube walls.[8] The underlying interactions have been probed and explained by several theories, such as Hansen's solubility theory and surface tension.[4,9] Selection criteria based on the Hansen theory suggest that interactions are comprised of dispersive, polar and hydrogen components. For semiconducting TMDs, research shows these components must be ~18 MPa$^{0.5}$, ~8.5 MPa$^{0.5}$ and ~7 MPa$^{0.5}$, respectively. Solvents such as N-methyl pyrrolidone (NMP, **Cat. No. 270468**), dimethyl sulfoxide (DMSO, **Cat. No. 276855**), and dimethylformamide (DMF, **Cat. No. 227056**) disperse TMDs with appreciable efficiencies owing to the matching of these components. In germanane, the solubility components were found to be ~24 MPa$^{0.5}$, ~13 MPa$^{0.5}$ and ~16 MPa$^{0.5}$ for the dispersive, polar, and hydrogen contributions, respectively, compared to that for ionic liquids like 1,3-butyl methyl imidazoliumtetrafluoroborate.[10]

The parameter determination is performed by evaluating the material dispersibility in a large probe set and matching with the best performing solvents based on the Hansen interaction radius (**Figure 1C**). Hansen solubility parameters have been determined for just a handful of IGAs, in comparison with the vast family of 2D materials. This approach has been extended to mixed-solvent systems, where the proportions of the mixture are used to tune its Hansen parameters. Another approach to understanding the dispersibility of 2D materials is evaluating exfoliation based on their surface tension components rather than the total surface tension, as shown in **Figure 1D**. Similar to the Hansen theory, this approach has proven useful in mixed-solvent systems.[11,12] Theoretical calculations using density functional theory and molecular dynamics, supported by experimental observations, suggest the role of additional factors in exfoliation and stabilization that are unaccounted for in these theories and call for further refinement. For example, trace amounts of water are known to be critical for exfoliation in NMP, or the presence of an excellent exfoliating solvent like DMF in trace amounts is needed to achieve stability when transferred into poor solvents like water.[13,14] Viscosity of the liquid phase is another decisive parameter for stability.[15] Given the length scales involved, the size and shape of the solvent molecule and its structuring/ ordering and coverage on the nanosheet surface are influential in LPE, also seen in both pure solvents and mixed-solvent systems.[16–18] **Figure 1E** shows the preferential binding site for solvent molecules adsorbed on the surface of MoS$_2$ obtained from density functional theory calculations. **Figure 1F** shows the "wedging" of solvent molecules between layers during exfoliation as simulated using molecular dynamics. Such methods could help draw a clearer picture of the underlying mechanisms of solvent exfoliation and stabilization.
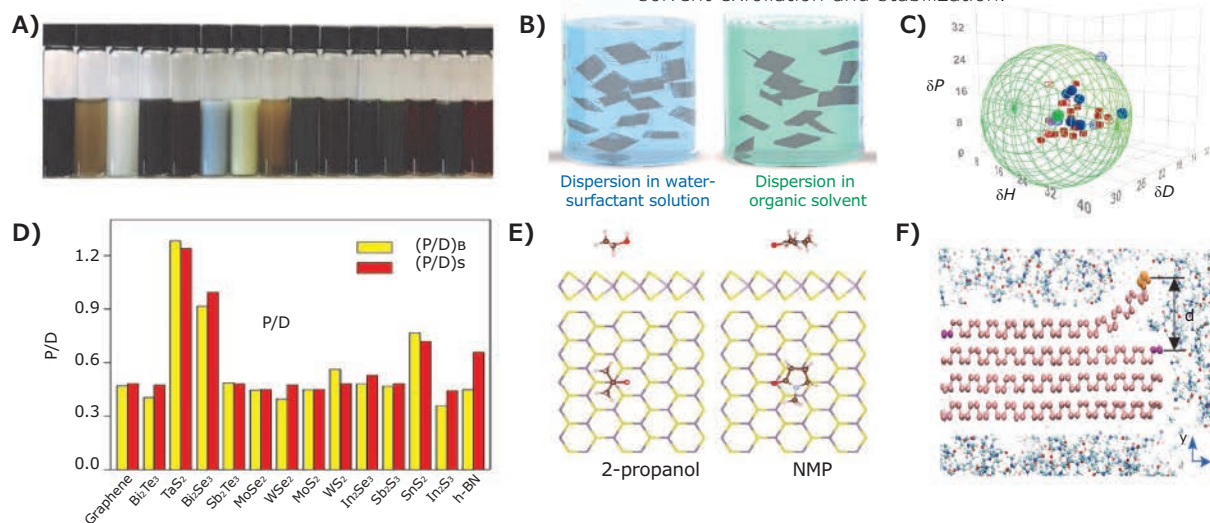
Figure 1. Aspects influencing the dispersibility of 2D materials. **A**) Photograph of functional inks of various 2D materials. **B**) Additive based (surfactant) and additive-free (organic) approach to obtaining stable dispersions. A and B Adapted with permission from reference 23, copyright 2016 Wiley-VCH. **C**) Hansen sphere computation as a means for solvent screening in liquid phase exfoliation of germanane. Adapted with permission from reference 10, copyright 2018 American Chemical Society. **D**) Dispersibility of 2D materials in solvents based on surface tension components. By choosing solvents with suitable ratios of polar to dispersive components, exfoliation conditions can be optimized. Adapted with permission from reference 9, copyright 2017 American Chemical Society. **E**) Adsorption of solvent molecules on the surface of MoS$_2$ obtained from first-principles as a means of understanding exfoliation and stabilization. Adapted with permission from reference 24, copyright 2018 American Institute of Physics. **F**) Solvent molecule geometry as a factor in the exfoliation and stabilization of black phosphorus nanosheets. Adapted with permission from reference 18, copyright 2015 American Chemical Society.

Among solvents, water is an ideal candidate for several reasons, such as non-toxicity, feasibility, and easy processing. Graphene oxide consists of various functional moieties on the nanosheet surface that render it hydrophilic nature. Depending on the extent of functionalization, graphene oxide dispersions can be readily obtained in water alone, whereas pristine graphene is hydrophobic and has negligible dispersibility in water. Aqueous dispersions of few other 2D materials like MXenes (2D carbides and nitrides) are stable, owing mainly to the surface and edge functionalization. Besides a few exceptions, most studied IGAs are hydrophobic and make poor dispersions in water. TMDs in octahedral 1T-phase obtained through lithium intercalation and exfoliation in water result in monolayers, which are metallic in nature. In comparison to this, the trigonal prismatic 2H-phase with remarkable semiconducting properties exhibits poor dispersibility in water.

Nanosheets can be functionalized to improve dispersibility of 2H-phase TMDs; other strategies to obtain aqueous dispersions include the introduction of defects or exposed edges. Besides efficiency, several other factors are also influential in deciding upon a solvent. This includes considerations like toxicity and boiling point, stringent processing protocols, or use restrictions on solvents like NMP. Safer low boiling alternatives like isopropyl alcohol, acetone, 2-butanone have been investigated in this regard and are suitable alternatives.[16,19] Cyrene (**Cat. No. 807796**) is shown to be a greener substitute for NMP. While the two solvents have different viscosities, they are similar in several aspects like Hansen solubility parameters and surface tensions. This difference results in higher exfoliation yields and provides a safer and greener processing for these materials because Cyrene is non-toxic, sustainable, and biodegradable. Therein lies significant scope for the development of suitable solvents for the green processing of 2D materials.

Since exfoliation is a top-down approach, the bulk precursor plays a crucial role on the process and the properties of the resulting exfoliated nanosheets.[20] Various approaches involving the pre-treatment or pre-processing of the bulk show enhancement in yield and enable engineering of the physicochemical properties. Mechanical pre-treatments that shear and reduce the dimensions of the bulk crystals through methods like ball milling show enhanced yields in subsequent LPE.[21] Additionally, modification through functionalization vastly improves dispersibility and helps tune the nanosheet interface.[19] In the case of a few sensitive materials such as black phosphorus, the liquid phase is shown to provide oxidative protection to the exfoliated nanosheets. Here, pre-exfoliation protocols like degassing of the solvent is required to obtain stable oxidation-free nanosheets.[22]

Polydispersity in both the size and thickness of nanosheets is an inherent property of LPE. Since the properties of nanosheets depend heavily on their dimensions, it is crucial to have control of their size. Various centrifugation based techniques such as isopycnic density gradient centrifugation and liquid cascade centrifugation have been deployed to separate polydisperse

nanosheets into monodisperse or monolayer enriched dispersions. During centrifugation, nanosheets are subjected to differential centrifugal forces, buoyant forces, and viscous drag depending on their dimensions, resulting in their separation.[6,25,26] Separation by dimension enables the efficient use of exfoliated nanosheets for specific applications since monodispersity enables reliable and optimum performance compared to polydisperse nanosheets.

Solution Processed Inorganic Films

2D materials are an enticing premise for investigation of a diverse variety of applications. Their physical structure enables their use in burgeoning technologies such as flexible printed electronic devices including thin-film transistors, displays, sensors, supercapacitors, solar cells, and transparent electrodes on both rigid and flexible substrates. Additionally, the immense diversity among IGAs also allows for their use in tandem with each other by fabricating heterostructures or superlattices.[32] Well established and scalable deposition protocols like spray coating, Langmuir film transfer, roll-to-roll processes, doctor blading, and printing techniques such as gravure, inkjet, and screen printing have been used on both rigid and flexible substrates.[16,33,34] Several variants of printing can provide a balance between throughput and resolution. Inkjet printing enables resolution of a few tens of micrometers and gravure printing enables throughput of up to a few hundred meters squared per second. These well-established techniques could allow the widespread use of IGAs in the form of suitable inks. In addition to the material and solvent, the inks could be composed of pigments, binders, dryers, and viscosifiers, but must be engineered for proper compatibility with the printing method used.

A variety of electronic elements, including both active and passive, and those with different architectures, have been produced through solution-processing methods. In addition to those due to other insulating components in the ink, resistive networks in films arise from inter- and intra-nanosheet junctions. Thin-film resistance is an essential aspect in printed circuits, and methods like photonic annealing and compression can be employed to obtain desirable electrical properties in films.[35] Capacitive devices can be improved by incorporating h-BN (**Cat. No. 901768**) and BiOCl (**Cat. No. 307610**), which have highly desirable dielectric properties.[27,36] Low temperature processed h-BN capacitors made through electrophoretic deposition onto flexible ITO coated PET sheet are shown in **Figure 2A**, with conformal coatings imaged by an atomic force microscope shown in **Figure 2B**. Along with its application as a dielectric in capacitors and encapsulations for electronic devices, h-BN also bears potential as a thermal interface material owing to its high thermal conductivity. Several semiconducting IGAs have band-gaps in the visible region, making them desirable for applications in optoelectronics such as photodetectors. Spray-coating of low boiling point inks onto two terminal devices as shown in **Figure 2C** has been demonstrated for fabrication of MoS_2 photodetectors (**Figure 2D**),[16] indicating high-speed and large-area scalability (**Figure 2E**) for device fabrication. Inkjet-printing provides a suitable avenue in multi-material printing
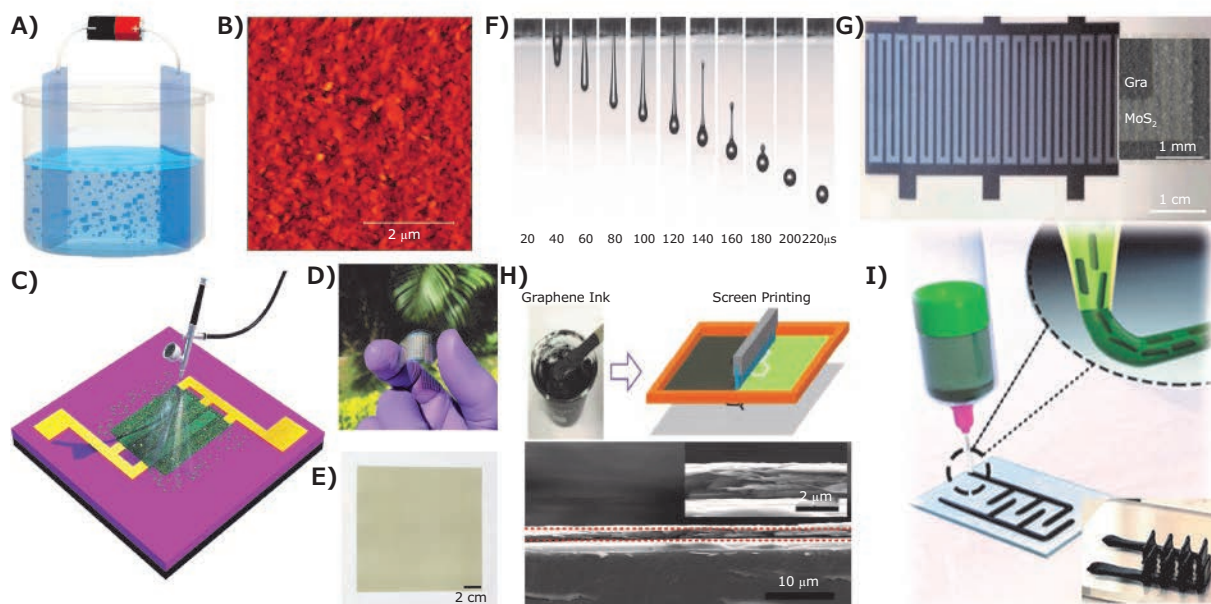
Figure 2. Routes to solution processing of 2D materials. **A**) Electrophoretic deposition of h-BN nanosheets onto conducting substrates, showing the conformal coating, as seen in the **B**) AFM image. Adapted with permission from reference 27, copyright 2019 American Chemical Society. **C**) Spray coating as a method for deposition of low viscosity inks for flexible optoelectronics of devices, as shown in the photograph in **D**) and its potential for large area deposition **E**). Adapted with permission from reference 16, copyright 2019 Royal Society of Chemistry. **F**) Droplet formation in inkjet printing showing good drop jetting without the formation of undesirable satellite droplets. Adapted with permission from reference 28, copyright 2009 American Chemical Society. **G**) Photodetector fabricated using inkjet printing of 2D material inks, with the inset showing the electron micrograph demarcating graphene contacts and photoactive MoS_2 regions. Adapted with permission from reference 29, copyright 2014 Royal Society of Chemistry. **H**) Screen printing of viscous graphene inks with an electron micrograph of the printed film after roller compression. Adapted with permission from reference 30, copyright 2019 American Chemical Society. **I**) 3D printing of structures using thick pastes of MXenes with a photograph of the printed structure in the inset. Adapted with permission from reference 31, copyright 2019 American Chemical Society.

compared to the previously mentioned deposition protocols with good resolution. The inverse Ohnesorge number, which depends on density, viscosity and surface tension, is optimal for inkjet printing when in the range of 1 to 14. Good jetting of ink droplets, as shown in **Figure 2F**, enables high resolution printing where satellite drop formation is avoided. Inkjet-printed photodetectors have been demonstrated with graphene and MoS_2 as shown in **Figure 2G**.[29,37] Research shows that inkjet-printed black phosphorus performs as a stable mode-locking saturable absorber, producing ultrashort pulses (fs) under intense laser irradiation.[38] Highly viscous inks (tending towards pastes) are more suitable for screen printing applications, such as the graphene ink shown in **Figure 2H**.[30] The electron micrograph shows the printed film after being subjected to roller compression for film compaction, exhibiting conductivity of 8.81 x 10^4 S/m. While there are several reports of screen printable graphene there is considerable scope in incorporating other IGAs for screen printing as well. Screen printed MXenes and Co-Al layered double hydroxide interdigitated devices in an asymmetric configuration on flexible polymeric substrate have been found to have high energy densities, good stability to flexure and high retention with cycling.[39] 3D printing is an upcoming avenue for nanomaterial application using methods like direct ink writing and fused deposition modelling to fabricate 2D material based energy storage devices like batteries and supercapacitors, sensors for temperature, and chemicals and mechanical strain.[40] **Figure 2I** shows one example of the incorporation of MXene nanosheets into 3D printed interdigital devices using a direct ink writing technique; the resulting device exhibited enhanced capacities of 1035 mF/cm^2.[31]

Applications with Functional 2D Material Films

Given the wide variety of processing techniques compatible with IGAs discussed in the previous section, the design flexibility and overall potential for this novel class of materials is clearly evident. Next, we will discuss selected reports that highlight applications that use IGAs. **Figure 3A** shows a passive capacitor device made using annealing-free electrophoretic deposition of h-BN, which performed as a stable device up to 1 MHz without a loss in capacitance (about 175 nF/cm^2).[27] When fabricated on ITO coated PET sheets, the devices exhibited stable capacitance with cyclic flexure as shown in **Figure 3B**. Energy storage devices such as batteries and supercapacitors of IGAs have received significant attention owing to the ever-increasing global energy demand. **Figure 3C** shows a supercapacitor fabricated through stamping of MXene inks, which performs invariantly during flexing, exhibiting capacitances of ~45 mF/cm^2 with 85% retention after 1600 cycles, suggesting potential applicability for providing energy storage in flexible devices.[41] IGA based capacitive devices incorporated into circuits have proven their functionality through applications such as line filtering, as shown in **Figure 3D**.

The transistor is an essential device for modern electronics. Its usage is multifaceted, and it is found in memory, optoelectronics, sensing, and many other devices. 2D materials offer several advantages in comparison to Si-based technology. For example, while transistor technologies are usually fabricated in a MOSFET configuration, solution processing can dramatically
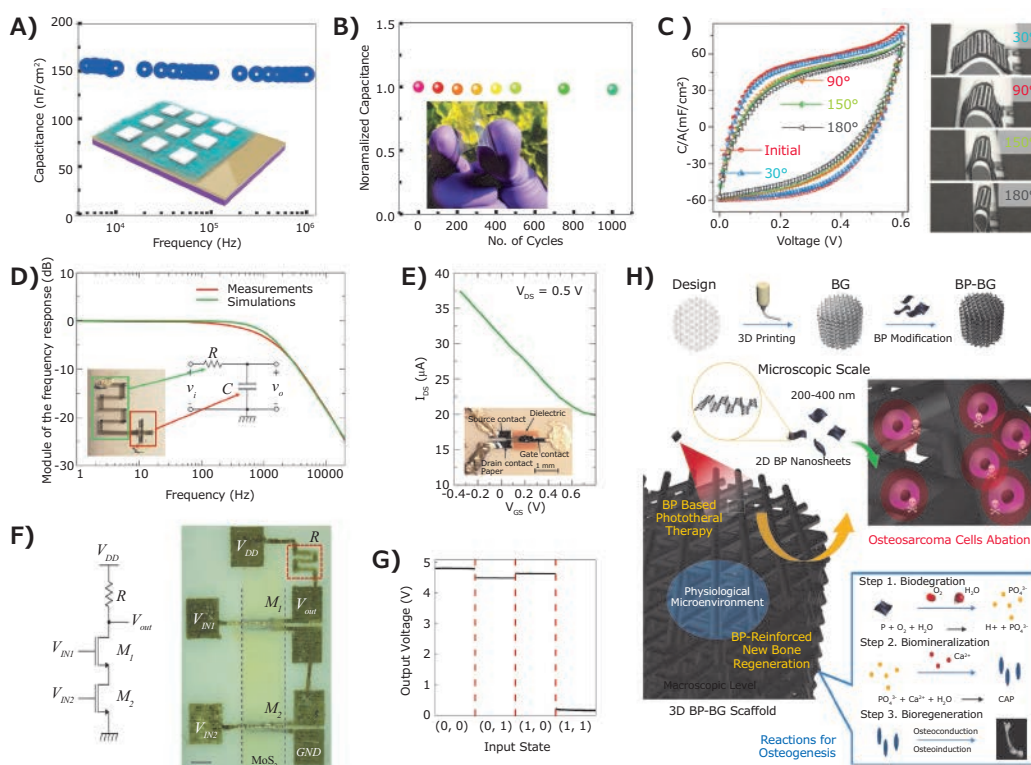
Figure 3. Applications of solution processed 2D materials. **A**) High frequency performance of h-BN based capacitive devices (schematic in inset) obtained through electrophoretic deposition and **B**) its performance under flexure. Adapted with permission from reference 27, copyright 2019 American Chemical Society. **C**) Low variation in capacitance of stamped flexible supercapacitor using MXene inks. Adapted with permission from reference 41, copyright 2018 Wiley-VCH. **D**) All-2D material inkjet printed circuits demonstrating application in line filtering and **E**) field effect transistor. Adapted with permission from reference 42, copyright 2018 American Chemical Society. **F**) Circuit diagram of a NAND gate, with a photograph of this circuit, realized using MoS$_2$ and its output voltage shown in **G**). Adapted with permission from reference 43, copyright 2019 Nature Publishing Group. **H**) 3D printed black phosphorus scaffolds utilized for applications in thermal treatment of osteosarcoma. Adapted with permission from reference 44, copyright 2018 Wiley-VCH.

simplify their fabrication and offer a cost effective solution for flexible printed electronics. Solution-processed FETs fabricated by spin coating of 2-H phase MoS$_2$ dispersions obtained by electrochemical intercalation of tetraheptylammonium bromide (**Cat. No. 87301**) have been reported to have mobilities of ~10 cm^{2}V^{-1}s^{-1} and high on-off ratios of ~10^6.[45] **Figure 3E** shows FETs printed using 2D materials alone, demonstrating the diversity in the electrical properties of these materials, and the great design flexibility. Fully inkjet-printed flexible and washable field effect transistors (FETs) using graphene and h-BN have been reported with mobilities of about 90 cm^{2}V^{-1}s^{-1}, however, with poor on-off ratios.[46] Using TMDs like WSe$_2$, an all-printed thin-film transistor with increased on-off ratios of ~600 and mobilities of ~ 0.2 cm^{2}V^{-1}s^{-1} have been achieved by gating using ionic liquids such as 1-ethyl 3-methylimidazolium bis(trifluoromethylsulfonyl)imide (**Cat. No. 900801**).[47] Inkjet-printed devices using graphene electrodes and WS$_2$ for photodetectors and memory devices have also been reported.[37] Transistors form a basic component in several functional circuits like logic gates, which are the building blocks for computing devices. **Figure 3F** shows the NAND gate's circuit diagram realized using CVD grown MoS$_2$, as shown in the photograph. The device operates at voltages below 2V, with mobilities reaching 26 cm^{2}V^{-1}s^{-1} and negligible leakage currents (below 5nA). The output voltage of such a circuit is shown in **Figure 3G**.

In the sensing domain, 2D materials provide a great platform for adsorption of analytes due to their large surface area and can also provide specificity by chemical nature. Compared to bilayers, multilayer MoS$_2$ was better at sensing gases such as NO$_2$, NH$_3$ and water vapor at ambient temperatures and pressures.[48] Dispersions of several IGAs have been made into freestanding films using simple techniques like vacuum filtration. The film structure, comprised of several layers of nanosheets, has proven effective as membranes for applications like filtration and low permeability packaging.[49] The incorporation of MoS$_2$ in polyethylene oxide by simple blending was shown to yield a strain sensor with an unusually negative gauge factor from the piezoresistive nature of the composite films.[50] Screen printed thermoelectric films of BiTeSe exhibited high figures of merit (ZT ~0.43) and performed well under flexure.[51] Extensive research to understand the biological implications of 2D materials and their possible uses in the field is underway.[52,53] **Figure 3H** shows a 3D printed scaffold incorporated with 2D nanosheets of black phosphorus, effective in the photothermal ablation of osteosarcoma cells.[44]

Outlook

From a birds-eye view, the vast expanse of 2D materials remains largely unchartered territory considering the possibility of thousands of theoretically predicted 2D materials with

various electronic, magnetic, and topological properties.[54] For their effective utilization through solution-processing, a more in-depth understanding of the role of precursor materials, solvents, pre- and post-processing protocols, and exfoliation strategies is crucial. In particular, both experimental and as theoretical scrutiny will be required to identify better and safer solvents. Given the rise of technologies such as the internet of things, electronic applications are a prospective area that holds tremendous potential for IGAs. Scalable fabrication using well-established protocols such as roll-to-roll processing could greatly ease their incorporation through solution routes.

In fast emerging technologies such as 3D printing, the demonstrated use of graphene indicates the possibility of integrating IGAs, that could appreciably expand the current boundaries of 2D materials. With the increasing use of these materials, other relevant aspects such as environmental effects and impact on biological systems will require attention. As of now, there is a limited understanding of such implications. An in-depth comprehension of biological interactions such as cytotoxicity, degradability, and accumulation will be required to help bridge the gap and facilitate their incorporation in advancing areas such as drug delivery, nanotheranostics, and bioelectronics. Therefore, there lies significant scope for exploring the many attributes possessed by this class of materials. The facile solution processable approaches that result from these studies could reach out across many diverse fields.

Acknowledgments

References

(1) de Arquer, F. P. G.; Armin, A.; Meredith, P.; Sargent, E. H. *Nat. Rev. Mater.* **2017**, *2*, 1–17.
(2) Stokes, P.; Khondaker, S. I. *Appl. Phys. Lett.* **2010**, *96*, 083110.
(3) Geier, M. L.; McMorrow, J. J.; Xu, W.; Zhu, J.; Kim, C. H.; Marks, T. J.; Hersam, M. C. *Nat. Nanotechnol.* **2015**, *10*, 944–948.
(4) Coleman, J. N.; Lotya, M.; O'Neill, A.; Bergin, S. D.; King, P. J.; Khan, U.; Young, K.; Gaucher, A.; De, S.; Smith, R. J. *Science* **2011**, *331*, 568–571.
(5) Biccai, S.; Barwich, S.; Boland, D.; Harvey, A.; Hanlon, D.; McEvoy, N.; Coleman, J. N. *2D Mater.* **2018**, *6*, 015008.
(6) Kang, J.; Seo, J.-W. T.; Alducin, D.; Ponce, A.; Yacaman, M. J.; Hersam, M. C. *Nat. Commun.* **2014**, *5*, 5478.
(7) Guardia, L.; Paredes, J. I.; Rozada, R.; Villar-Rodil, S.; Martínez-Alonso, A.; Tascón, J. M. RSC Adv. 2014, 4, 14115-14127.
(8) Hernandez, Y.; Nicolosi, V.; Lotya, M.; Blighe, F. M.; Sun, Z.; De, S.; McGovern, I.; Holland, B.; Byrne, M.; Gun'Ko, Y. K. *Nat. Nanotechnol.* **2008**, *3*, 563–568.
(9) Wang, M.; Xu, X.; Ge, Y.; Dong, P.; Baines, R.; Ajayan, P. M.; Ye, M.; Shen, J. *ACS Appl. Mater. Interface.* **2017**, *9*, 9168–9175.
(10) Nakamura, D.; Nakano, H. *Chem. Mater.* **2018**, 30, 5333–5338.
(11) Zhou, K. G.; Mao, N. N.; Wang, H. X.; Peng, Y.; Zhang, H. L. *Angew. Chem. Intern. Ed.* **2011**, *123*, 11031–11034.
(12) Shen, J.; Wu, J.; Wang, M.; Dong, P.; Xu, J.; Li, X.; Zhang, X.; Yuan, J.; Wang, X.; Ye, M. *Small* **2016**, *12*, 2741–2749.
(13) Gupta, A.; Arunachalam, V.; Vasudevan, S. *J. Phys. Chem. Lett.* **2016**, *7*, 4884–4890.
(14) Wang, Y.; Wang, K.; Zhang, C.; Zhu, J.; Xu, J.; Liu, T. *Small* **2019**, *15*, 1903816.
(15) Ogilvie, S. P.; Large, M. J.; O'Mara, M. A.; Lynch, P. J.; Lee, C. L.; King, A. A.; Backes, C.; Dalton, A. B. *2D Mater.* **2019**, *6*, 031002.
(16) Lobo, K.; Trivedi, S.; Matte, H. R. *Nanoscale* **2019**, *11*, 10746–10755.
(17) Halim, U.; Zheng, C. R.; Chen, Y.; Lin, Z.; Jiang, S.; Cheng, R.; Huang, Y.; Duan, X. *Nat. Commun.* **2013**, *4*, 1–7.
(18) Sresht, V.; Padua, A. A.; Blankschtein, D. *ACS Nano* **2015**, *9*, 8255–8268.
(19) Backes, C.; Berner, N. C.; Chen, X.; Lafargue, P.; LaPlace, P.; Freeley, M.; Duesberg, G. S.; Coleman, J. N.; McDonald, A. R. *Angew. Chem. Intern. Ed.* **2015**, *54*, 2638–2642.
(20) Ott, S.; Wolff, N.; Rashvand, F.; Rao, V. J.; Zaumseil, J.; Backes, C. *Chem. Mater.* **2019**, *31*, 8424–8431.
(21) Forsberg, V.; Zhang, R.; Bäckström, J.; Dahlström, C.; Andres, B.; Norgren, M.; Andersson, M.; Hummelgård, M.; Olin, H. *PloS One* **2016**, *11*, e0154522.
(22) Kang, J.; Wood, J. D.; Wells, S. A.; Lee, J.-H.; Liu, X.; Chen, K.-S.; Hersam, M. C. *ACS Nano* **2015**, *9*, 3596–3604.
(23) Bonaccorso, F.; Bartolotta, A.; Coleman, J. N.; Backes, C. *Adv. Mater.* **2016**, *28*, 6136–6166.
(24) Patil, U.; Caffrey, N. M. *J. Chem. Phys.* **2018**, *149*, 094702.
(25) Backes, C.; Szydłowska, B. M.; Harvey, A.; Yuan, S.; Vega-Mayoral, V.; Davies, B. R.; Zhao, P.-I.; Hanlon, D.; Santos, E. J.; Katsnelson, M. I. *ACS Nano* **2016**, *10*, 1589–1601.
(26) Kang, J.; Sangwan, V. K.; Wood, J. D.; Hersam, M. C. *Acc. Chem. Res.* **2017**, *50*, 943–951.
(27) Gupta, B.; Matte, H. R. *ACS Appl. Electron. Mater.* **2019**, *1*, 2130–2139.
(28) Jang, D.; Kim, D.; Moon, J. *Langmuir* **2009**, *25*, 2629–2635.
(29) Finn, D. J.; Lotya, M.; Cunningham, G.; Smith, R. J.; McCloskey, D.; Donegan, J. F.; Coleman, J. N. *J. Mater. Chem. C* **2014**, *2*, 925–932.
(30) He, P.; Cao, J.; Ding, H.; Liu, C.; Neilson, J.; Li, Z.; Kinloch, I. A.; Derby, B. *ACS Appl. Mater. Interface.* **2019**, *11*, 32225–32234.
(31) Orangi, J.; Hamade, F.; Davis, V. A.; Beidaghi, M. *ACS Nano* **2019**, *14*, 640–650.
(32) Xiong, P.; Sun, B.; Sakai, N.; Ma, R.; Sasaki, T.; Wang, S.; Zhang, J.; Wang, G. *Adv. Mater.* **2020**, *32*, 1902654.
(33) Zhang, Y.; Xu, L.; Walker, W. R.; Tittle, C. M.; Backhouse, C. J.; Pope, M. A. *J. Mater. Chem. C* **2017**, *5*, 11275–11287.
(34) Torrisi, F.; Coleman, J. N. *Nat. Nanotechnol.* **2014**, *9*, 738–739.
(35) Barwich, S.; de Araújo, J. M.; Rafferty, A.; da Rocha, C. G.; Ferreira, M. S.; Coleman, J. N. *Carbon* **2020**, *171*, 306–3019.
(36) Nalawade, Y.; Pepper, J.; Harvey, A.; Griffin, A.; Caffrey, D.; Kelly, A. G.; Coleman, J. N. *ACS Appl. Electron. Mater.* **2020**, *2* (10), 3233–3241.
(37) McManus, D.; Vranic, S.; Withers, F.; Sanchez-Romaguera, V.; Macucci, M.; Yang, H.; Sorrentino, R.; Parvez, K.; Son, S.-K.; Iannaccone, G.; Kostarelos, K.; Fiori, G.; Casiraghi, C. Nat. *Nanotechnol.* **2017**, *12*, 343–350.
(38) Hu, G.; Albrow-Owen, T.; Jin, X.; Ali, A.; Hu, Y.; Howe, R. C.; Shehzad, K.; Yang, Z.; Zhu, X.; Woodward, R. I. *Nat. Commun.* **2017**, *8*, 1–10.
(39) Xu, S.; Dall'Agnese, Y.; Wei, G.; Zhang, C.; Gogotsi, Y.; Han, W. *Nano Energy* **2018**, *50*, 479–488.
(40) Hassan, K.; Nine, M. J.; Tung, T. T.; Stanley, N. J.; Yap, P. L.; Rastin, H.; Yu, L.; Losic, D. *Nanoscale* **2020**, *12*, 19007.
(41) Zhang, C.; Kremer, M. P.; Seral Ascaso, A.; Park, S. H.; McEvoy, N.; Anasori, B.; Gogotsi, Y.; Nicolosi, V. *Adv. Funct. Mater.* **2018**, *28*, 1705506.
(42) Worsley, R.; Pimpolari, L.; McManus, D.; Ge, N.; Ionescu, R.; Wittkopf, J. A.; Alieva, A.; Basso, G.; Macucci, M.; Iannaccone, G. *ACS Nano* **2018**, *13*, 54–60.
(43) Conti, S.; Pimpolari, L.; Calabrese, G.; Worsley, R.; Majee, S.; Polyushkin, D. K.; Paur, M.; Pace, S.; Keum, D. H.; Fabbri, F. *Nat. Commun.* **2020**, *11*, 1–9.
(44) Yang, B.; Yin, J.; Chen, Y.; Pan, S.; Yao, H.; Gao, Y.; Shi, J. *Adv. Mater.* **2018**, *30*, 1705611.
(45) Lin, Z.; Liu, Y.; Halim, U.; Ding, M.; Liu, Y.; Wang, J.; Jia, C.; Chen, P.; Duan, X.; Wang, C. *Nature* **2018**, *562*, 254–258.
(46) Carey, T.; Cacovich, S.; Divitini, G.; Ren, J.; Mansouri, A.; Kim, J. M.; Wang, C.; Ducati, C.; Sordan, R.; Torrisi, F. *Nat. Commun.* **2017**, *8*, 1–11.
(47) Kelly, A. G.; Hallam, T.; Backes, C.; Harvey, A.; Esmaeily, A. S.; Godwin, I.; Coelho, J.; Nicolosi, V.; Lauth, J.; Kulkarni, A. *Science* **2017**, *356*, 69–73.
(48) Late, D. J.; Huang, Y.-K.; Liu, B.; Acharya, J.; Shirodkar, S. N.; Luo, J.; Yan, A.; Charles, D.; Waghmare, U. V.; Dravid, V. P. *ACS Nano* **2013**, *7*, 4879–4891.
(49) Li, W.; Yang, Y.; Weber, J. K.; Zhang, G.; Zhou, R. *ACS Nano* **2016**, *10*, 1829–1835.
(50) Biccai, S.; Boland, C. S.; O'Driscoll, D. P.; Harvey, A.; Gabbett, C.; O'Suilleabhain, D. R.; Griffin, A. J.; Li, Z.; Young, R. J.; Coleman, J. N. *ACS Nano* **2019**, *13*, 6845–6855.
(51) Varghese, T.; Hollar, C.; Richardson, J.; Kempf, N.; Han, C.; Gamarachchi, P.; Estrada, D.; Mehta, R. J.; Zhang, Y. *Sci. Rep.* **2016**, *6*, 33135.
(52) Ma, B.; Martín, C.; Kurapati, R.; Bianco, A. *Chem. Soc. Rev.* **2020**, *49*, 6224–6247.
(53) Kurapati, R.; Kostarelos, K.; Prato, M.; Bianco, A. *Adv. Mater.* **2016**, *28*, 6052–6074.
(54) Mounet, N.; Gibertini, M.; Schwaller, P.; Campi, D.; Merkys, A.; Marrazzo, A.; Sohier, T.; Castelli, I. E.; Cepellotti, A.; Pizzi, G. *Nat. Nanotechnol.* **2018**, *13*, 246–252.

Transition Metal Dichalcogenides (TMDCs)

MoS$_2$

Name	Description	Cat. No.
Molybdenum disulfide ink for spin/spray coating	Resistivity: 75-100 kΩ·cm	901867-10ML
Molybdenum disulfide nanoplatelets	50-1000 nm thickness < 3 layers	901792-250MG
Molybdenum disulfide quantum dots	-	914541-50ML 914541-20ML
Molybdenum disulfide suspension	50-1000 nm thickness < 3 layers	901797-50ML
	50-1000 nm thickness < 3 layers	902012-25ML
Molybdenum sulfide	single crystalline monolayer flakes on SiO$_2$/Si	901479-1EA
	Single crystalline monolayer flakes on sapphire	901615-1EA
Molybdenum disulfide	-	900724-10ML

WS$_2$

Name	Description	Cat. No.
Tungsten disulfide nanoplatelets	50-300 nm thickness < 3 layers	901789-250MG
Tungsten disulfide quantum dots	-	914290-20ML 914290-50ML
Tungsten disulfide suspension	50-300 nm thickness < 3 layers	901791-50ML
	thickness < 3 layers 50-300 nm	901775-25ML
Tungsten sulfide	single crystalline monolayer flakes on sapphire	901474-1EA
	single crystalline monolayer flakes on SiO$_2$/Si	901484-1EA
Tungsten(IV) sulfide	-	790583-5G

MoSe$_2$

Name	Description	Cat. No.
Molybdenum selenide	single crystalline monolayer flakes on SiO$_2$/Si	901473-1EA
	single crystalline monolayer flakes on sapphire	901467-1EA

WSe$_2$

Name	Description	Cat. No.
Tungsten selenide	single crystalline monolayer flakes on sapphire	901483-1EA
	single crystalline monolayer flakes on SiO$_2$/Si	901478-1EA

MXene Precursor-MAX Phases

Name	Form	Particle Size (µm)	Purity	Cat. No.
Titanium aluminium carbide 211	powder	≤100	≥80%	910821-25G
	powder	≤200	≥80%	910708-25G
Titanium aluminium carbide 312	powder	≤40	≥90%	910775-25G
	powder	≤100	≥90%	910767-25G
	powder	≤200	≥90%	910740-25G
Titanium aluminium carbide 211	powder	≤40	≥80%	910759-25G

Etchants

Name	Purity	Form	Cat. No.
Lithium fluoride	99.995%	powder	669431-50G
	≥99.99% trace metals basis	powder and chunks	449903-2G 449903-10G
	≥99.98% trace metals basis	powder	203645-5G 203645-25G
	-	powder	237965-100G 237965-1KG
Hydrochloric acid	99.999% trace metals basis	liquid	339253-100ML 339253-500ML
Buffer HF improved	-	liquid	901657-1L
	-	liquid	901667-1L

Name	Purity	Form	Cat. No.
Hydrofluoric acid	≥99.99% trace metals basis	liquid	**339261-100ML** **339261-4X100ML**
	≥48%	liquid	**30107-500ML** **30107-1L** **30107-6X1L**
	≥40%	liquid	**30103-1L** **30103-6X1L** **30103-2.5L**
	48%	liquid	**695068-25ML** **695068-500ML**
Lithium fluoride	99.995%	fused (pieces)	**668052-10G** **668052-25G** **668052-100G**

BNNTs

Name	Composition	Form	Purity	Cat. No.
Boron nitride nanotubes	BN	nanotubes powder	>70%	**913332-250MG** **913332-1G**
	BN	nanotubes powder	>90%	**912085-500MG** **912085-100MG**
	BN	nanotubes powder	>80%	**919500-250MG** **919500-1G**

Conductive Inks for Printed Electronics

Screen Printing Inks

Name	Sheet Resistance	Viscosity	Cat. No.
Carbon/graphite screen printing paste	< 50Ω/square at 25 µm (printed through 230 stainless steel mesh with 13 micron emulsion)	2.0-3.5 Pa.s	**901969-200G**
Flexible conductive silver paste for screen printing	925 ohm cm at 60 °C 527 ohm cm at 130 °C	0.72-1.78 Pa.s	**901769-25G** **901769-100G**
Silver/silver chloride (60/40) paste for screen printing,	<100 miliohms per square (20 micron thick printed on alumina substrate)	2.0-5.5 Pa.s	**901773-50G**
Graphene ink in water	10 Ω/sq (at 25 µm thickness)	350 cP $(100s^{-1})$ 1800 cP $(1000s^{-1})$	**808261-10ML**
Graphene ink, for screen printing with ethyl cellulose in terpineol, screen printable	0.003-0.008 Ω-cm (thermally annealed 300 °C for 30 minutes, film thickness >100 nm, 25 °C)	5-50 Pa.s	**798983-10ML**
Conductive silver printing ink, resistivity 5-6 µΩ cm	5-6 µΩ-cm	13,000-17,000 mPa.s	**791873-10G** **791873-20G**
Platinum paste, screen printable	-	2500-4500 mPa.s	**791512-20G**
SunTronic® conductive silver ink for screen printing	<0.010 Ω/sq/mil (150 °C/10 min)	45-55 Pa.s	**901879-25G**

Inkjet Printing Inks

Name	Sheet Resistance	Viscosity	Cat. No.
SunTronic® silver nanoparticle ink for inkjet printing	-	11-13 cP	**901971-2ML** **901971-10ML**
Conductive nanosilver ink for inkjet printing, Silver content:18-20%W/W	-	10-18 mPa.s	**907022-25ML**
Copper inkjet ink, Cu(0) in Cu nanoparticles: >95%	-	32 cP	**907413-5ML**
Graphene ink in water, inkjet printable	4k Ω/sq (80 nm thickness)	1 cP $(100s^{-1})$	**808288-5ML**
Graphene ink, for inkjet printing with ethyl cellulose in cyclohexanone and terpineol	0.003-0.008 Ω-cm (thermally annealed 250 °C for 30 minutes, film thickness >100 nm)	8-15 mPa.s	**793663-5ML**
Poly(3,4-ethylenedioxythiophene)-poly(styrenesulfonate), conductive inkjet ink	110 Ω/sq	7-12 cP	**739316-25G**
SunTronic® silver nanoparticle ink for inkjet printing	-	6-8 cP	**901975-2ML** **901975-10ML**

Flexographic Printing

Name	Sheet Resistance	Viscosity	Cat. No.
SunTronic®aqueous silver flexo ink	15 mΩ/sq/mil	19-21 poise	**901876-20G**
Graphene ink in water, flexo/gravure/screen printable	10 Ω/sq (25µm thickness)	570 cP $(100s^{-1})$ 140 cP $(1000s^{-1})$	**805556-10ML**
SunTronic® conductive graphite ink for flexographic printing	<100 Ω/sq (flexo printed on SBS board with 18 BCM anilox roll)	1300-1700 cP	**901970-250G**

Laser-Induced Forward Transfer (LIFT) Printing

Name	Sheet Resistance (μΩ-cm)	Viscosity	Cat. No.
Conductive silver printing ink	30-35 μΩ-cm (at a 180 °C cure temperature)	6000-9000 mPa.s	791903-10G 791903-20G
Silver ink, 75 wt%, LIFT printable	-	50,000-100,000 cP	907669-5G

3D Printing

Name	Sheet Resistance	Viscosity At 20 °C (Pa.s)	Cat. No.
3D printing graphene ink	0.12-0.15 Ω-cm (as 3D-printed fibers, not ink, 200-400 μm diameter)	25-45	808156-5ML
3D printing graphite ink	-	20-60	901662-5ML 901662-25ML

Gravure Printing

Name	Sheet Resistance (Ω-cm)	Viscosity At 25 °C (Pa.s)	Cat. No.
Graphene ink, for gravure printing with ethyl cellulose in terpineol	0.003-0.008 (thermally annealed 250 °C for 30 minutes, film thickness >100 nm)	0.75-3	796115-10ML

Dielectric Inks for Printed Electronics

Inkjet Printing Ink

Name	Sheet Resistance	Viscosity (cP)	Cat. No.
SunTronic® UV curing jettable insulator for low-K dielectric applications	-	11-13	901974-250ML

Screen Printing Inks

Name	Coverage	Viscosity	Cat. No.
Polymer dielectric grey for screen printing	305 cm² per g (using a 230 mesh stainless steel screen with 13 micron emulsion)	12.0-16.0 Pa.s	902497-250G
Polymer dielectric blue for screen printing	800 cm² per g (using a 230 mesh stainless steel screen)	5.5-8.0 Pa.s	902365-250G
SunTronic® UV curing dielectric green for screen printing	32-35 m²/kg/mil	20-30 poise	901973-250G

Interficial Inks for Printed Electronics

Slot-Die, Doctor Blade, or Spin Coating

Name	Work Function	Viscosity At 20 °C	Cat. No.
Tungsten oxide (WO$_{3-x}$) nanoparticle ink	-	-	793353-5ML 793353-25ML 793353-50ML
Zinc oxide ink for spin coating/slot-die coating	4.0 ± 0.1 eV	<4 mPa.s	901081-25ML
Zinc oxide nanoparticle ink	-	-	793361-5ML 793361-25ML 793361-50ML
Zinc oxide nanoparticle ink, 2.5 wt. %	-3.9eV	1.6-2.6 cP	808253-10ML 808253-50ML
Aluminum-doped zinc oxide ink for spin coating/slot-die coating	3.6 ± 0.1 eV	<4 mPa.s	901092-25ML
Aluminum-doped zinc oxide nanoparticle ink, 2.5 wt. %	-4.3eV	1.9-3.1 cP	807729-10ML 807729-50ML
Aluminum-doped zinc oxide nanoparticle ink, 2.5 wt. %	-3.9 eV	1.7-2.7 cP	808237-10ML 808237-50ML
Molybdenum oxide nanoparticle ink	-	1-3 cP	900151-10ML

Inkjet Printing

Name	Work Function	Viscosity At 20 °C	Cat. No.
Zinc oxide nanoparticle ink, 2.5 wt. %	-4.3eV	8-14 cP	807613-5ML 807613-10ML 807613-50ML
Zinc oxide nanoparticle ink, 2.5 wt. %	-4.3eV	2.4-3.8 cP	807648-10ML 807648-50ML
Tungsten oxide nanoparticle ink	-	8 cP	807753-5ML 807753-25ML 807753-50ML
Aluminum-doped zinc oxide ink for inkjet printing	3.6 ± 0.1 eV	10 mPa.s ±3 mPa.s	901065-25ML
Aluminum-doped zinc oxide nanoparticle ink, 2.5 wt. %	-4.3eV	2.4-4.0 cP	807656-10ML 807656-50ML

Name	Work Function	Viscosity At 20 °C	Cat. No.
Aluminum-doped zinc oxide nanoparticle ink, 2.5 wt. %	-3.9eV	2.5-3.7 cP	808164-10ML 808164-50ML
Aluminum-doped zinc oxide nanoparticle ink, 2.5 wt. %	-4.3eV	8-14 cP	808172-5ML 808172-10ML 808172-50ML
Aluminum-doped zinc oxide nanoparticle ink, 2.5 wt. %	-3.9eV	8-14 cP	808180-5ML 808180-10ML 808180-50ML
Zinc oxide nanoparticle ink, 2.5 wt. %	-3.9eV	8-14 cP	808202-5ML 808202-10ML 808202-50ML

Screen Printing

Name	Work Function	Viscosity	Cat. No.
Zinc oxide nanoparticle ink, 2.5 wt. %	-3.9eV	32-48 cP	808075-10ML 808075-50ML
Titania paste, active opaque	-	40000-55000 mPa.s	791555-5G 791555-20G
Titania paste, reflector	-	15000-25000 mPa.s	791539-5G 791539-20G
Titania paste, transparent	-	40000-55000 mPa.s	791547-10G 791547-20G
Aluminum-doped zinc oxide nanoparticle ink, 2.5 wt. %	-4.3eV	25-37 cP	808210-10ML 808210-50ML
Aluminum-doped zinc oxide nanoparticle ink, 2.5 wt. %	-3.9eV	32-48 cP	808229-10ML 808229-50ML
Zinc oxide nanoparticle ink, 2.5 wt. %	-4.3eV	26-36 cP	807621-10ML 807621-50ML

Common Solvents for Thin Films

Name	Purity	Form	Cat. No.
Cyrene™	≥98.5%, GC	liquid	807796-100ML 807796-1L
N,N-Dimethylformamide	99.8%	liquid	227056-100ML 227056-250ML 227056-1L 227056-2L
Dimethyl sulfoxide	≥99.9%	liquid	276855-100ML 276855-250ML 276855-1L 276855-2L
2-Propanol	99.5%	liquid	278475-100ML 278475-250ML 278475-1L 278475-2L
Acetone	≥99.5%	liquid (clear)	179124-500ML 179124-1L 179124-2.5L
2-Butanone	≥99.0%	liquid	360473-500ML 360473-1L 360473-2L 360473-2.5L
Ethyl alcohol, Pure	≥99.5%	liquid	459836-100ML 459836-500ML 459836-1L 459836-2L
Methanol	99.8%	liquid	322415-100ML 322415-250ML 322415-1L 322415-2L
Toluene	99.8%	liquid	244511-100ML 244511-250ML 244511-1L 244511-2L
m-Xylene	≥99%	liquid	296325-100ML 296325-1L 296325-2L
p-Xylene	≥99%	liquid	296333-100ML 296333-1L 296333-2L
o-Xylene	97%	liquid	294780-100ML 294780-1L 294780-2L

Name	Purity	Form	Cat. No.
Chloroform	≥99%	liquid	288306-100ML 288306-900ML 288306-1L 288306-2L
Chlorobenzene	99.8%	liquid	284513-100ML 284513-250ML 284513-1L 284513-2L
1,2-Dichlorobenzene	99%	liquid	240664-100ML 240664-1L 240664-2L
1,4-Dichlorobenzene	≥99%	crystalline solid	D56829-25G D56829-100G D56829-500G
1,3-Dichlorobenzene	≥99.0%, GC	-	35350-100ML 35350-500ML
1,2,4-Trichlorobenzene	≥99%	solid or liquid	296104-100ML 296104-1L 296104-2L
1,3,5-Trichlorobenzene	99%	powder or crystals	T54607-100G T54607-500G
1,8-Diiodooctane	98%	-	250295-5G
1,8-Octanedithiol	≥97%	-	O3605-1G O3605-5G
Glycerol	≥99.5%	-	G9012-100ML G9012-500ML G9012-1L G9012-2L
1-Methyl-2-pyrrolidinone	99.5%	liquid	328634-100ML 328634-250ML 328634-1L 328634-2L

Recent Advances in the Fabrication of High-stability Metal Halide Perovskite-Based Solar Cells and Modules

Zonghao Liu,[1*] Yabing Qi[2*]

[1] Wuhan National Laboratory for Optoelectronics, Huazhong University of Science and Technology, Wuhan, China
[2] Energy Materials and Surface Sciences Unit (EMSSU), Okinawa Institute of Science and Technology Graduate University (OIST), 1919-1 Tancha, Onna-son, Kunigami-gun, Okinawa 904-0495, Japan
* Email: liuzonghao@hust.edu.cn; Yabing.Qi@OIST.jp

Introduction

Perovskite solar cells (PSCs) have emerged as one of the most promising thin-film photovoltaic (PV) technologies and have made a strong debut in the PV field based on their high power conversion efficiencies (PCEs) and low-cost facile fabrication.[1] However, PSCs face two critical challenges on the road to their commercialization: 1) upscaling to module scale[2–4] and 2) long-term stability.[5–6]

Any mature PV technology must be suitable for mass production at a module scale to meet practical application requirements. Lab-scale PCE devices with a size below 1 cm^2 have achieved a record high certified PCE of 25.5% using a spin coating method.[7] However, it is difficult to directly apply this approach to the fabrication of perovskite solar modules (PSMs) and reach an efficiency level similar to other commercialized solar modules.[4] The record PCEs of perovskite solar mini modules (PCE = 18.6%, designated area = 29.539 cm^2, UNCarolina, 8 serial cells) and modules (PCE = 17.9%, designated area = 802 cm^2, Panasonic, 55 cells) has only reached around 18%, substantially lower than other commercial solar modules.[7] Scalable fabrication methods need to be developed to deposit all the functional layers and to boost the efficiency of PSMs, including electron and hole transport layers, the perovskite layer, electrode, the encapsulation layer, and suitable material development.

In addition to high efficiency, instability is another crucial issue impeding the commercialization of PSCs. Due to the soft nature of perovskite materials their degradation can happen under various stressors, such as oxygen, moisture, heat, light, and electric bias.[8] Other functional layers may also degrade under these stressors or react with the by-products from perovskite degradation, causing instability of the whole solar cell device.[6] Effective strategies to improve stability of PSCs include

composition engineering of the perovskite layer using mixed cation perovskites,[9] structural engineering by incorporating bulky alkylamine cations, polymers, ionic liquids or other additives,[10] engineering of other functional layers (including charge transport layers,[11–13] barrier layers,[14] electrode[15]), and encapsulation.[16] Here, we review recent advances in the fabrication of high-stability metal halide perovskite-based solar cells and modules.

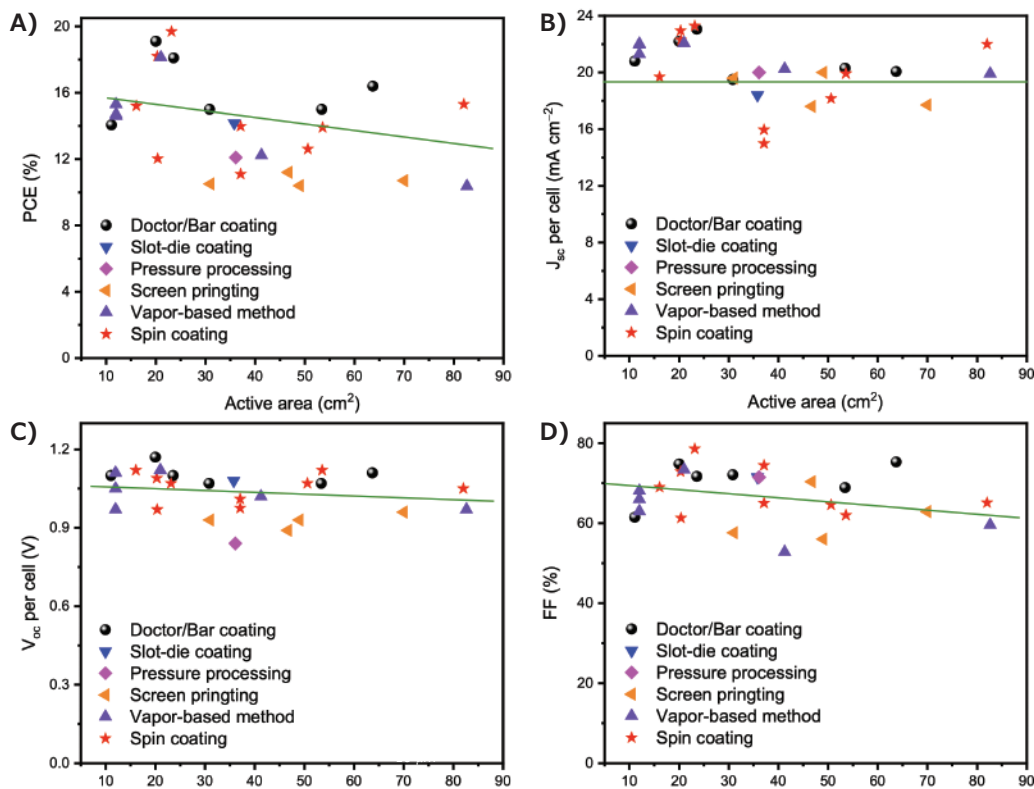## Fabrication of High-stability Metal Halide Perovskite-based Solar Cells and Solar Modules

In the last decade, the stability of PSCs has been dramatically improved, with lifetimes increasing from several minutes to thousands of hours through the engineering of perovskite and other functional layers. Many successful stability improvement strategies have also been employed in PSMs to drive this emerging photovoltaic technology towards practical application. **Table 1** lists selected studies that report PSMs with a total area exceeding 10 cm^2 and provide module stability testing results. Based on **Table 1**, we analyzed the device performance parameters as a function of the device area, shown in **Figure 1**. The decrease of PCE mainly comes from the decrease of open circuit voltage (V_{oc}) and fill factor (FF) resulting from the difficulty in fabricating uniform active layers (especially the perovskite and charge transport layers) over large-area substrates. The higher probability of forming pinholes and defects significantly affects V_{oc} and FF. Therefore, a critical factor in realizing highly efficient and stable solar modules is the development of scalable processes to coat high-quality, uniform, large-area active layers (including the perovskite and charge transport layers).

Table 1. Selected reports that report perovskite solar modules with a total area exceeding 10 cm² and provide module stability testing results. ac, active area; ap, aperture area; da, designated area (active area + dead area for interconnections). CE, certified efficiency; ITO, indium tin oxide; FTO, fluorine doped tin oxide; c-TiO_2, compact TiO_2; mp, mesoporous TiO_2; spiro-OMeTAD, 2,2',7,7'-tetrakis(N,N-di-4-methoxyphenylamino)-9,9'-spirobifluorene; PCBM, [6,6]-phenyl-C60,61 butyric acid methyl ester; PTAA, poly[bis(4-phenyl)(2,4,6-trimethylphenyl)amine]; PEDOT:PSS, poly(3,4-ethylenedioxythiophene):poly(styrenesulfonate); P3HT, poly(3-hexylthiophene-2,5-diyl) regioregular; 5-AVA, 5-aminovaleric acid. The device performance values are mainly obtained from current-voltage curves.

Module structure	PCE (%)	V_{oc} (V)	J_{sc} (mA/cm^{-2})	FF (%)	Cells	GFF (%)	Area (cm²)	Perovskite deposition method	Module or cell stability test condition	Ref.
FTO/c-TiO_2/MAPbI$_3$/spiro-OMeTAD/Ag	14.06^{ac}	4.4	~20.8	61.5	4	88	11.09^{ac}	Doctor blading	In air, storage, PSC, T_{80}=3000 h	[17]
ITO/PTAA/MAPbI$_3$/C60/BCP/Cu	15^{ap} (14.6^{SE})	~17.1	20.3	68.9	16	93.4	57.2^{ap}	Doctor blading	Dark, N$_2$, storage, PSM, T_{100}=480 h	[18]
	15^{ap} (15.3^{SE})	~18.2	19.5	72.1	17	93.4	33^{ap}	Doctor blading	Dark, N$_2$, storage, PSM, T_{100}=480 h	[18]
ITO/PTAA/MAPbI$_3$/C60/BCP/Cu	16.9^{ap} (16.4^{CE})	18.9	1.18^{ap}	75.3	17	93.4	63.7^{ap}	Doctor blading	1 Sun equivalent light, MPP, Encapsulated PSM, T_{87}=1000 h	[19]
FTO/c-TiO_2/mp-TiO_2/MAPbI$_3$/spiro-OMeTAD/Au	15.7^{ap} (12.1^{CE})	10.5(8.36^{CE})	2^{ap} (2^{CE})	75.7(71.5^{CE})	10	N/A	36.1^{ap}	Pressure processing	0.1 Sun UV-filtered simulated sunlight, 45 °C in ambient air, MPP, Encapsulated PSM, T_{90}=500 h	[20]
ITO/C60/MAPbI$_3$/spiro-OMeTAD/Au	13.98^{CE,ac}	14.10	1.14^{ac}	74.45	14	N/A	37.1^{ac}	Evaporation/spin coating	N$_2$, 30 °C, storage, Encapsulated PSM, storage, T_{60}=384 h;	[21]
ITO/C60/MAPbI$_3$/spiro-OMeTAD/Cu	11.09^{ac}	13.65	1.07^{ac}	65	14	N/A	37.1^{ac}	Evaporation/spin coating	N$_2$, 30 °C, storage, Encapsulated PSM, storage, T_{90}=720 h;	
ITO/PTAA/MAPbI$_3$/C60/BCP/Cu	18.0^{ap} (17.8^{SE})	~7	~3.44^{ap}	~74.8	6	93	21.5^{ap}	Blade coating	1 Sun equivalent light, 35 °C, Encapsulated PSM, MPP with resistors, T_{90}=400 h	[22]
FTO/NiO/FA$_{0.85}$MA$_{0.15}$Pb(I$_{0.85}$Br$_{0.15}$)$_3$/G-PCBM/BCP/Ag	15.6^{da} (14.17^{CE})	~11.1(10.8^{CE})	~1.92^{da} (1.84^{CE})	~73.2(71.5)	10	N/A	35.8^{da}	Slot-die	85 °C, RH 85%, Encapsulated PSM, T_{95}=1000 h; 1 Sun with UV filter, 60 °C, Encapsulated PSM, MPP, T_{91}=1000 h;	[23]
FTO/TiO_2/SnO$_2$/PCBM/MAPbI$_3$/spiro-OMeTAD/Au	18.13^{ac}	6.71	3.68^{ac}	73.4	6	72	21^{ac}	Thermally co-evaporated	1 Sun, N$_2$, RH 5%, unencapsulated PSM, MPP, T_{90}=100 h; 65 °C, RH 5%, unencapsulated PSM, T_{80}=100 h; RH 35%, unencapsulated PSM, storage, T_{95}=1440 h;	[24]
FTO/SnO$_2$/C60/Cs$_{0.1}$FA$_{0.9}$PbI$_3$/spiro-OMeTAD/Au	9.34^{da}	13.55	1.15^{da}	59.6	14	90	91.8^{da}	HCVD	1 Sun, N$_2$, 25 °C, Encapsulated PSM, MPP, T_{80}=500 h	[25]
FTO/c-TiO_2/Cs$_{0.07}$FA$_{0.93}$PbI$_3$/spiro-OMeTAD/Au	14.6^{ac}	5.84	3.67^{ac}	68.1	6	N/A	12^{ac}	HCVD	1 Sun, RH 60%, unencapsulated PSC, MPP, T_{56}=1000 min; 1 Sun, N$_2$, RH 5%, unencapsulated PSC, MPP, T_{100}=1200 min	[26]
FTO/c-TiO_2/FAPb(I$_{0.85}$Br$_{0.15}$)$_3$/spiro-OMeTAD/Au	14.7^{ac}	6.29	3.55^{ac}	66	6	N/A	12^{ac}	HCVD	Dark, N$_2$, unencapsulated PSM, storage, $T_{96.4}$=3600 h; 1 Sun, N$_2$, RH 5%, unencapsulated PSC, MPP, T_{80}=535 h; 1 Sun, N$_2$, RH 5%, unencapsulated PSM, MPP, T_{80}=388 h	[27]
FTO/SnO$_2$/Cs$_x$FA$_{1-x}$PbI$_{3-y}$Br$_y$/spiro-OMeTAD/Au	12.24^{ac}	9.18	2.25^{ac}	52.8	9	N/A	41.25^{ac}	HCVD	30 °C, RH 30%, unencapsulated PSM, storage, T_{83}=200 h; 60 °C, RH 30%, unencapsulated PSM, storage, T_{80}=200 h;	[28]
FTO/c-TiO_2/mp-TiO_2/MAPbI$_{3-x}$Cl$_x$/spiro-OMeTAD/Au	15.3^{ac}	6.65	3.66^{ac}	63.0	6	N/A	12^{ac}	Gas-solid process	1 Sun, N$_2$, RH 5%, unencapsulated PSC, MPP, T_{80}=1660 h	[29]
FTO/SnO$_2$/(FA$_{0.85}$MA$_{0.15}$)$_{0.95}$Pb(I$_{0.85}$Br$_{0.15}$)$_3$/spiro-OMeTAD/Au	13.9^{ac}	13.38	1.66^{ac}	62.0	12	N/A	53.6^{ap}	Spin coating/Solvent bath process	In air, RH 20%, storage, Unencapsulated PSC, T_{85}=500 h	[30]
PET/ITO/SnO$_2$/Cs$_{0.05}$(FA$_{0.85}$MA$_{0.15}$)$_{0.95}$Pb(I$_{0.85}$Br$_{0.15}$)$_3$/spiro-OMeTAD/Au	15.2^{ap}	6.727	3.28^{ac}	69	6	N/A	16.07^{ap}	Spin coating/antisolvent	Dark, RH 20%, unencapsulated PSM, storage, T_{80}=1000 h;	[31]
FTO/c-TiO_2/mp-TiO_2/(FAPbI$_3$)$_{0.95}$(MAPbBr$_3$)$_{0.05}$/WBH/P3HT/Au	17.1^{da}	8.78	2.72^{da}	71.7	8	94.4	24.97^{da}	Spin coating	RH 85%, RT, storage Unencapsulated PSC, T_{80}=1008 h; 1 Sun, MPP, Encapsulated PSC, T_{95}=1370 h	[32]
FTO/c-TiO_2/mp-TiO_2/(FAPbI$_3$)$_{0.95}$(MAPbBr$_3$)$_{0.05}$/WBH/P3HT/Au	17.1^{da}	8.66	2.72^{da}	72.6	8	94.4	24.97^{da}	Bar coating	RH 85%, RT, storage Unencapsulated PSC, T_{80}=1008 h; 1 Sun, MPP, Encapsulated PSC, T_{95}=1370 h	[32]
FTO/SnO$_2$/ (CsPbI$_3$)$_{0.05}$((FAPbI$_3$)$_{1-x}$(MAPbBr$_3$)$_x$)$_{0.95}$/spiro-OMeTAD/Au	17.88^{CE,ap}	7.52	3.02^{da}	78.6	7	90.8	25.49^{ap}	Spin coating	Dark, storage, Encapsulated PSM, T_{90}=5040 h;	[33]
SnO$_2$-EDTAK/Cs$_{0.05}$FA$_{0.54}$MA$_{0.41}$Pb(I$_{0.98}$Br$_{0.02}$)$_3$/spiro-OMeTAD-P3HT/Au	16.6^{da}	7.64	2.99^{da}	72.9	7	91	22.4^{da}	Spin coating	1 Sun, N$_2$, 40 °C, Encapsulated PSM, MPP, T_{90}=1570 h, T_{80}=2680 h; RH 5%, 60 °C, Encapsulated PSM, T_{80}=1000 h	[34]

Module structure	PCE (%)	V_{oc} (V)	J_{sc} (mA/cm^{-2})	FF (%)	Cells	GFF (%)	Area (cm²)	Perovskite deposition method	Module or cell stability test condition	Ref.
FTO/c-TiO$_2$/mp-TiO$_2$/Graphene/ MAPbI$_3$/spiro-OMeTAD/Au	12.6[ac]	8.57	2.27[ac]	64.6	8	N/A	50.6[ac]	Spin coating/Doctor blading	ISOS-D-1, storage, T$_{80}$=1630 h	[35]
FTO/c-TiO$_2$/mp-TiO$_2$/Graphene/ (Cs$_{0.01}$FA$_{0.79}$MA$_{0.15}$)Pb(I$_{0.85}$Br$_{0.15}$)$_3$/MoS$_2$/ spiro-OMeTAD/Au	15.3[ac] (13.4)	10.46	2.20[ac]	65.1	10 (22)	N/A	82[ac] (108[ac])	Spin coating	ISOS-D-2, 65 °C, T$_{80}$=~400 h	[36]
FTO/SnO$_2$/MAPbI$_3$/spiro-MeOTAD/Au	12.03[da]	5.80	3.38[da]	61.3	6	91	22.4[da]	Spin coating	1 Sun, N$_2$, unencapsulated PSM, MPP, T$_{80}$=515 h	[37]
FTO/c-TiO$_2$/(m-TiO$_2$/m-ZrO$_2$/m-C)/ (5-AVA)$_x$(MA)$_{1-x}$PbI$_3$	10.5[ac]	3.72	19.6	57.6	4	N/A	31[ac]	Screen-printing/ drop-diffusion	Ambient Air, RH 65%, storage, unencapsulated PSM, T$_{95}$=2000 h;	[38]
	10.7[ac]	9.6	17.7	62.9	10	N/A	70[ac]	Screen-printing/ drop-diffusion	White light LED, unencapsulated PSM, MPP, T$_{96}$=72 h	
FTO/c-TiO$_2$/(m-TiO$_2$/m-ZrO$_2$/m-C)/ (5-AVA)$_x$(MA)$_{1-x}$PbI$_3$	10.4[ac]	9.3	2[ac]	56	10	N/A	49[ac]	Screen-printing/ drop-diffusion	1 sun, 25 °C, RH 54%, unencapsulated PSM, MPP, T$_{100}$=1000 h; Outdoor, 30 °C, RH 80%, encapsulated PSM, T$_{100}$=720 h; RH 54%, unencapsulated PSM, storage, T$_{100}$=8760 h	[39]
FTO/c-TiO$_2$/(m-TiO$_2$/m-ZrO$_2$/m-C)/ (5-AVA)$_x$(MA)$_{1-x}$PbI$_3$	11.2[ac]	7.1	2.2[ac]	70.4	8	46.7	46.7[ac]	Screen-printing/ drop-diffusion	1 sun, 55 °C, short circuit, T$_{100}$=10,000 h	[40]

[ac], active area, [ap], aperture area; [da], designated area (active area + dead area for interconnections). [CE], certified efficiency; ITO, indium tin oxide; FTO, fluorine doped tin oxide; c-TiO$_2$, compact TiO$_2$; mp, mesoporous TiO$_2$; spiro-OMeTAD, 2,2',7,7'-tetrakis(N,N-di-4-methoxyphenylamino)-9,9'-spirobifluorene; PCBM, [6,6]-phenyl-C60,61 butyric acid methyl ester; PTAA, poly[bis(4-phenyl)(2,4,6-trimethylphenyl)amine]; PEDOT:PSS, poly(3,4-ethylenedioxythiophene): poly(styrenesulfonate); P3HT, poly(3-hexylthiophene-2,5-diyl) regioregular; 5-AVA, 5-aminovaleric acid. The device performance values are mainly obtained from current-voltage curves.

Figure 1. Summary plots showing the PSM performance parameters A) PCE, B) J$_{sc}$, C) V$_{oc}$, and D) FF as a function as the solar module area for the studies listed in **Table 1**. PCE, V$_{oc}$, and J$_{sc}$ values are normalized according to the active area and the number of interconnected cells. The lines serve as guides for the eye and do not correspond to average or any statistical values.

Note that some reports in **Table 1** also provide the geometric fill factor (GFF) of the solar module, and some PCE values are reported according to the active area, which excludes the area of the interconnections. In a solar module, the GFF is defined as the ratio between the photoactive area and the total area. Solar modules can generate more power with a higher GFF for a given solar module size. To facilitate a comparison of PSMs' performance fabricated by different research groups, it will be more convenient if researchers report the designated area efficiency or aperture area efficiency, including the interconnections regions. Another essential guideline for high efficiency solar modules is to develop suitable interconnection processing techniques.[41–43] Furthermore, each sub-cell and module pattern length also affects the charge transport length across the subcell. A suitable module pattern design is thus crucial for high efficiency PSMs due to the conductivity limit of the transparent conductive oxide based front electrode (e.g., ITO, FTO, etc.).[44]

We also analyzed PSMs stability profiles and plotted the extracted parameters in the literature (**Table 1**) in **Figure 2**. Based on **Figure 2A**, carbon electrode based PSMs seem to show better stability than those with metal based electrodes. Carbon electrode based PSMs take advantages of the thick hydrophobic carbon layer and the excess perovskite filled in the multiple mesoporous layers.[40] However, due to the aging difference in test protocols, this trend requires further verification.[45] On the other hand, metal electrode based PSMs show nearly twice the efficiency of carbon electrode based PSMs (**Figure 2C**). When considering GFF, the metal electrode based PSMs show nearly four times the carbon electrode based PSMs efficiency. Therefore, metal electrode based PSMs currently have an appreciable advantage in PCE and appear more promising for future development of high efficiency PSMs that can compete with commercialized solar modules.[7] Furthermore, the plots of thermal stability of PSMs show that encapsulation is critically important to achieve thermal stability, albeit only in a small number of reports. This observation is consistent with the studies on small-area PSCs.[46-47] For metal electrode based PSMs, it is also clear that formamidinium based perovskite showed relative better stability than the those based on pure methylammonium due to the better stability of formamidinium based perovskite,[6] as discussed in more detail later.

In the following sections, we review the progress on fabrication of high stability PSCs and PSMs created by the engineering of various functional layers: perovskite layers, interface layers including electron and hole transport layers, barrier layers, as well as electrode and encapsulation layers.

## Engineering of the Perovskite Layer for Stability Improvement

In the early stages of PSC research, the most commonly used perovskite composition was $CH_3NH_3PbI_3$ (MAPbI3, **Cat. No. 793833**). However, its poor stability[48] and thermal decomposition[49] rendered $MAPbI_3$ unsuitable for long-term stable operation. To date, formamidinium (FA_+) based mixed cation perovskite materials with improved thermal stability, including MAFA, CsMAFA, CsFA, RbCsFA, RbCsMAFA have been employed to fabricate high-efficiency thermal stable PSCs.[9] Beside FA^+ and MA^+, several other large cation such as butyl ammonium (BA^+, **Cat. No. 910961**), and phenylethylammonium (PEA^+, **Cat. No. 901937**), have also been incorporated into the already mentioned perovskites to improve their intrinsic stability, and overall PSC stability. Besides these, the inorganic perovskite $CsPbX_3$ has also been used as a potential thermal stable candidate. For example, $CsPbI_3$ was used to achieve an efficiency comparable to that of organic-inorganic perovskite based PSCs.[50] In addition to composition engineering, additive engineering[10] and passivation engineering[51-52] have also been used to enhance perovskite stability against external stressors. Research shows the employment of stability improvement strategies to be effective for small-size PSCs. For example, it has been reported that small size PSCs based on the FACs perovskite with additional piperidinium salt passivation can
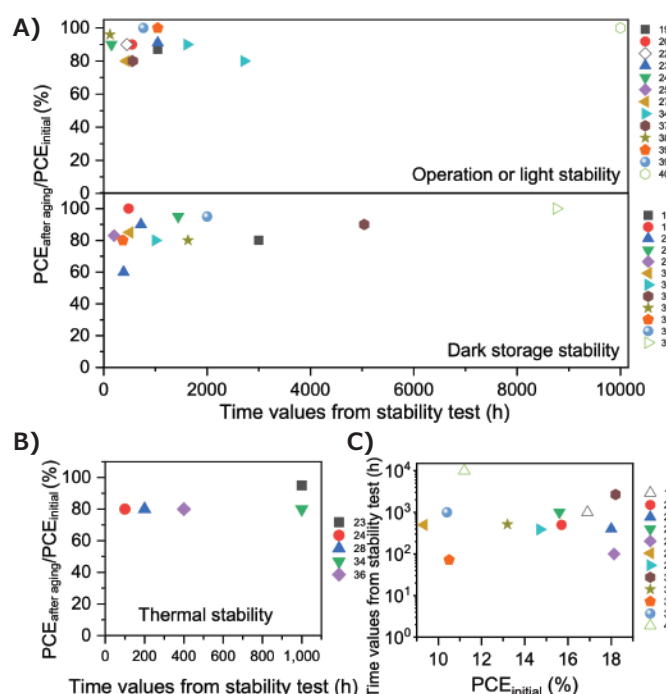
Figure 2. A–C) PSM stability profile analysis by plotting the extracted parameters in the literature (**Table 1**). The ratio a PCE after a certain time aging test versus the initial PCE of PSMs as a function of the reported stability time values of **A**) operational or light stability and **B**) thermal stability, for example, T_{80} represents the time over which the device efficiency reduces to 80% of its initial value. **C**) The estimated operation stability time values obtained from the PSMs' stability test as a function of the initial PCEs.

withstand the high temperature stress of 60 °C and 85 °C during operation under continuous light illumination (**Figure 3**).[53] These promising findings suggest that PSCs show great potential to pass the toughest stability testing against light and heat induced degradation (LeTID). These successful examples can thus serve as stepping stones to inspire researchers to transfer perovskite stability improvement strategies to large-area PSMs.

To date, many scalable perovskite deposition methods, such as doctor blading, slot-die coating, meniscus printing, and vapor deposition, have been used to fabricate large-area perovskite thin films for PSM manufacturing (see **Table 1**). However, most of these reports focused on the deposition of $MAPbI_3$ and $MAPbI_{3-x}Cl_x$ perovskite. Only a few works used scalable methods to deposit FA based perovskites. To drive PSMs to reach the same stability level as PSCs, it is imperative to integrate the accumulated high quality perovskite engineering strategies with scalable methods. For example, bar coating has been used to deposit $(FA_{0.85}MA_{0.15})_{0.95}Pb(I_{0.85}Br_{0.15})_3$ films on 7 cm × 7 cm substrates. Combining perovskite surface modification with hole transport layer engineering, the PSMs reached a PCE of 17.1% with a designated area of 24.97 cm^2. Their corresponding PSCs with an active area of 0.0935 cm^2 gave a T_{95} of 1370 h under continuous 1-Sun illumination at room temperature by tracking their maximum power point.[54]
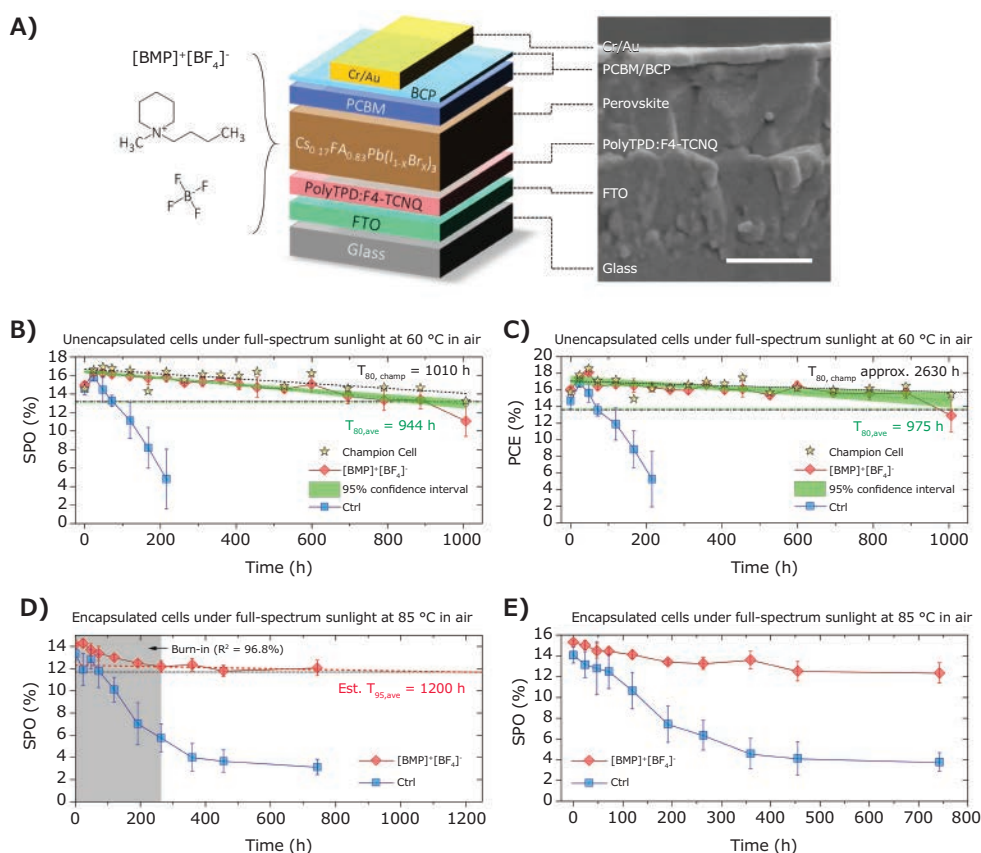
Figure 3. A) Schematic drawing showing the p-i-n PSCs and the chemical structure of $[BMP]^+[BF_4]^-$. BCP, bathocuproine; PCBM, phenyl-C61-butyric acid methyl ester; PolyTPD, poly(4-butylphenyl-diphenylamine); F4-TCNQ, tetrafluoro-7,7,8,8-tetracyanoquinodimethane. **B–E)** Long-term operational stability of PSCs. **B)** Evolution of steady-state power output (SPO) of unencapsulated 0.25 mol % $[BMP]^+[BF_4]^-$-modified and control (Ctrl) $Cs_{0.17}FA_{0.83}Pb(I_{0.77}Br_{0.23})_3$ perovskite solar cells (eight cells for each condition), aged under full-spectrum sunlight at 60 °C in ambient air. **C)** Corresponding PCEs for (A). **D)** Evolution of SPOs of encapsulated 0.25 mol % $[BMP]^+[BF_4]^-$ modified and control $Cs_{0.17}FA_{0.83}Pb(I_{0.77}Br_{0.23})_3$ cells aged under full-spectrum sunlight at 85 °C in ambient air (six cells for each condition). **E)** Corresponding PCEs for (C). In all figures, the error bars denote standard deviations. Reproduced with permission from reference 53, copyright 2020 American Association for the Advancement of Science.

To further enhance the perovskite quality, solvent engineering[4,55] and additive engineering[10] should be considered during the scalable fabrication of PSMs to control the nucleation and grain growth. Due to the different solvation characteristics of FA^+ and Cs^+ compared with MA^+, FA based perovskites usually show noticeably different interactions with solvents;[56] the partial substitution of I^- with Br^- or Cl^- ions used to stabilize the photoactive phase perovskites also makes the FA based perovskite formation more complex than pure $MAPbI_3$.[57-58] Thus, the different interaction of perovskite anions and cations with solvent molecules in the precursor solution and additives should be considered to obtain high-quality, large-area perovskite films. For example, a Lewis base hexamethylphosphoramide (HMPA, **Cat. No. H11602**) has been reported by Nazeeruddin et al., to form the PbI_2–HMPA complex and induce high quality $MAPbI_3$ films via the spin coating method.[59] Recently, Park et al. introduced HMPA into FACs perovskite with the composition of $(FAPbI_3)_{0.875}(CsPbBr_3)_{0.125}$ precursor solution and fabricated large-area perovskite films by D-bar coating (**Figure 4**).[60] It is found that HMPA with a higher donor number versus dimethyl sulfoxide (DMSO) leads to the formation of a stable adduct intermediate phase, which gives a dense and uniform large area perovskite film. Their 5 × 5 cm² PSMs achieved an active area (18.66 cm²) PCE of 17.01%.
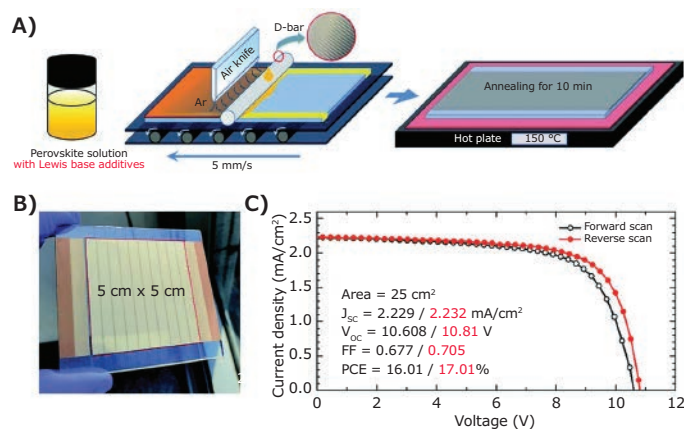
Figure 4. A) Schematic illustration of the bar-coating process for depositing large-area perovskite films. **B)** Photograph of the PSM. **C)** J–V curves for the PSM. Republished with permission from reference 60, copyright 2020 Royal Society of Chemistry.

The higher defect density of the perovskite top surface, especially at the grain boundaries, usually affects device performance and stability considerably when compared with that at the bottom interface.[61] A further surface passivation is important to passivate the surface defects to reduce

non-radiation charge recombination and reduce the defect induced perovskite degradation. Such surface passivation is also employed in PSMs fabrication.[6] However, most surface passivation methods used in PSCs are based on the spin coating method. Further exploration to develop surface passivation for large area perovskite films in PSMs has been reported.[34]

Engineering of the Interface Layers for Stability Improvement

In PSCs and PSMs, each interface layer, including charge transport layers (CTLs), electrode, or barrier layer, also contributes to the whole solar cell device operation. Like the perovskite layer, all the interface layers also need to be coated over a large area with minimal defects for scalable PSM fabrication. Engineering of these interface layers also plays important roles in device stability improvement.

In a typical PSC, the perovskite layer is sandwiched between two CTLs, i.e., electron and hole transport layers (ETL and HTL). Besides their charge transport functions, a compact and stable ETL or HTL also contributes to the long term stability by acting as a UV filter or isolation layer to alleviate the adverse effect of external detrimental factors such as UV light and H_2O/O_2 or reduce the perovskite degradation.

To date, various types of materials[11,62] have been directly deposited on conductive substrates, for use as bottom CTLs such as TiO_2, SnO_2 in n-i-p PSCs, and NiO, PTAA in n-i-p PSCs. These materials are usually compatible with scalable processing methods, such as spray coating,[23] slot-die coating,[31] or sputter deposition,[37] and can be easily coated into uniform large area thin films for module fabrication. For the CTLs deposited on top of the perovskite layer, the compatibility of the deposition methods with the perovskite layer should be considered due to the soft nature of perovskites. For example, during the solution process perovskite films can often be dissolved by strong polar solvents, while perovskite films can easily be damaged by strong beam irradiation or high energy plasma[14] during the vacuum deposition processes. The top CTLs also play a critical role in the perovskite stability as they naturally provide protection for the perovskite layer by shielding perovskite from ingression of metal particles and H_2O/O_2 and keeping volatile components inside.

Among all the top HTLs in high efficiency n-i-p PSCs/PSMs, spiro-OMeTAD (**Cat. No. 792071**) is the most commonly used (**Table 1**). To date, only a few works used scalable coating techniques to deposit spiro-OMeTAD.[63-64] The poor thermal and moisture stability of spiro-OMeTAD also limits device stability.[65] To address these issues, several authors have modified spiro-OMeTAD HTL to improve PSMs stability. Inspired by incorporating P3HT into spiro-OMeTAD to improve small-area PSCs stability against moisture,[66] Qi et al. used a spiro-OMeTAD-P3HT mixed HTL in PSMs. We found that the use of such a mixture HTL protects the underlying layers during the P1-P2-P3 line scribing necessary for PSM fabrication and retards gold migration to improve stability.[34] Replacing spiro-OMeTAD with stable HTL has also been demonstrated to be effective for improving PSM

stability. Noh et al. used pure P3HT without any dopant as a HTL in PSMs.[54] To address the relatively low device performance of P3HT based PSCs in previous reports,[67] they post-treated the $(FA_{0.85}MA_{0.15})_{0.95}Pb(I_{0.85}Br_{0.15})_3$ perovskite surface with n-hexyl trimethyl ammonium bromide to form a 2D perovskite thin layer on top of perovskite. This 2D thin layer effectively passivates charge traps on the perovskite surface and induces improved morphology of P3HT to enable mobility improvement from 10^{-5} cm^2 V^{-1} s^{-1} to 0.1 cm^2 V^{-1} s^{-1}. As a result, their PSMs achieved a PCE of over 16%, and the corresponding PSCs showed good long term stability with T_{95} of 1,370 hours under 1-Sun illumination at room temperature (**Table 1**). Note that their P3HT layer can also be deposited by bar coating. Other top HTLs, such as dopant free organic HTLs and inorganic HTLs, deliver good device performance and stability in small-area PSCs and can be tested in PSM in future studies.

In p-i-n PSCs/PSMs, the most widely used ETLs are fullerene (C_{60}) or derivatives such as PCBM. Because the outward diffusion of perovskite degradation by-products can penetrate the top CTLs and react with the Ag electrode,[68] Han et al. developed a nanostructured carbon layer containing N-doped graphene, the fullerene derivative phenyl-C61-butyric acid methyl ester (PCBM) and carbon quantum dots (CQDs), to act as both the blocking layer and ETL.[69] The Ag electrode reaction with perovskite becomes even worse in the P1-P2-P3 interconnection regions due to the direct contact of the electrode with the perovskite layer.[70] Besides the above-mentioned nanostructured carbon layer based ETL, Han et al. further introduced a low-dimensional diffusion barrier at the interconnection region, their corresponding PSMs with an area of 36 cm^2 achieved PCE of 15.6% and T_{95}=1000 h under 85 °C thermal aging and T_{91}= 1,000 h under AM 1.5 solar light soaking, respectively.[23]

In addition to ETL engineering, introducing an additional barrier layer into the PCS interfaces has been demonstrated to be of equal importance to improve device stability.[14] These barriers can protect the perovskite layer and CTLs from external stressors such as heat, light, and H_2O/O_2 and keep perovskite degradation by-products inside. Also, some delicate barrier designs can simultaneously improve efficiency and stability. Barrier engineering strategies have also been successfully transferred from PSCs to PSMs. For example, Carlo et al. introduced two-dimensional (2D) materials (e.g., graphene and functionalized MoS_2) into n-i-p PSMs.[36] Incorporation of 2D materials at the ETL/perovskite and perovskite/HTL interface has been shown to improve PSM stability and efficiency. The corresponding PSMs achieved an active area PCE of 13.4% (108 cm^2) and 15.3% (82 cm^2), respectively. In addition, the 2D material-based PSMs show a T_{80} lifetime ~400 h under a prolonged (>1000 h) thermal stress test at 65 °C.

In typical PSCs, the deposition of a counter electrode occurs on top of CTLs as the back contact.[15] Similar to CTLs, the electrode can also protect the underlying layers. The most commonly used metal electrodes are Au, Ag, Al, etc. However, these metal materials may diffuse into underlying layers and react with the

outward diffused perovskite degradation by-products. Using inert and stable metal or other low cost materials is desirable for stability improvement and cost reduction. For example, Correa-Baena et al. introduced a Cr layer inserted between spiro-OMeTAD and the Au electrode; the Cr/Au-based PSCs showed markedly improved stability.[71] Huang et al. studied the possibility of using low cost Cu as the electrode for PSCs.[72] In their PSMs, they also used Cu as the counter electrode, and the device showed good module performance and stability.[18,22,73] Chen et al. found that Cu was not stable enough for long-term aging due to its reaction with perovskite, and formed Cu^+ ions, which was detected by X-ray photoelectron spectroscopy (XPS).[74] They further introduced a bismuth (Bi) layer underlying the commonly used Ag layer, the Bi layer electrode with an oriented 2D structure prevented both inward moisture/Ag and outward iodine ions to improve PSC stability. Other metal complex layers, such as Cr_2O_3/Cr,[75] MoOx/Au, MoOx/Ag, and MoOx/Al,[76] also show improved stability. As these layers are compatible with thermal evaporation, one may easily transfer them to the fabrication of PSMs in the future. In addition to metal electrodes, some stable conductive oxide electrodes such as ITO or indium zinc oxide (IZO) have also been used as electrodes in semitransparent PSCs or tandem PSCs.[77-78] These compact oxide layers can act as excellent barriers to damage due to metal diffusion and outside moisture and inside halogen for stable devices. However, proper buffer layers are required to protect the underlying layers when sputtering ITO or IZO as electrodes.

Carbon electrodes consisting of combinations of carbon black, graphite, and additives have delivered excellent stability in PSCs because they restrict the penetration of H_2O/O_2 due to their inert chemical characteristics and over 10 μm thickness.[79] The compatibility of such devices with the screen printing method makes them easily transferrable to the module level. For example, Mathews et al. developed the carbon electrode based PSMs with an active area of 70 cm^2, which showed a PCE of 10.7% and a T_{95} lifetime of 2000 h in ambient air (25 °C, 65% RH).[38] Combining with 2D/3D interface engineering of the perovskite layer, Nazeeruddin et al. fabricated a 10 × 10 cm^2 carbon electrode based PSMs and achieved a PCE of 11.2% and long-term stability with zero PCE loss after 10,000 h light-soaking stability.[40] However, when the carbon based PSMs were further scaled up to an active area of 198 cm^2, the PCE dropped significantly to 6.6% due to the irregular infiltration process of the perovskite film over large scale.[80] The geometrical fill factor of 45.5% is also relatively low due to the difficulty of controlling the dead area loss at the interconnection regions.

Encapsulation

Encapsulation is widely employed to suppress moisture and oxygen penetration into semiconductor devices (e.g., solar cells, light emitting diodes) and improve their long-term stability. The encapsulation capability is usually defined by water vapor transmission rate (WVTR) and oxygen transmission rate (OTR).

Similarly, encapsulation is also an effective strategy to improve PSC stability.[16] For PSCs, encapsulation not only acts as a

robust barrier layer that helps keep the whole device into a closed enclosure by preventing the diffusion of external ambient gases, such as moisture and oxygen, as well as containing the internally generated volatile degradation by-products. Deposition methods based on scalable plasma enhanced chemical vapor deposition (PECVD), chemical vapor deposition (CVD), atomic layer deposition (ALD) are used to form the encapsulation layer on top of the whole device, which has been used in organic light emitting diodes[81] or organic solar cells.[82] The good flexibility of thin films, such as parylene, Al_2O_3, SiN_x, SiO_x, or multiple layers, also makes them suitable for flexible devices. Recently, Qi et al. employed parylene encapsulation via upscalable CVD to encapsulate PSMs.[34] Parylene films helped keep the whole module, including the P2 and P3 patterning lines, in a closed space to improve module stability.

It is also possible to use glues such as polyisobutylene (PIB), ethylene vinyl acetate (EVA), surlyn, polyolefin, butyl rubber to attach a cover glass or metal to the back of the device to serve as the encapsulation structure. For example, McGehee et al. reported that glass–glass encapsulation for PSCs could enable them to pass the industry standard IEC 61646 damp heat and thermal cycling tests.[46] The combination of thin film and cover glass encapsulation can further improve the effectiveness of encapsulation. Recently, Ho-Baillie et al. also reported a low-cost polymer/glass stack encapsulation that enabled PSCs to pass the demanding IEC 61215:2016 damp heat and humidity freeze tests.[47]

Moreover, encapsulation can also prevent the leakage of Pb into the environment when Pb-based PSMs break due to extreme weather conditions during operation. Qi et al. employed epoxy resin encapsulation to protect PSMs and demonstrated that it effectively reduced lead leakage under a hail impact (modified FM 44787 standard) test standard.[83]

Summary and Outlook

In this review, we discuss the strategies for stability improvement of PSCs/PSMs based on aspects of composition engineering of the perovskite layer, charge transport layers, barrier layers, electrode, and encapsulation. Most of these strategies have been tested on small size PSCs or PSMs, and similar strategies have not been widely considered or systematically investigated in the context of PSMs. To achieve the practical application of PSCs, it is important to engineer all the function layers to boost the stability of PSMs because each function layer contributes to the whole device stability. Moreover, the stability improvement strategies should also be compatible with scalable processing methods to enable their employment in PSMs. As shown in **Figure 5**, Qi et al. developed a holistic interface stabilization strategy by modifying all the relevant layers and interfaces, namely the perovskite layer, charge transporting layers and device encapsulation, and boosting stability and efficiency of PSMs. Their work suggests the importance of considering the engineering of all layers and interfaces when upscaling perovskite solar cells.
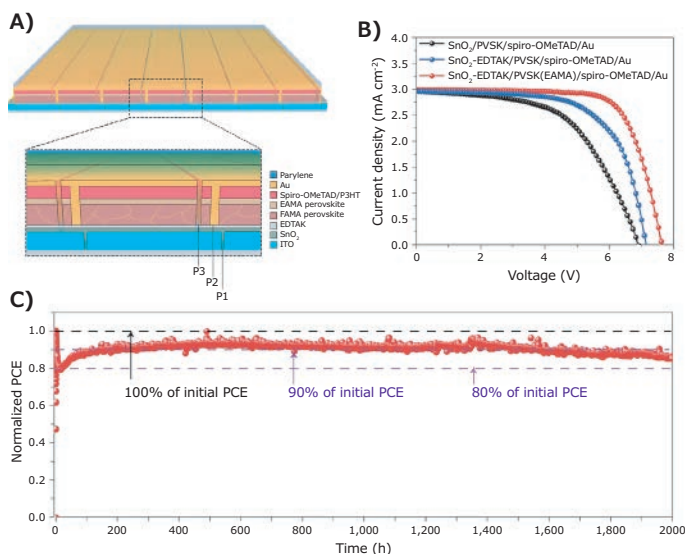
Figure 5. A) The holistic interface stabilization strategy of PSMs. B) The performance of PSMs. C) The operational stability of PSMs with holistic interface stabilization strategy. Reproduced with permission from reference 34, copyright 2020 Springer Nature.

Acknowledgments

References

(1) Kim, J. Y.; Lee, J.-W.; Jung, H. S.; Shin, H.; Park, N.-G. *Chem. Rev.* **2020**, *120* (15), 7867–7918.
(2) Li, Z.; Klein, T. R.; Kim, D. H.; Yang, M.; Berry, J. J.; van Hest, M. F. A. M.; Zhu, K. *Nat. Rev. Mater.* **2018**, *3* (4), 18017.
(3) Qiu, L.; He, S.; Ono, L. K.; Liu, S.; Qi, Y. B. *ACS Energy Lett.* **2019**, *4* (9), 2147–2167.
(4) Park, N.-G.; Zhu, K. *Nat. Rev. Mater.* **2020**, *5* (5), 333–350.
(5) Ono, L. K.; Qi, Y. B.; Liu, S. *Joule* **2018**, *2* (10), 1961–1990.
(6) He, S.; Qiu, L.; Ono, L. K.; Qi, Y. B. *Mater. Sci. Eng. R Rep.* **2020**, *140*, 100545.
(7) Green, M. A.; Dunlop, E. D.; Hohl-Ebinger, J.; Yoshita, M.; Kopidakis, N.; Hao, X. *Prog. Photovolt.* **2020**, 10.1002/pip.3371.
(8) Boyd, C. C.; Cheacharoen, R.; Leijtens, T.; McGehee, M. D. *Chem. Rev.* **2019**, *119* (5), 3418–3451.
(9) Ono, L. K.; Juarez-Perez, E. J.; Qi, Y. B. *ACS Appl. Mater. Interfaces* **2017**, *9* (36), 30197–30246.
(10) Liu, Z.; Ono, L. K.; Qi, Y. B. *J. Energy Chem.* **2020**, *46*, 215–228.
(11) Yang, G.; Tao, H.; Qin, P.; Ke, W.; Fang, G. *J. Mater. Chem. A* **2016**, *4* (11), 3970–3990.
(12) Chen, J.; Park, N.-G. *J. Phys. Chem. C* **2018**, *122* (25), 14039–14063.
(13) Rakstys, K.; Igci, C.; Nazeeruddin, M. K. *Chem. Sci.* **2019**, *10* (28), 6748–6769.
(14) Zhang, S.; Liu, Z.; Zhang, W.; Jiang, Z.; Chen, W.; Chen, R.; Huang, Y.; Yang, Z.; Zhang, Y.; Han, L.; Chen, W. *Adv. Energy Mater.* **2020**, *10* (35), 2001610.
(15) Liu, Z.; He, H., In *Nanostructured Materials for Next-Generation Energy Storage and Conversion: Photovoltaic and Solar Energy*, Atesin, T. A.; Bashir, S.; Liu, J. L., Eds. Springer Berlin Heidelberg: Berlin, Heidelberg, **2019**; pp 165–225.
(16) Corsini, F.; Griffini, G. *J. Phys.: Energy* **2020**, *2* (3), 031002.
(17) Yang, M.; Li, Z.; Reese, M. O.; Reid, O. G.; Kim, D. H.; Siol, S.; Klein, T. R.; Yan, Y.; Berry, J. J.; van Hest, M. F. A. M.; Zhu, K. *Nat. Energy* **2017**, *2* (5), 17038.
(18) Deng, Y.; Zheng, X.; Bai, Y.; Wang, Q.; Zhao, J.; Huang, J. *Nat. Energy* **2018**, *3* (7), 560–566.
(19) Deng, Y.; Van Brackle, C. H.; Dai, X.; Zhao, J.; Chen, B.; Huang, J. J. S. A. *Sci. Adv.* **2019**, *5* (12), eaax7537.
(20) Chen, H.; Ye, F.; Tang, W.; He, J.; Yin, M.; Wang, Y.; Xie, F.; Bi, E.; Yang, X.; Gratzel, M.; Han, L. *Nature* **2017**, *550* (7674), 92–95.
(21) Li, K.; Xiao, J.; Yu, X.; Bu, T.; Li, T.; Deng, X.; Liu, S.; Wang, J.; Ku, Z.; Zhong, J.; Huang, F.; Zhong, Z.; Peng, Y.; Li, W.; Cheng, Y. *ACS Appl. Mater. Interfaces* **2018**, *1* (8), 3565–3570.
(22) Deng, Y.; Ni, Z.; Palmstrom, A. F.; Zhao, J.; Xu, S.; Van Brackle, C. H.; Xiao, X.; Zhu, K.; Huang, J. *Joule* **2020**, *4* (9), 1949–1960.
(23) Bi, E.; Tang, W.; Chen, H.; Wang, Y.; Barbaud, J.; Wu, T.; Kong, W.; Tu, P.; Zhu, H.; Zeng, X.; He, J.; Kan, S.-i.; Yang, X.; Grätzel, M.; Han, L. *Joule* **2019**, *3* (11), 1–13.
(24) Li, J.; Wang, H.; Chin, X. Y.; Dewi, H. A.; Vergeer, K.; Goh, T. W.; Lim, J. W. M.; Lew, J. H.; Loh, K. P.; Soci, C.; Sum, T. C.; Bolink, H. J.; Mathews, N.; Mhaisalkar, S.; Bruno, A. *Joule* **2020**, *4* (5), 1035–1053.
(25) Qiu, L.; He, S.; Jiang, Y.; Son, D.-Y.; Ono, L. K.; Liu, Z.; Kim, T.; Bouloumis, T.; Kazaoui, S.; Qi, Y. B. *J. Mater. Chem. A* **2019**, *7* (12), 6920–6929.
(26) Jiang, Y.; Leyden, M. R.; Qiu, L.; Wang, S.; Ono, L. K.; Wu, Z.; Juarez-Perez, E. J.; Qi, Y. B. *Adv. Funct. Mater.* **2018**, *28* (1), 1703835.
(27) Jiang, Y.; Remeika, M.; Hu, Z.; Juarez-Perez, E. J.; Qiu, L.; Liu, Z.; Kim, T.; Ono, L. K.; Son, D. Y.; Hawash, Z.; Leyden, M. R.; Wu, Z.; Meng, L.; Hu, J.; Qi, Y. B. *Adv. Energy Mater.* **2019**, *9* (13), 1803047.
(28) Luo, L.; Zhang, Y.; Chai, N.; Deng, X.; Zhong, J.; Huang, F.; Peng, Y.; Cheng, Y.-B.; Ku, Z. *J. Mater. Chem. A* **2018**, *6* (42), 21143–21148.
(29) Liu, Z.; Qiu, L.; Juarez-Perez, E. J.; Hawash, Z.; Kim, T.; Jiang, Y.; Wu, Z.; Raga, S. R.; Ono, L. K.; Liu, S. F.; Qi, Y. B. *Nat. Commun.* **2018**, *9* (1), 3880.
(30) Tian, S.; Li, J.; Li, S.; Bu, T.; Mo, Y.; Wang, S.; Li, W.; Huang, F. *Sol. Energy* **2019**, *183*, 386–391.
(31) Bu, T.; Li, J.; Zheng, F.; Chen, W.; Wen, X.; Ku, Z.; Peng, Y.; Zhong, J.; Cheng, Y. B.; Huang, F. *Nat. Commun.* **2018**, *9* (1), 4609.
(32) Jung, E. H.; Jeon, N. J.; Park, E. Y.; Moon, C. S.; Shin, T. J.; Yang, T. Y.; Noh, J. H.; Seo, J. *Nature* **2019** *567* (7749), 511–515.
(33) Ren, A.; Lai, H.; Hao, X.; Tang, Z.; Xu, H.; Yu Jeco, B. M. F.; Watanabe, K.; Wu, L.; Zhang, J.; Sugiyama, M.; Wu, J.; Zhao, D. *Joule* **2020**, *4* (6), 1263–1277.
(34) Liu, Z.; Qiu, L.; Ono, L. K.; He, S.; Hu, Z.; Jiang, M.; Tong, G.; Wu, Z.; Jiang, Y.; Son, D.-Y.; Dang, Y.; Kazaoui, S.; Qi, Y. B. *Nat. Energy* **2020**, *5*, 596–604.
(35) Agresti, A.; Pescetelli, S.; Palma, A. L.; Del Rio Castillo, A. E.; Konios, D.; Kakavelakis, G.; Razza, S.; Cinà, L.; Kymakis, E.; Bonaccorso, F.; Di Carlo, A. *ACS Energy Lett.* **2017**, *2* (1), 279–287.
(36) Agresti, A.; Pescetelli, S.; Palma, A. L.; Martin-Garcia, B.; Najafi, L.; Bellani, S.; Moreels, I.; Prato, M.; Bonaccorso, F.; Di Carlo, A. *ACS Energy Lett.* **2019**, *4* (8), 1862–1871.
(37) Qiu, L.; Liu, Z.; Ono, L. K.; Jiang, Y.; Son, D.-Y.; Hawash, Z.; He, S.; Qi, Y. B. *Adv. Funct. Mater.* **2018**, *29* (47), 1806779.
(38) Priyadarshi, A.; Haur, L. J.; Murray, P.; Fu, D.; Kulkarni, S.; Xing, G.; Sum, T. C.; Mathews, N.; Mhaisalkar, S. G. *Energy Environ. Sci.* **2016**, *9* (12), 3687–3692.
(39) Hu, Y.; Si, S.; Mei, A.; Rong, Y.; Liu, H.; Li, X.; Han, H. *Sol. RRL* **2017**, *1* (2), 1600019.
(40) Grancini, G.; Roldán-Carmona, C.; Zimmermann, I.; Mosconi, E.; Lee, X.; Martineau, D.; Narbey, S.; Oswald, F.; De Angelis, F.; Graetzel, M.; Nazeeruddin, M. K. *Nat. Commun.* **2017**, *8*, 15684.
(41) Palma, A. L.; Matteocci, F.; Agresti, A.; Pescetelli, S.; Calabrò, E.; Vesce, L.; Christiansen, S.; Schmidt, M.; Carlo, A. D., *IEEE J. Photovolt.* **2017**, *7* (6), 1674–1680.
(42) Rakocevic, L.; Gehlhaar, R.; Merckx, T.; Qiu, W.; Paetzold, U. W.; Fledderus, H.; Poortmans, J. *IEEE J. Photovolt.* **2017**, *7* (1), 404–408.
(43) Moon, S.; Yum, J.; Löfgren, L.; Walter, A.; Sansonnens, L.; Benkhaira, M.; Nicolay, S.; Bailat, J.; Ballif, C. *IEEE J. Photovolt.* **2015**, *5* (4), 1087–1092.
(44) Gao, L.; Chen, L.; Huang, S.; Li, X.; Yang, G. *ACS Appl. Energy Mater.* **2019**, *2* (5), 3851–3859.
(45) Khenkin, M. V.; Katz, E. A.; Abate, A.; Bardizza, G.; Berry, J. J.; Brabec, C.; Brunetti, F.; Bulović, V.; Burlingame, Q.; Di Carlo, A.; Cheacharoen, R.; Cheng, Y.-B.; et.al *Nat. Energy* **2020**, *5* (1), 35–49.
(46) Cheacharoen, R.; Boyd, C. C.; Burkhard, G. F.; Leijtens, T.; Raiford, J. A.; Bush, K. A.; Bent, S. F.; McGehee, M. D., E. *Sustain. Energy Fuels* **2018**, *2* (11), 2398–2406.
(47) Shi, L.; Bucknall, M. P.; Young, T. L.; Zhang, M.; Hu, L.; Bing, J.; Lee, D. S.; Kim, J.; Wu, T.; Takamure, N.; McKenzie, D. R.; Huang, S.; Green, M. A.; Ho-Baillie, A. W. Y. *Science* **2020**, *368* (6497), eaba2412.
(48) Conings, B.; Drijkoningen, J.; Gauquelin, N.; Babayigit, A.; D'Haen, J.; D'Olieslaeger, L.; Ethirajan, A.; Verbeeck, J.; Manca, J.; Mosconi, E.; Angelis, F. D.; Boyen, H.-G. *Adv. Energy Mater.* **2015**, *5* (15), 1500477.
(49) Juarez-Perez, E. J.; Hawash, Z.; Raga, S. R.; Ono, L. K.; Qi, Y. B. *Energy Environ. Sci.* **2016**, *9* (11), 3406–3410.
(50) Wang, Y.; Dar, M. I.; Ono, L. K.; Zhang, T.; Kan, M.; Li, Y.; Zhang, L.; Wang, X.; Yang, Y.; Gao, X.; Qi, Y. B.; Grätzel, M.; Zhao, Y. *Science* **2019**, *365* (6453), 591–595.
(51) Ono, L. K.; Liu, S.; Qi, Y. B. *Angew. Chem. Int. Ed.* **2019**, *59* (17), 6676–6698.

(52) Chen, B.; Rudd, P. N.; Yang, S.; Yuan, Y.; Huang, J. *Chem. Soc. Rev.* **2019**, *48* (14), 3842–3867.

(53) Lin, Y.-H.; Sakai, N.; Da, P.; Wu, J.; Sansom, H. C.; Ramadan, A. J.; Mahesh, S.; Liu, J.; Oliver, R. D. J.; Lim, J.; Aspitarte, L.; Sharma, K.; et.al *Science* **2020**, *369* (6499), 96–102.

(54) Jung, E. H.; Jeon, N. J.; Park, E. Y.; Moon, C. S.; Shin, T. J.; Yang, T.-Y.; Noh, J. H.; Seo, J. *Nature* **2019**, *567* (7749), 511–515.

(55) Lee, J.-W.; Lee, D.-K.; Jeong, D.-N.; Park, N.-G. *Adv. Funct. Mater.* **2018**, *29* (47), 1807047.

(56) Lee, J. W.; Dai, Z.; Lee, C.; Lee, H. M.; Han, T. H.; De Marco, N.; Lin, O.; Choi, C. S.; Dunn, B.; Koh, J.; Di Carlo, D.; Ko, J. H.; Maynard, H. D.; Yang, Y. *J. Am. Chem. Soc.* **2018**, *140* (20), 6317–6324.

(57) Xu, J.; Boyd, C. C.; Zhengshan, J. Y.; Palmstrom, A. F.; Witter, D. J.; Larson, B. W.; France, R. M.; Werner, J.; Harvey, S. P.; Wolf, E. J. J. S. *Science* **2020**, *367* (6482), 1097–1104.

(58) Park, N. J. C. *Cryst. Eng. Comm.* **2016**, *18* (32), 5977–5985.

(59) Zhang, Y.; Gao, P.; Oveisi, E.; Lee, Y.; Jeangros, Q.; Grancini, G.; Paek, S.; Feng, Y.; Nazeeruddin, M. K. *J. Am. Chem. Soc.* **2016**, *138* (43), 14380–14387.

(60) Lim, K.-S.; Lee, D.-K.; Lee, J.-W.; Park, N.-G. *J. Mater. Chem. A* **2020**, *8* (18), 9345–9354.

(61) Yang, S.; Chen, S.; Mosconi, E.; Fang, Y.; Xiao, X.; Wang, C.; Zhou, Y.; Yu, Z.; Zhao, J.; Gao, Y.; De Angelis, F.; Huang, J. *Science* **2019**, *365* (6452), 473–478.

(62) Calió, L.; Kazim, S.; Grätzel, M.; Ahmad, S. *Angew. Chem. Int. Ed.* **2016**, *55* (47), 14522–14545.

(63). Di Giacomo, F.; Shanmugam, S.; Fledderus, H.; Bruijnaers, B. J.; Verhees, W. J. H.; Dorenkamper, M. S.; Veenstra, S. C.; Qiu, W.; Gehlhaar, R.; Merckx, T.; Aernouts, T.; Andriessen, R.; Galagan, Y. *Sol. Energy Mater Sol. Cells* **2018**, *181*, 53–59.

(64) Qin, T.; Huang, W.; Kim, J.-E.; Vak, D.; Forsyth, C.; McNeill, C. R.; Cheng, Y.-B. *Nano Energy* **2017**, *31*, 210–217.

(65) Hawash, Z.; Ono, L. K.; Qi, Y. B. *Adv. Mater. Interfaces* **2018**, *5* (1), 1700623.

(66) Kim, G.-W.; Kang, G.; Malekshahi Byranvand, M.; Lee, G.-Y.; Park, T. *ACS Appl. Mater. Interfaces* **2017**, *9* (33), 27720–27726.

(67) Nia, N. Y.; Matteocci, F.; Cina, L.; Di Carlo, A. *Chem. Sus. Chem.* **2017**, *10* (19), 3854–3860.

(68) Kato, Y.; Ono, L. K.; Lee, M. V.; Wang, S.; Raga, S. R.; Qi, Y. B. *Adv. Mater. Interfaces* **2015**, *2* (13), 1500195.

(69) Bi, E.; Chen, H.; Xie, F.; Wu, Y.; Chen, W.; Su, Y.; Islam, A.; Grätzel, M.; Yang, X.; Han, L. *Nat. Commun.* **2017**, *8*, 15330.

(70) Werner, J.; Wolf, E. J.; Boyd, C. C.; van Hest, M. F. A. M.; Luther, J. M.; Zhu, K.; Berry, J. J.; McGehee, M. D. *Energy Environ. Sci.* **2020**, *13* (10), 3393–3403.

(71) Domanski, K.; Correa-Baena, J.-P.; Mine, N.; Nazeeruddin, M. K.; Abate, A.; Saliba, M.; Tress, W.; Hagfeldt, A.; Grätzel, M. *ACS Nano* **2016**, *10* (6), 6306–6314.

(72) Zhao, J.; Zheng, X.; Deng, Y.; Li, T.; Shao, Y.; Gruverman, A.; Shield, J.; Huang, J. *Energy Environ. Sci.* **2016**, *9* (12), 3650–3656.

(73) Deng, Y.; Van Brackle, C. H.; Dai, X.; Zhao, J.; Chen, B.; Huang, J. *Sci. Adv.* **2019**, *5* (12), eaax7537.

(74) Wu, S.; Chen, R.; Zhang, S.; Babu, B. H.; Yue, Y.; Zhu, H.; Yang, Z.; Chen, C.; Chen, W.; Huang, Y.; Fang, S.; Liu, T.; Han, L.; Chen, W. *Nat. Commun.* **2019**, *10* (1), 1161.

(75) Kaltenbrunner, M.; Adam, G.; Glowacki, E. D.; Drack, M.; Schwodiauer, R.; Leonat, L.; Apaydin, D. H.; Groiss, H.; Scharber, M. C.; White, M. S.; Sariciftci, N. S.; Bauer, S. *Nat. Mater.* **2015**, *14* (10), 1032–1039.

(76) Sanehira, E. M.; Tremolet de Villers, B. J.; Schulz, P.; Reese, M. O.; Ferrere, S.; Zhu, K.; Lin, L. Y.; Berry, J. J.; Luther, J. M. *ACS Energy Lett.* **2016**, *1* (1), 38–45.

(77) Bush, K. A.; Bailie, C. D.; Chen, Y.; Bowring, A. R.; Wang, W.; Ma, W.; Leijtens, T.; Moghadam, F.; McGehee, M. D. *Adv. Mater.* **2016**, *28* (20), 3937–3943.

(78) Bush, K. A.; Manzoor, S.; Frohna, K.; Yu, Z. J.; Raiford, J. A.; Palmstrom, A. F.; Wang, H.-P.; Prasanna, R.; Bent, S. F.; Holman, Z. C.; McGehee, M. D. *ACS Energy Lett.* **2018**, *3*, 2173–2180.

(79) Mei, A.; Li, X.; Liu, L.; Ku, Z.; Liu, T.; Rong, Y.; Xu, M.; Hu, M.; Chen, J.; Yang, Y.; Grätzel, M.; Han, H. *Science* **2014**, *345* (6194), 295–298.

(80) De Rossi, F.; Baker, J. A.; Beynon, D.; Hooper, K. E. A.; Meroni, S. M. P.; Williams, D.; Wei, Z.; Yasin, A.; Charbonneau, C.; Jewell, E. H.; Watson, T. M. *Adv. Mater. Technol.* **2018**, *3* (11), 1800156.

(81) Park, J.-S.; Chae, H.; Chung, H. K.; Lee, S. I. *Semicond. Sci. Technol.* **2011**, *26* (3), 034001.

(82) Ahmad, J.; Bazaka, K.; Anderson, L. J.; White, R. D.; Jacob, M. V. *Renew. Sust. Energ. Rev.* **2013**, *27*, 104–117.

(83) Jiang, Y.; Qiu, L.; Juarez-Perez, E. J.; Ono, L. K.; Hu, Z.; Liu, Z.; Wu, Z.; Meng, L.; Wang, Q.; Qi, Y. *Nat. Energy* **2019**, *4* (7), 585–593.

Perovskite QDs

Name	Form	Description	Fluorescence Emission, λ_{em} (nm)	Cat. No.
Perovskite quantum dots	10 mg/mL in toluene	oleic acid and oleylamine coated	480	**900747-5ML**
	10 mg/mL in toluene	oleic acid and oleylamine coated	450	**900748-5ML**
	10 mg/mL in toluene	oleic acid and oleylamine coated	530	**905062-5ML**
	10 mg/mL in toluene	oleic acid and oleylamine coated	510	**900746-5ML**

Precursors for Organometallic Perovskites

Organohalide Materials

Name	Composition	Form	Purity	Cat. No.
Methylammonium iodide	$CH_3NH_2 \cdot HI$; CH_6IN	powder	98%	**793493-5G**
Methylammonium triiodoplumbate(II) precursor solution	$[CH_3NH_3]^+[PbI_3]^-$	40 wt. % in DMF	-	**793833-5ML**
Methylammonium bromide	$CH_3NH_2 \cdot HBr$	powder	98%	**793507-5G**
Methylammonium chlorodiiodoplumbate(II) precursor solution	CH_6NClI_2Pb	liquid	-	**809039-25G**
Methylammonium bromide	CH_6BrN	powder	98%	**806498-25G**
n-Propylammonium iodide	$C_3H_{10}IN$	powder	-	**805858-5G** **805858-25G**
Dimethylammonium iodide	C_2H_8IN	powder	98%	**805831-5G** **805831-25G**
i-Propylammonium iodide	$C_3H_{10}IN$	powder	98%	**805882-5G** **805882-25G**
n-Butylammonium iodide	$C_4H_{12}IN$	powder	98%	**805874-5G** **805874-25G**
i-Butylammonium iodide	$C_4H_{12}IN$	powder	98%	**805866-5G** **805866-25G**
t-Butylammonium iodide	$C_4H_{12}IN$	powder	98%	**806102-5G** **806102-25G**

Name	Composition	Form	Purity	Cat. No.
Diethylammonium iodide	$C_4H_{12}IN$	powder	98%	806188-5G 806188-25G
Benzylammonium iodide	$C_7H_{10}IN$	powder	98%	806196-5G 806196-25G
Phenethylammonium iodide	$C_8H_{12}IN$	powder	98%	805904-25G
Phenylammonium iodide	C_6H_8IN	powder	≥98%, H-NMR	805912-5G 805912-25G
Guanidinium iodide	CH_6IN_3	powder	≥99%	806056-5G 806056-25G
Formamidinium iodide	CH_5IN_2	powder	≥98%, H-NMR	806048-5G 806048-25G
Acetamidinium iodide	$C_2H_7IN_2$	powder	98%	805971-5G 805971-25G
Imidazolium iodide	$C_3H_5IN_2$	powder	98%	805963-25G
Methylammonium iodide	$CH_3NH_2 \cdot HI$	powder	-	806390-25G
i-Propylammonium bromide	$C_3H_{10}BrN$	powder or crystals	≥98%	900816-10G 900816-25G
Methylammonium bromide solution	$CH3NH2 \cdot HBr$	0.18 M in 2-propanol	-	808407-50ML
Formamidinium bromide	CH_5BrN_2	powder or crystals	≥98%	900835-5G 900835-25G
Guanidinium bromide	CH_6BrN_3	powder or crystals	≥98%	900839-10G 900839-25G
Diethylammonium bromide	$(C_2H_5)_2NH \cdot HBr$	powder or crystals	≥98%	900840-10G 900840-25G
Propane-1,3-diammonium bromide	$C_3H_{12}Br_2N_2$	powder or crystals	≥98%	900834-5G 900834-25G
Ethane-1,2-diammonium iodide	$C_2H_8N_2 \cdot 2HI$	powder or crystals	≥98%	900852-5G 900852-25G
i-Butylammonium bromide	$C_4H_{12}BrN$	powder or crystals	-	900869-10G 900869-25G
Phenylammonium bromide	C_6H_8BrN	powder or crystals	≥98%	900828-10G 900828-25G
n-Butylammonium bromide	$C_4H_{12}BrN$	powder or crystals	≥98%	900817-10G 900817-25G
Imidazolium bromide	$C_3H_4N_2 \cdot HBr$	powder	≥98%	900821-5G 900821-25G
Benzylammonium bromide	$C_7H_{10}BrN$	powder or crystals	≥98%	900885-5G 900885-25G
Dimethylammonium bromide	C_2H_8BrN	powder	≥98%	900872-10G 900872-25G
t-Butylammonium bromide	$C_4H_{12}BrN$	powder or crystals	≥98%	900827-10G 900827-25G
n-Propylammonium bromide	$C_3H_{10}BrN$	powder or flakes	≥98%	900819-10G 900819-25G
Phenethylammonium bromide	$C_8H_{12}BrN$	powder or crystals	≥98%	900829-10G 900829-25G
Ethane-1,2-diammonium bromide	$C_2H_{10}Br_2N_2$	powder	≥98%	900833-5G 900833-25G
Propane-1,3-diammonium iodide	$C_3H_{12}I_2N_2$	powder	≥98%	900832-5G 900832-25G
Methylammonium iodide	CH_6IN	crystals	≥99%	901434-10G
Methylammonium bromide	CH_6BrN	powder	≥99%	901435-10G
Formamidinium iodide	CH_5IN_2	powder	≥99%	901436-10G
Formamidinium bromide	CH_5BrN_2	powder or crystals	≥99%	901437-10G
Guanidinium iodide	CH_6IN_3	powder	≥99%	901450-10G
Guanidinium bromide	CH_6BrN_3	powder	≥99%	901452-10G
Bis[4-(glycidyloxy)phenyl] methane	$C_{19}H_{20}O_4$	-	>88%	900198-100ML

Lead Halides

Name	Composition	Form	Purity	Cat. No.
Lead(II) chloride	$PbCl_2$	powder and chunks	99.999% trace metals basis	203572-10G 203572-50G
Lead(II) iodide	PbI_2	solid	99.999% trace metals basis	203602-50G
Lead(II) bromide	$PbBr_2$	powder	≥98%	211141-100G 211141-500G
Lead(II) iodide	PbI_2	powder	99%	211168-50G
Lead(II) chloride	$PbCl_2$	powder	98%	268690-5G 268690-250G 268690-1KG

Name	Composition	Form	Purity	Cat. No.
Lead(II) bromide	$PbBr_2$	powder	99.999% trace metals basis	**398853-5G**
Lead(II) chloride	$PbCl_2$	-	99.999%	**449865-5G**
Lead(II) iodide	PbI_2	-	99.999% trace metals basis	**554359-5G**
Lead(II) iodide solution	PbI_2	solution; 0.55 M in DMF	-	**795550-10ML**

Coated Glass Substrates and Electrode Materials

FTO Coated

Name	Surface Resistivity (Ω/sq)	L × W × Thickness (mm)	Cat. No.
Fluorine doped tin oxide coated glass slide	~7	50 × 50 × 2.2	**735140-5EA**
	~7	100 × 100 × 2.3	**735159-5EA**
	~7	300 × 300 × 2.2	**735167-1EA**
	~8	50 × 50 × 3	**735175-5EA**
	~8	100 × 100 × 3	**735183-5EA**
	~8	300 × 300 × 3.2	**735191-1EA**

ITO Coated

Name	Surface Resistivity (Ω/sq)	L × W × Thickness (mm)	Cat. No.
Indium tin oxide coated glass slide, rectangular	15-25	75 × 25 × 1.1	**636916-10PAK** **636916-25PAK**
Indium tin oxide coated boro-aluminosilicate glass slide	5-15	75 × 25 × 1.1	**576360-10PAK** **576360-25PAK**
Indium tin oxide coated glass slide, rectangular	8-12	75 × 25 × 1.1	**578274-10PAK** **578274-25PAK**
Indium tin oxide coated glass slide, square	8-12	25 × 25 × 1.1	**703192-10PAK**
	30-60	25 × 25 × 1.1	**703184-10PAK**

R&D Highlight

Merck

Silicon Anode Materials

High Capacity

For high-capacity cathode research, you need an anode that can keep up. With a capacity over 1300 mAh/g, our silicon composite formulation is well suited for use as a counter electrode for new high capacity cathode materials.[1]

Extended Cycle-Life

Test your batteries longer with our silicon composite anodes. Unlike some silicon-based electrode formulations, our 3D porous conductive polymer prevents capacity loss during the charge/discharge cycles.[1,2]
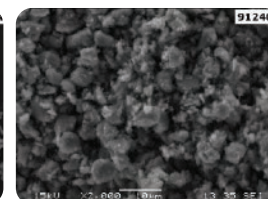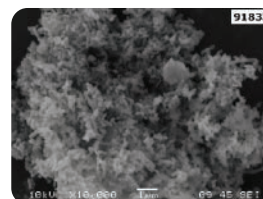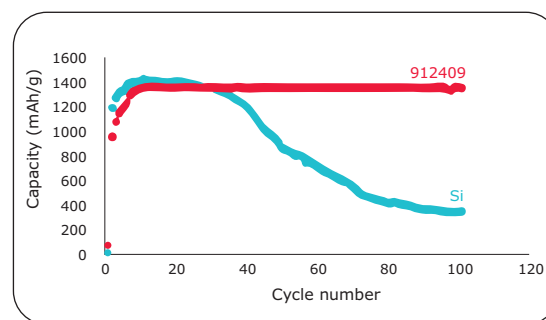
Formula		Cat. No.
High-performance silicon anode material	1 micron (Si)	910961
	100 nm (Si)	910953

References:

1) Wu, H.; Yu, G. H.; Pan, L. J.; Liu, N.; McDowell, M. T.; Bao, Z. N.; Cui, Y. *Nat. Commun.* **2013,** *4,* 1943. DOI: 10.1038/ncomms2941

2) Zhao, F.; Bae, J. W.; Zhou, X. Y.; Guo, Y. H.; Yu, G. H. *Adv. Mater.* **2018,** *30,* 1801796. DOI: 10.1002/adma.201801796

Merck

2D Layered Perovskites

Solution Processable Materials

The recent discovery that single-layer 2D perovskites can be prepared using solution processing techniques[1] has been followed by enormous research into optoelectronic applications of 2D perovskites including light emitting diodes (LEDs),[2] phototransistors,[3] and solar cells,[4] and lasers.[5]

Direct and Tunable Bandgap

Photoluminescent 2D perovskites have a direct bandgap with a narrow emission peak that changes depending on the layer thickness and the choice of amine and halide. We offer an excellent portfolio of the most popular 2D perovskite compositions for photoluminescence based devices.

Improved Moisture Stability

Solar cells fabricated with 2D perovskites have improved stability in moist air compared to 3D perovskites.[4]

| Formula | Cat. No. | Layer Thickness | $(RNH_3)_2(MeNH_3)_{n-1}Pb_nX_{3n+1}$ | | |
			R	X	n
$(BA)_2PbI_4$	**910961**	n=1	Bu	I	1
$(BA)_2PbBr_4$	**910953**	n=1	Bu	Br	1
$(PEA)_2PbI_4$	**910937**	n=1	PE	I	1
$(PEA)_2PbBr_4$	**910945**	n=1	PE	Br	1
$(BA)_2(MA)Pb_2I_7$	**912816**	n=2	Bu	I	2
$(BA)_2(MA)_2Pb_3I_{10}$	**912557**	n=3	Bu	I	3
$(BA)_2(MA)_3Pb_4I_{13}$	**914363**	n=4	Bu	I	4
$(BA)_2(MA)_4Pb_5I_{16}$	**912301**	n=5	Bu	I	5

BA = n-butylammonium; PEA = 2-phenylethylammonium;
MA =methylammonium, Bu=n-butyl, PE=2-phenylethyl

SigmaAldrich.com/perovskite

References:

1) Dou, L.; Wong, A. B.; Yu, Y.; Lai, M.; Kornienko, N.; Eaton, S. W.; Fu, A.; Bischak, C. G.; Ma, J.; Ding, T.; Ginsberg, N. S.; Wang, L-W.; Alivisatos, A. P.; Yang, P. *Science* **2015,** *349,* 1518. DOI: 10.1126/science.aac7660

2) Yuan, M.; Quan, L. N.; Comin, R.; Walters, G.; Sabatini, R.; Voznyy, O.; Hoogland, S.; Zhao, Y.; Beauregard,E. M.; Kanjanaboos, P.; Lu, Z.; Kim, D. H.; Sargent, E. H. *Nat. Nanotechnol.* **2016,** *11,* 872. DOI: 10.1038/NNANO.2016.110

3) Shao, Y.; Liu, Y.; Chen, X.; Chen, C.; Sarpkaya, I.; Chen, Z.; Fang, Y.; Kong, J.; Watanabe, K.;Taniguchi, T.; Taylor, A.; Huang, J.; Xia, F. *Nano Lett.* **2017,** *17,* 7330. DOI: 10.1021/acs.nanolett.7b02980

4) Cao, D. H.; Stoumpos, C. C.; Farha, O. K.; Hupp, J. T.; Kanatzidis, M. G. *J. Am. Chem.* Soc. **2015,** *137,* 7843. DOI: 10.1021/jacs.5b03796

5) Raghavan, C. M.; Chen, T.-P.; Li, S.-S.; Chen, W.-L.; Lo, C.-Y.; Liao, Y.-M.; Haider, G.; Lin, C.-C.; Chen, C.-C.; Sankar, R.; Chang, Y.-M.; Chou, F.-C.; Chen, C.-W. *Nano Lett.* **2018,** *18* (5), 3221. DOI: 10.1021/acs.nanolett.8b00990

Cold Gas-Dynamic Spray Processing as a Versatile Inorganic Material Deposition, Additive Manufacturing and Consolidation Technology
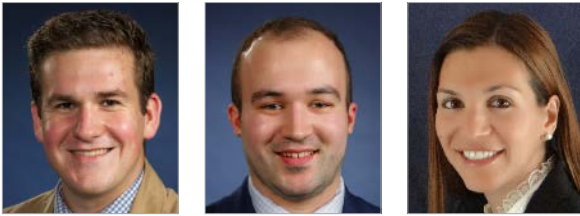
Bryer C. Sousa,* Jack A. Grubbs, and Danielle L. Cote, Ph.D.

Materials and Manufacturing Engineering Program, Department of Mechanical Engineering,
Worcester Polytechnic Institute, Worcester, MA, United States
* Email: bcsousa@wpi.edu, dlcote2.edu

Introduction

In recent years, additive manufacturing (AM) has become much more common in the material processing world due to the accelerated development of early rapid prototyping applications.[1] Automation of AM processes has allowed researchers and industrial manufacturers to increase the throughput of these processes and enable the expeditious creation of geometrically complex parts that were previously not possible to manufacture. Many AM processes utilize a layer-by-layer approach to consolidate feedstock material into a bulk part, which varies significantly from traditional subtractive manufacturing approaches.[2] Unique properties and functionalities are commonly observed in AM-processed materials/parts/components due to the diverse set of available material types — including metals, ceramics, polymers, composites, and novel methods of feedstock material consolidation. Although AM processes can fabricate parts with excellent chemical and mechanical integrity, they are by no means optimized and contain processing faults/defects that need to be mitigated. For example, lack of layer fusion, extensive porosity, and variable residual stress states/distributions can be found in parts manufactured by laser-based AM, which can have ramifications with respect to the resultant mechanical behavior.[3,4] Accordingly, new processing methods are required to avoid these commonly observed defects. Fortunately, the materials consolidation process, commonly known as cold spray, can address such a need for alternative AM methods, as

was recently discussed in a book edited by Pathak and Saha and titled *Cold Spray in the Realm of Additive Manufacturing* as part of Springer's "Materials Forming, Machining and Tribology" series.

On Cold Gas-Dynamic Spray Materials Consolidation

Cold gas-dynamic spray, or simply cold spray, is a promising AM process that, while not new, has seen its most prominent development in recent years given cold spray's applicability within many industrial sectors/applications. Cold spray processing dates back to the 1980's, where researchers at the Institute of Theoretical and Applied Mechanics of the Siberian Division of the Russian Academy of Science incidentally observed the phenomenon of high-speed microparticle deposition at low temperatures during wind tunnel experiments.[5,6] Accordingly, the cold spray process as we know it is a product of this accidental discovery. Nevertheless, cold spray is a solid-state deposition technique that utilizes powder feedstock to create a consolidated part via supersonic particulate impact processing. As depicted in **Figure 1A**, a pressured gas stream, usually nitrogen or helium at moderate temperatures, is used to carry the powder through a de Laval (converging-diverging) nozzle, thus accelerating the particles to said supersonic velocities, therefore enabling deposition onto a substrate material.[7,8] Powders of many material
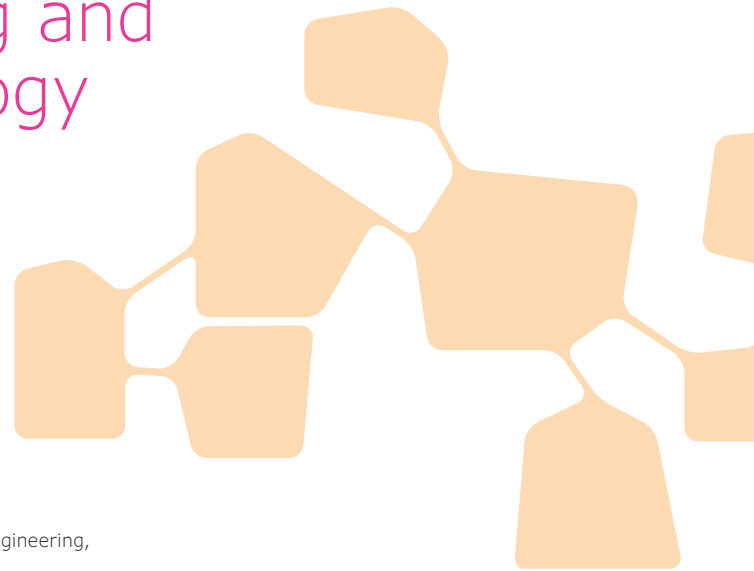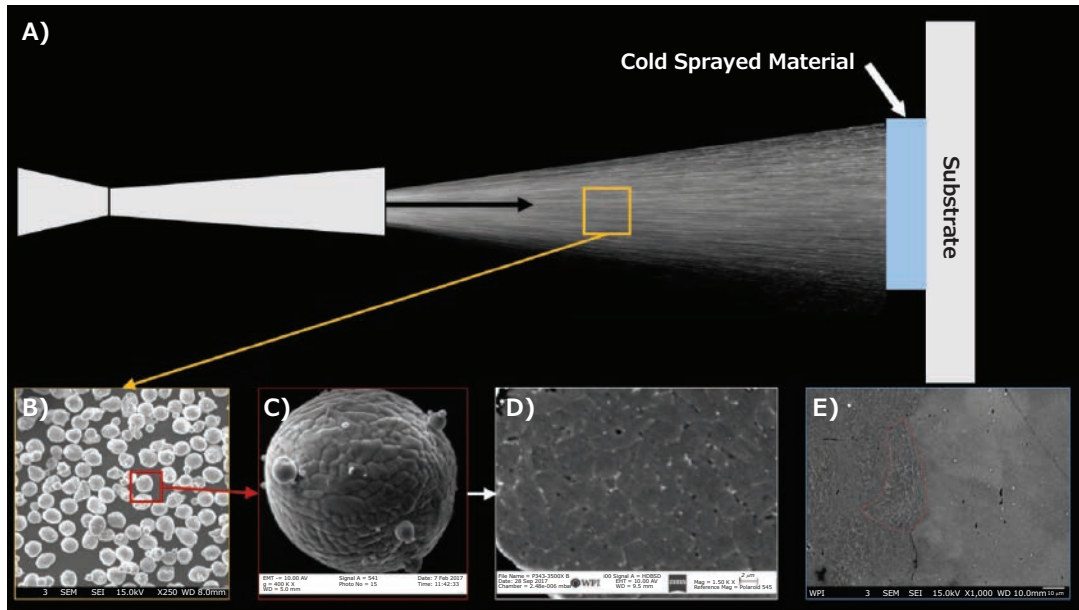
Figure 1. Cold spray process depiction is presented herein with respect to the use of gas-atomized Al 6061 feedstock. **A)** presents a schematic overview of the cold spray process. **B)** presents a scanning electron microscopy (SEM) micrograph of the gas-atomized powder. **C)** presents a SEM micrograph of the surface of a single Al 6061 particle. **D)** presents a SEM micrograph of the internal microstructure of a single particle following cross-sectional preparation. **E)** presents a SEM micrograph that captures the interfacial microstructure between the cold spray deposits particle-substrate system.

types have been used for cold spray processing, leading to vast applications in several industries. Research shows powder properties correlate directly with deposited material behavior and suitability for cold spray processing. Thus, it is critical to understand particle size and morphology (**Figures 1B** and **1C**) and how the particle microstructure (**Figure 1D**) influences the microstructure of deposits (**Figure 1E**).[9,10]

In any case, to achieve consistent deposition during cold spray processing, particles must reach a critical velocity upon impacting a substrate and/or a previously deposited layer. Below this velocity, the particles erode the substrate material and will not form a densified deposit; however, at or just above this critical impact velocity, particles deform at high strain rates and subsequently form particle-substrate and particle-particle bonds to create a deposit or consolidation.[11] Given the importance of particulate critical impact velocity on deposition success, a significant amount of cold spray research focuses on manipulating powder characteristics, processing parameters, and substrate properties to obtain necessary impact conditions for proper particle adhesion and bonding between one substrate and/or previously deposited layers.[12–17] With the aforementioned in mind, a list of significant parameters in the cold spray process, though not comprehensive, is detailed in **Table 1**, in order to ensure that readers interested in incorporating cold spray processing into their technological repertoire can more readily appreciate the varied parametric aspects of the deposition technology.

That being said, cold spray is particularly innovative in how it varies from traditional thermal spray processes. Conventional thermal spray techniques entail partial or complete particle melting, resulting in nonequilibrium microstructures from rapid

Table 1. Significant parameters in the cold spray process that affect deposition success.

Powder Parameters	Carrier Gas Parameters	Nozzle Parameters	Substrate Parameters
Mean Particle Size	Gas Type	Nozzle Material	Substrate Composition
Particle Size Distribution	Gas Pressure	Spray Angle	Substrate Temperature
Particle Morphology	Gas Temperature	Standoff Distance	Substrate Roughness
Powder Composition		Traverse Speed	
Powder Feed Rate		Scanning Step	
		Spray Path	

solidification. Conversely, cold spray is entirely in the solid-state where there is no liquid-solid transition, thus maintaining a refined and dynamically recrystallized variation of the original powder particulates microstructure in the consolidated specimen. This disparity in a particles internal phase change has ramifications on part performance, making cold spray processing more advantageous than thermal spray in certain situations. For example, during numerable thermal spray processes, oxide formation and other phase transformations can occur during solidification following deposition, therefore negatively affecting properties such as electrical conductivity.[18] Additionally, the relatively low processing temperatures associated with cold spray consolidation means that resultant thermal stresses in both the deposit and the substrate are minimized.[19] Hence, the benefits underpinning cold spray processing has led to its adoption in highly varied industries from the biomedical to energy and aerospace applications. As such, said adoptions of cold spray processing are discussed next.

Antipathogenic Cold Gas-Dynamic Spray Consolidations

In an original and experimental undertaking, Champagne et al. assessed the antibacterial functionality of three different copper coated surfaces, which were produced by way of different thermal spray processing techniques.[20] In doing so, Champagne et al. employed the following three thermal spray processing technologies: the plasma spray process, the arc spray process, and the cold spray materials consolidation process. These processes lead to the successful layering of the three thermally sprayed copper surfaces upon an alloyed aluminum substrate that was consistent with the range of aluminum alloys commonly found in medical and hospital environments. Champagne et al. sought to test their hypothesis that the unique microstructures associated with pure copper arc sprayed, plasma sprayed, and cold sprayed coatings would achieve varied antimicrobial contact killing efficiencies and antimicrobial performance as a function of the resultant material microstructures that were unique to each of the three respective coating methodologies.

After examining the microstructures affiliated with each thermal spray methodology, Champagne et al. noted that "[differences] in microstructure are clearly evident, suggesting that differences in biological activity may also occur."[20] This observational statement was consistent with their early hypothesis. To pursue antimicrobial efficacy testing, the copper-coated and aluminum substrate bimetallic systems were inoculated with Methicillin-resistant *Staphylococcus aureus* (MRSA), then held at room temperature for two hours, wherein surviving bacteria were subsequently resuspended and cultured in a manner that was consistent with a relevant EPA protocol. Results showed that the plasma sprayed surface killed less than 90% of the exposed MRSA after two hours of exposure, while the cold sprayed copper killed more than 99.999% of the bacterial agent at the same timepoint (and potentially 100% of the inoculated MRSA, since the testing methods intrinsic limitation was surpassed), and the arc sprayed surface achieved a contact killing efficacy between the plasma sprayed and cold sprayed kill rates. Thus, the assertation that differences in biological activity would follow from the resulting differences in microstructures associated with each thermally sprayed surface held true.

Beyond a Proof-Of-Concept Demonstration

After Champagne et al. published their 2013 proof-of-concept study, the authors collaborated with Sundberg et al. in 2015 to study commercially pure copper cold spray deposited surfaces for the purpose of inactivating the *Influenza A* virus.[21] The collaborative effort attempted to showcase copper cold spray processed coatings' ability to thwart surface-contact fomite transmission of a viral pathogen. *Influenza A* was reportedly chosen since surface-contact fomite transmission may ensue 72 hours after a non-antiviral surface is exposed to the virus. Sundberg et al. went a step further by way of also varying the copper powder fed into the high-pressure cold spray system utilized to realize commercially pure copper cold spray coatings, which in one case contained the same microstructure ascertained in 2013, while a second copper cold spray coating garnered a nanostructured crystallinity via the use of spray-dried micrometric nanoparticle agglomerations.

Intriguingly, the nanostructured copper cold spray coating achieved a 99.3% decrease of infectious *Influenza A* virions after two hours of exposure (according to the previously mentioned and still relevant EPA protocol). In contrast with the nanostructured cold spray coating, the ultra-fine/fine-grained conventional copper cold spray surface, which was associated with the earlier findings from the MRSA study, accomplished a 97.7% reduction of infectious *Influenza A* pathogens; thus, attesting to the fact that Champagne et al.'s 2013 hypothesis, which asserts that the antimicrobial performance is a function of microstructure, also holds true for viral pathogens too. To highlight the von Mises mechanical flow stress distribution profile associated with a gas-atomized copper particle and aluminum substrate system and the microstructural attributes associated with such a single-particle and substrate combination, one may consider **Figure 2**, which is adapted from reference 22.

Thereafter, in 2019, Sundberg offered initial characterization and research that identified several material properties as being influential with respect to the antimicrobial efficacy of pure copper cold spray surfaces in a doctoral dissertation, which was publicly defended and presented at Worcester Polytechnic Institute.[23] Nevertheless, Champagne et al. sustained their examination of copper cold spray surface contact killing and/

(1) Length 1908 µm
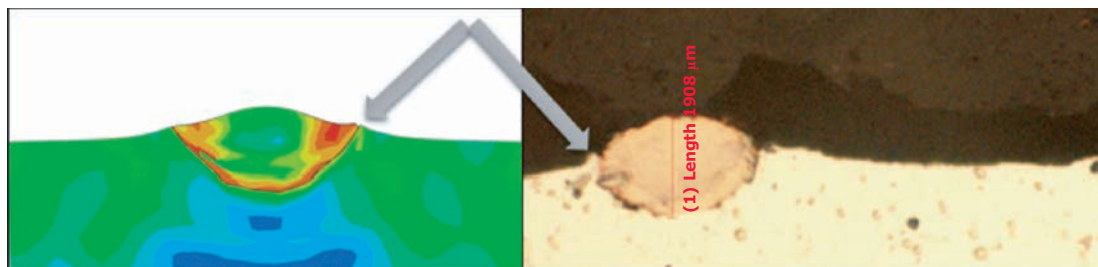
Figure 2. Finite element analysis simulation output impact morphology (**Left**) for a conventionally gas-atomized copper powder particle with the experimentally obtained single-particle impact morphology (**Right**).

or inactivation efficacies by summarizing their 2013 to 2019 findings in order to substantiate their second hypothesis that the dislocation density generated by cold spray consolidation processing of copper powder acts as the microstructural feature that is liable for the superior antipathogenic efficacies of cold sprayed surfaces relative to other manufacturing methods.[24] Stated otherwise, Champagne et al. conveyed dislocation density as the microstructural constituency most responsible for copper cold spray's coatings and consolidations antibacterial and antiviral behaviors.

However, a 2020 article by Sousa et al. presented an alternative microstructure-mediated mechanistic framework, which classified the surface area concentration of polycrystalline grain boundaries of the cold spray consolidated coated material as being more telling of the resultant surfaces' antimicrobial behavior than dislocation density alone.[25] Rather than disregarding dislocation density when formulating a mathematical relation for the effective copper ion diffusivity, wherein the copper microstructure with the greatest effective copper ion diffusivity corresponds with the most antipathogenic polycrystalline microstructure, Sousa et al. discovered "that the grain boundary contribution to the effective diffusivity of copper ions in the nanostructured material outperforms the diffusivity of dislocation pipe diffusion by an order of magnitude."[25] **Figure 3** builds upon the microstructural presentation provided in **Figure 2**, which was for a single particle deposit system, by way of capturing chemically etched multi-particle deposited cold

spray processed material consolidations when a similar gas-atomized copper feedstock was utilized (**Figures 3A** and **3B**) and the already mentioned spray-dried nanostructured agglomerate copper feedstock (**Figures 3C** and **3D**) was employed for antimicrobial/antiviral applications.[25]

Alternative Antipathogenic Cold Spray Considerations

At the same time, it behooves us to note that Rutkowska-Gorczyca studied the microstructure of a biocidal copper and titanium-dioxide composite surface built using low-pressure, rather than high-pressure, cold spray processing.[26] Before Rutkowska-Gorczyca published.[26] Sanpo et al. assessed a copper and zinc-oxide composite cold spray consolidated surface to facilitate microbial contact killing and the proscription of *C. marina* binding to maritime ship surfaces.[27] Outside of Sanpo et al.'s research, continued accumulation of data attests to the fact that direct surface contact between a microbe and a contact killing/inactivating copper surface plays a substantial part in capturing optimal antipathogenic efficacy.[28] Such substantiating data follows from scholarly demonstrations that surface topographies and surface roughness, as well as surface artifacts, tend to impact the biocidal, and in some cases viricidal, activities of a given antimicrobial surface.[29] Finally, from a point of view that was relevant to the healthcare and agricultural industries, El-Eskandrany et al. explored the use of a copper-containing ($Cu_{50}Ti_{20}Ni_{30}$) alloyed metallic glass powder particulate feedstock for antibacterial cold spray processing applications.[30]
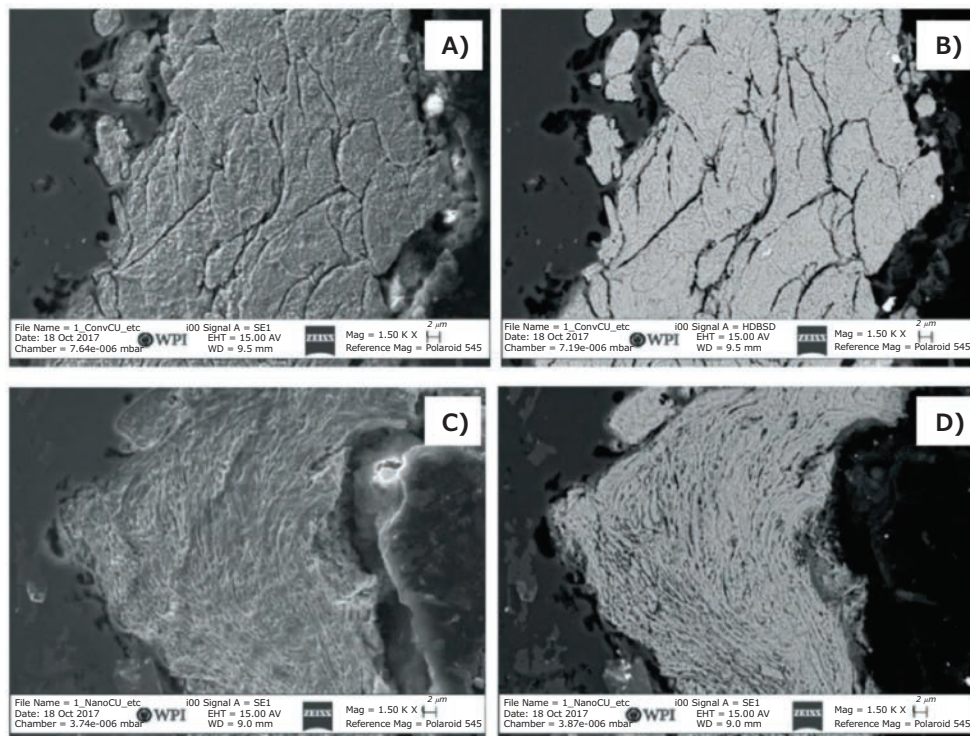
Figure 3. A) and B) presents SEM micrographs of cross-sectioned and etched consolidated conventional copper cold spray processed materials, whereas C) and D) presents SEM micrographs of cross-sectioned and etched nanostructured copper cold spray processed materials.

Inorganic Cold Spray Processing for the Energy Sector

Beyond the unique ability to functionalize cold spray material consolidations as biomaterials, cold spray processing has also enjoyed wider adoption beyond its original use as a nonstructural coating/restoration technology in various corners of the energy sector. In so far as nuclear energy, nuclear engineering, and nuclear materials are concerned, Maier et al. developed ceramic and metallic coatings to improve zirconium alloy cladding accident tolerances via oxidation-resistant inorganic material deposition.[31] Maier et al. optimized cold spray processing parameters (specifically, feedstock powder particle size, gas preheat temperature, carrier gas-temperature, and nozzle traverse speed) and achieved excellent particle-substrate adhesion and bonding of pure chromium (**Cat. No. 266299**), alloyed FeCrAl, and ceramic Ti_2AlC (**Cat. No. 910759**). The researchers also observed the fact that the coatings were able to "significantly mitigate oxidation kinetics… [via] high-temperature oxidation tests at temperatures up to 1300 °C." Along a similar line of inquiry, Maier et al. also found Ti_2AlC cold spray coatings, which were applied Zircaloy-4 (**Cat. No. BCR098**) fuel claddings, to have high hardness (800 Hk), fretting wear resistance, and wear/damage resistance, which are vital properties for proper rod insertion.[32]

Concerning the burgeoning field of energy storage, novel electrochemical materials development and battery-based research, cold spray has also been beneficial. Samuel et al. detailed the fabrication of TiO_2 (**Cat. No. 718467**) and reduced graphene oxide (**Cat. No. 900561**) surfaces via kinetic/cold spray for use as an anode in lithium ion batteries.[33] An array of similar research to that reported upon by Samuel et al. has continued to be published as of late. From the vantage point of additively manufacturing high-performance battery pack enclosures for enhanced electric vehicle safety and battery pack protection, Pal et al. identified cold spray consolidated enclosures as having improved resistance to total maximum deformation (59.49% relative to a bulk aluminum enclosure) while also achieving a 63% reduction in geometrical mass.[34] In addition to the anodes described by Samuel et al., the publication of Birt et al.'s patent application details how to manufacture cathodes and electrodes via cold spray processing.[35]

Cold Spray Deposition for Military/Aerospace Applications

Arguably, the most successful implementation of cold spray as a mainstream processing technique has been in military and aerospace applications. In these industries, cold spray applications serve as a repair technique for damaged components exposed to highly corrosive or erosive environments. Often, these components face extreme service conditions, such as high-speed cyclic motions or elevated humidity levels, which can quickly degrade the component's properties. For example, magnesium and magnesium alloys are often utilized in U.S. Army helicopter transmission gearboxes due to their low density and high structural integrity. However, magnesium is a relatively electrochemically active metal, thus

necessitating the need for frequent repair of these gearboxes due to corrosion damage. Fortunately, a coating of commercially pure aluminum was found to be able to be applied using cold spray wherein sufficient adhesion, density, and corrosion resistance was achieved, allowing for the subsequent use of the repaired gearboxes.[36] In another situation, which was reported by the U.S. Navy, an aluminum alloy (Al 6061) valve actuator often experienced severe exfoliation and corrosion pitting damage, which would have been unrepairable under normal circumstances. However, after utilizing high-pressure cold spray to deposit an Al 6061 coating over the damaged areas, these valve actuators were successfully repaired and re-implemented back into service.[37]

Part repair by cold spray processing is also used in applications where wear-resistant coatings are necessary, such as U.S. Army gun barrel liners. Due to the aggressive expansion of propellant gases, these liners erode quickly and require a wear-resistant coating to ensure optimum part lifetime and performance. Tantalum and tantalum alloys, among other refractory metals, have most recently been used as coatings in these gun barrel liners, which have replaced the previously used carcinogenic and environmentally hazardous chromium coatings.[38] To properly illustrate the use of cold spray additive manufacturing and materials consolidation in the defense sector one may consider **Figures 4A** and **4B**, where **Figure 4A** "depicts an example of a hollow cylinder with end cap manufactured by joining Ni-Al composite at the US Army Research Laboratory" and **Figure 4B** "shows a complex-shaped bracket developed by the United Technologies Research Center," according to an open-access review article by Pathak et al.[39]

While directly repairing previously unserviceable parts is an industrial goal associated with cold spray technology, the cold spray processing technique can also be used as a method of preventative maintenance too. For instance, a titanium alloy (Ti-3Al-2.5V) hydraulic aircraft tube that is known to frequently experience chafing from harsh vibrations and abrasions, which requires costly maintenance in time and labor. As a preventative solution to mitigate these traditional losses, commercially pure titanium sacrificial coatings have been used in wear-prone regions, which require far less effort to maintain.[6] In addition to preventative maintenance, there are newer and more novel applications of cold spray surfacing with a broader array of material systems. For example, the use of carbon fiber reinforced plastic (CRFP) in aircraft fuselages are utilized due to CRFP's extremely high strength-to-weight ratio. However, to withstand frequent lightning strikes in service, CRFP containing fuselages need an electrically conductive surface coating; thus, cold spray processing has been explored as a surface metallization technique for CRFP components using commercially pure aluminium.[40] This survey of past literature is by no means a comprehensive list of the innovative and impactful applications of cold spray in defense and aerospace industries — it is the present authors' goal for this survey to merely serve as a spotlight on exciting instances wherein cold spray has been established as a successful means of part repair and restoration in the military and aerospace sectors.
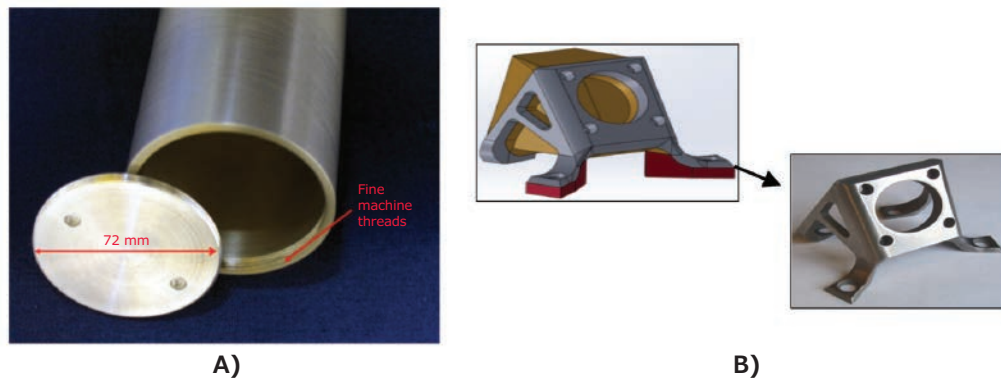
Figure 4. Micrographs of **A**) a hollow cylinder with end cap produced by cold spray; **B**) a bracket produced by cold spray. Reprinted with permission from reference 39, copyright 2012 Marcel Dekker Inc.

Concluding Remarks and Future Outlook

In this review, the authors have introduced the solid-state material deposition, additive manufacturing, and consolidation technology known as cold gas-dynamic spray, or simply cold spray. Recent work has accelerated the adoption of cold spray as an inorganic coating process in the biomedical, energy, defense, and aerospace industries, to name a few. The survey of past literature in this review is by no means a comprehensive list of the innovative and impactful applications of cold spray — rather, it is the authors' goal for this review to merely serve as a spotlight on exciting instances where cold spray has already been established as a successful coating process. However, it is the authors' belief that cold spray processing deserves attention in future research efforts to expand upon its existing uses, capabilities, and fundamentally scientific foundations.

As for cold spray's future outlook, the technology remains ripe for extended application and continued optimization given cold spray's relative youth as a deposition-based processing method. A promising avenue for future cold spray experimentation is in radiation shielding applications. Already, cold sprayed aluminum-based composite coatings have been used for their neutron shielding capabilities in high-radiation environments.[41] With the pervasiveness of space exploration and advancements in nuclear technology, robust material repair and consolidation techniques, such as cold spray, are needed in these intense settings. Regarding other extreme environments, one may also consider underwater part repair and restoration via cold spray. Novel spray procedures are being developed for *in-situ* repair of underwater structures, resulting in reduced maintenance cost and coatings of similar quality to those fabricated under conventional conditions.[42] Other modifications to processing conditions may be used with the cold spray, including environments with very low pressures. Successful processing of titanium-based nanoparticles at relatively low temperatures has already been achieved under vacuum conditions, which would not have been possible with conventional cold spray setups.[43] This may be a promising approach to future cold spray experimentation with nanoparticles, given the recent relevance of nanomaterials and nanotechnology research within the wider STEM communities.

While new applications of cold spray processing may be pursued, it is also imperative to improve upon the current processes utilized. More recently, robotic path planning has become more frequently emphasized in order to obtain optimal spray paths for improved deposition and part characteristics. Modeling the effects of precise tool configurations prior to the spray operation has allowed researchers to produce coatings of controlled thickness and surface quality not otherwise achievable.[44] Further implementation of advanced robotic systems in cold spray may assist the process' expansion beyond solely a coating technology into the realm of near net-shape part production. Researchers have also leveraged the power of machine learning techniques to predict processing success based on the initial conditions. Specifically, researchers have applied machine learning to spray trajectory planning, reducing material waste and improving geometric control of the final part profile as a result.[45,46] As artificial intelligence and machine learning are developing and becoming more ubiquitous in materials science and manufacturing, cold spray may benefit from further integration with these modeling techniques in order to lead towards process optimization. In fact, the current manuscripts authors recently demonstrated the way in which powder flowability classification via machine learning can be utilized for cold spray additive manufacturing feedstock analysis.[47] That said, given such considerations, the authors truly believe inorganic material deposition via cold spray processing remains prime for continued attention by the research community and continued applicability within the applied sciences and engineering communities.

References

(1) Gibson, I.; Rosen, D.; Stucker, B. *Additive Manufacturing Technologies*; Springer: New York, **2015**.

(2) Horn, T.; Harrysson, O. *Sci. Prog.* **2012**, *95* (3), 255–282. doi: 10.3184/003685012X13420984463047.

(3) Wycisk, E.; Solbach, A.; Siddique, S.; Herzog, D.; Walther, F.; Emmelmann, C. *Phys. Procedia* **2014**, *56*, 371–378. doi: 10.1016/j.phpro.2014.08.120.

(4) Kim, F. H.; Moylan, S. P. "Literature review of metal additive manufacturing defects," Gaithersburg, MD, May 2018.

(5) Papyrin, A. N. *Cold Spray Technology*. Elsevier, Amsterdam **2007**.

(6) Villafuerte, J. Ed., *Modern Cold Spray*. Cham: Springer International Publishing, **2015**.

(7) Sousa, B. C.; Walde, C.; Champagne, V.; Cote, D. *Int. J. Metall. Met. Phys.* **2020**, *5* (1). doi: 10.35840/2631-5076/9250.

(8) Sousa, B. C.; Gleason, M. A.; Haddad, B.; Champagne, V. K.; Nardi, A. T.; Cote, D. L. *Metals* **2020**, *10* (9), 1195–1265. doi: 10.3390/met10091195.

(9) Belsito, D. "Application of Computational Thermodynamic and Solidification Kinetics to Cold Sprayable Powder Alloy Design," Worcester Polytechnic Institute, **2014**.

(10) Champagne, V. K. "Investigation of the Effect of Oxides on the Critical Impact Velocity during the Cold Spray Process of High Purity Aluminum Powder," Worcester Polytechnic Institute, **2018**.

(11) Schmidt, T.; Gärtner, F.; Assadi, H.; Kreye, H. *Acta Mater*. **2006**, *54* (3), 729–742. doi: 10.1016/j.actamat.2005.10.005.

(12) Li, C.-J.; Wang, H.-T.; Zhang, Q.; Yang, G.-J.; Li, W.-Y.; Liao, H. L. *J. Therm. Spray Technol*. **2010**, *19* (1–2), 95–101. doi: 10.1007/s11666-009-9427-x.

(13) Ang, A. S. M.; Berndt, C. C.; Cheang, P. *Surf. Coatings Technol.* **2011**, *205* (10), 3260–3267. doi: 10.1016/j.surfcoat.2010.11.045.

(14) Schmidt, T.; Gaertner, F.; Kreye, H. *J. Therm. Spray Technol*. **2006**, *15* (4), 488–494. doi: 10.1361/105996306X147144.

(15) Lupoi, R. *Surf. Eng.* **2014**, *30* (5), 316–322. doi: 10.1179/1743294413Y.0000000214.

(16) Hassani-Gangaraj, M.; Veysset, D.; Champagne, V. K.; Nelson, K. A.; Schuh, C. A. *Acta Mater.* **2018**, *158*, 430–439. doi: 10.1016/j.actamat.2018.07.065.

(17) Fukumoto, M.; et al. *J. Therm. Spray Technol*. **2007**, *16* (5–6), 643–650. doi: 10.1007/s11666-007-9121-9.

(18) Stoltenhoff, T.; Borchers, C.; Gärtner, F.; Kreye, H. *Surf. Coatings Technol.* **2006**, *200* (16–17), 4947–4960. doi: 10.1016/j.surfcoat.2005.05.011.

(19) Stoltenhoff, T.; Kreye, H.; Richter, H. J. *J. Therm. Spray Technol.* **2002**, *11* (4), 542–550. doi: 10.1361/105996302770348682.

(20) Champagne, V. K.; Helfritch, D. J. *J. Biol. Eng.* **2013**, *7* (1), 8. doi: 10.1186/1754-1611-7-8.

(21) Sundberg, K.; Champagne, V. K.; McNally, B.; Helfritch, D.; Sisson, R. D. J. *Biotechnol. Biomater.* **2015**, *5* (4). doi: 10.4172/2155-952X.1000205.

(22) Sundberg, K.; et al. *J. Therm. Spray Technol.* **2020**, doi: 10.1007/s11666-020-01093-8.

(23) Sundberg, K. "Application of Materials Characterization, Efficacy Testing, and Modeling Methods on Copper Cold Spray Coatings for Optimized Antimicrobial Properties," Worcester Polytechnic Institute, **2019**.

(24) Champagne, V.; Sundberg, K.; Helfritch, D. *Coatings* **2019**, *9* (4), 257. doi: 10.3390/coatings9040257.

(25) Sousa, B. C.; Sundberg, K. L.; Gleason, M. A.; Cote, D. L. *Crystals* **2020**, *10* (6), 504. doi: 10.3390/cryst10060504.

(26) Rutkowska-Gorczyca, M. *Mater. Sci. Technol.* **2020**, 1–5., doi: 10.1080/02670836.2020.1738069.

(27) Sanpo, N.; Tharajak, J. *Appl. Mech. Mater.* **2016**, *848*, 23–26. doi: 10.4028/www.scientific.net/AMM.848.23.

(28) Bleichert, P.; Espírito Santo, C.; Hanczaruk, M.; Meyer, H.; Grass, G. *BioMetals* **2014**, *27* (6), 1179–1189. doi: 10.1007/s10534-014-9781-0.

(29) Selvamani, V. et al. *Adv. Mater. Interfaces* **2020**, *7* (7), 1901890. doi: 10.1002/admi.201901890.

(30) El-Eskandrany, M. S.; Al-Azmi, A. *J. Mech. Behav. Biomed. Mater.* **2016**, *56*, 183–194. doi: 10.1016/j.jmbbm.2015.11.030.

(31) Maier, B.; et al. *JOM* **2018**, *70* (2), 198–202. doi: 10.1007/s11837-017-2643-9.

(32) Maier, B. R.; Garcia-Diaz, B. L.; Hauch, B.; Olson, L. C.; Sindelar, R. L.; Sridharan, K. *J. Nucl. Mater.* **2015**, *466*, 712–717. doi: 10.1016/j.jnucmat.2015.06.028.

(33) Samuel, E.; et al. *J. Alloys Compd.* **2017**, *715*, 161–169. doi: 10.1016/j.jallcom.2017.04.308.

(34) Pal, S. K.; Singh, S.; Singh, H.; Le Phung, M. L.; Yooyen, S.; Sleesongsom, S. *Energy Storage* **2020**, *2* (3), e148. doi: 10.1002/est2.148.

(35) A. M. Birt and D. Apelian, "Kinetic Batteries," US 2018/0138494 A1, **2018**.

(36) Champagne, V. K. *J. Fail. Anal. Prev.* **2008**, *8* (2), pp. 164–175. doi: 10.1007/s11668-008-9116-y.

(37) Widener, C. A.; et al. *J. Therm. Spray Technol.* **2016**, *25* (1–2), 193–201. doi: 10.1007/s11666-015-0366-4.

(38) Trexler, M. D.; Carter, R.; de Rosset, W. S.; Gray, D.; Helfritch, D. J.; Champagne, V. K. *Mater. Manuf. Process.* **2012**, *27* (8), 820–824. doi: 10.1080/10426914.2011.648690.

(39) Pathak, S.; Saha, G. *Coatings* **2017**, *7* (8), 122. doi: 10.3390/coatings7080122.

(40) Affi, J.; Okazaki, H.; Yamada, M.; Fukumoto, M. *Mater. Trans.* **2011**, *52* (9), 1759–1763. doi: 10.2320/matertrans.T-M2011807.

(41) N. H. Tariq et al. *Surf. Coat. Technol. 2018*, *339* (15), 224–236. doi: 10.1016/j.surfcoat.2018.02.007.

(42) Liu, Y.; Li, C.; Huang, X.-F.; Ma, K.; Luo, X.-T.; Li, C. *Appl. Surf. Sci.* **2020**, *506*, 144542. doi: 10.1016/j.apsusc.2019.144542.

(43) Fan, S. Q.; Yang, G. J.; Li, C. J.; et al. *J Therm Spray Tech* **2006**, *15*, 513–517. doi: 10.1361/105996306X146901.

(44) Kout, A.; Müller, H. *Adv. Eng. Softw.* **2009**, *40* (10), 1078–1086.

(45) Ikeuchi, D.; Vargas-Uscategui, A.; Wu, X.; King, P.C. *Materials* **2019**, *12*, 2827.

(46) Aggour, K., Gupta, V., Ruscitto, D., Ajdelsztajn, L., Bian, X., Brosnan, K., Vinciquerra, J. *MRS Bulletin* **2019**, *44* (7), 545–558. doi:10.1557/mrs.2019.157

(47) Valente, R. et al., "Classifying Powder Flowability for Cold Spray Additive Manufacturing Using Machine Learning," 2020, 2nd International Workshop on Big Data Tools, Methods, and Use Cases for Innovative Scientific Discovery, IEEE BigData Conference. https://www.researchgate.net/publication/345675096_Classifying_Powder_Flowability_for_Cold_Spray_Additive_Manufacturing_Using_Machine_Learning.

Copper and Copper Alloy Powders

Name	Form	Max. Part. Size	Cat. No.
Copper-tin alloy	spherical powder	−200 mesh	**520365-1KG**
Copper-silver alloy, Cu98Ag2	powder	45 µm	**GF10388763-1EA**
Silver-copper alloy, Ag72Cu28	powder (alloy pre-cursor)	45 µm	**GF06395351-1EA**
Silver-zirconium-copper alloy, Ag97Zr2Cu1	powder (atomized)	45 µm	**GF08673677-1EA**
Copper-tin alloy, Cu80Sn20	powder	53 µm	**GF75211837-1EA**
Copper-titanium alloy, Cu56.4Ti43.6	powder	45 µm	**GF14757655-1EA**
Copper-titanium alloy, Cu70Ti30	powder	45 µm	**GF12988615-1EA**
Copper-titanium alloy, Cu90Ti10	powder	45 µm	**GF59732590-1EA**
Copper-zirconium alloy, Cu87Zr13	powder	45 µm	**GF77196044-1EA**
Copper	powder (spheroidal)	10 - 25 µm	**326453-250G** **326453-1KG**

Aluminum, Aluminum Alloys, and Alumina Powders

Alumina Powders

Name	Form	Particle Size (mesh)	Cat. No.
Aluminum oxide	powder	~150	**267740-250G** **267740-1KG** **267740-5KG**
	fused powder	-325	**342688-100G** **342688-1KG**

Aluminum

Name	Form	Particle Size (μm)	Purity	Cat. No.
Aluminum	powder	particle size <5	99.5% trace metals basis	**653608-5G**
	powder	<75	≥99.95% trace metals basis	**202584-10G**
	powder	max. part. size 15	99%	**GF01392050-1EA**
	powder	max. part. size 60	99.9%	**GF04572750-1EA**
	powder	max. part. size 25	99%	**GF29119877-1EA**
	powder	max. part. size 15	99%	**GF41304899-1EA**
	powder	max. part. size 60	99.9%	**GF48562465-1EA**
	powder	max. part. size 25 (micron)	99%	**GF59664572-1EA**
	powder	max. part. size 15 (micron)	99%	**GF82061670-1EA**
	powder	max. part. size 60 (micron)	99.9%	**GF95119847-1EA**
	powder	max. part. size 60 (micron)	99.9%	**GF96256604-1EA**

Aluminum Alloys

Name	Form	Max. Part. Size (μm)	Cat. No.
Zirconium-aluminum alloy, Zr90Al10	powder	45	**GF11331863-1EA**
Aluminum-magnesium alloy, Al92.1Mg7.9	powder (alloy pre-cursor)	63	**GF66065452-1EA**
Titanium-aluminum alloy, Ti88Al12	powder	150	**GF22319557-1EA**

Zinc Powders for Cold Spray

Name	Form	Particle Size (μm)	Purity	Cat. No.
Zinc	powder	max. part. size 5	-	**GF09783018-1EA**
	powder	mean particle size 7.5	98.8%	**GF20413718-1EA**
Zinc oxide	powder	particle size <5	99.9%	**205532-100G** **205532-1KG** **205532-5KG**

Iron and Steel Alloys for Cold Spray

Name	Form	Particle Size (μm)	Cat. No.
Iron-Chromium-Molybdenum alloy, Fe81Cr16Mo3	powder	max. part. size 45	**GF18826140-1EA**
Iron-Nickel alloy, Fe50Ni50	powder	max. part. size 45	**GF66807300-1EA**
Stainless Steel - AISI 304 alloy, FeCr18Ni10	powder	max. part. size 45	**GF02863841-1EA**
Stainless Steel - AISI 316 alloy, FeCr18Ni10Mo3	powder	max. part. size 45	**GF87616851-1EA**
Stainless steel - AISI 316l	powder	mean particle size 3	**GF30719471-1EA**
	powder	max. part. size 45 (micron)	**GF83597204-1EA**
Stainless Steel - AISI 316L alloy, FeCr18Ni10Mo3	powder	max. part. size 3	**GF68846552-1EA**
Stainless steel - AISI 347	powder	max. part. size 45 (micron)	**GF94677733-1EA**
Stainless Steel - AISI 347 alloy, FeCr18Ni10Nb	powder (atomized)	max. part. size 45	**GF36444999-1EA**
Stainless Steel - AISI 410 alloy, FeCr12.5	powder	max. part. size 45	**GF64171694-1EA**
Iron-Chromium-Aluminum alloy, Fe81Cr16Al3	powder	max. part. size 45	**GF69474606-1EA**

Titanium Powders for Cold Spray

Name	Form	Particle Size (μm)	Cat. No.
Titanium	powder	max. part. size 75 (micron)	**GF78028421-1EA**
Cobalt-titanium alloy, Co94Ti6	powder	max. part. size 45	**GF48942692-1EA**
Molybdenum-titanium alloy, Mo80Ti20	powder	max. part. size 45	**GF91863355-1EA**
Molybdenum-titanium alloy, Mo90Ti10	powder	max. part. size 45	**GF26337427-1EA**
Niobium-titanium alloy, Nb56Ti44	powder	max. part. size 45	**GF03489419-1EA**
Titanium bronze alloy, Ti75Cu25	powder	max. part. size 45	**GF51218636-1EA**
Titanium-aluminum alloy, Ti65Al35	powder	max. part. size 75	**GF41193615-1EA**
Titanium-aluminum alloy, Ti78Al22	powder	max. part. size 75	**GF15249214-1EA**
Titanium-aluminum-vanadium alloy, Ti90Al6V4	powder	max. part. size 45	**GF99149484-1EA**
Titanium-chromium alloy, Ti80Cr20	powder	max. part. size 75	**GF26445001-1EA**
Tungsten-titanium alloy, W95Ti5	powder	max. part. size 45	**GF52543683-1EA**
Titanium	powder	avg. part. size <45	**366994-10G** **366994-50G**

Nickel Powders for Cold Spray

Name	Form	Particle Size (µm)	Purity	Cat. No.
Nickel	powder	max. part. size 45	≥99.5%	GF00232816-1EA
	powder	mean particle size 3 - 7 (FSSR)	99.8%	GF38925557-1EA
	powder	max. part. size 45 (micron)	≥99.5%	GF69412170-1EA
Nickel-molybdenum alloy, Ni84Mo16	powder	max. part. size 45	-	GF95579252-1EA
Nickel	powder	<50	99.7% trace metals basis	266981-100G 266981-500G

Tantalum Powders

Name	Form	Particle Size	Purity	Cat. No.
Tantalum	powder	−325 mesh	99.9% trace metals basis	262846-25G 262846-100G
	powder	mean particle size 1 - 3 µm (FSSR)	99.9%	GF52623738-1EA
	powder	max. part. size 75 (micron)	99.9%	GF84769453-1EA

Cobalt Powders

Name	Form	Particle Size	Purity	Cat. No.
Cobalt	powder	max. part. size 45 µm	99.8%	GF06340597-1EA
Cobalt(II) oxide	powder	−325 mesh	-	343153-10G 343153-100G
Cobalt(II,III) oxide	powder	<10 µm	-	221643-50G 221643-250G
Cobalt-titanium alloy, Co94Ti6	powder	max. part. size 45 µm	-	GF48942692-1EA
Cobalt-tungsten alloy, Co50W50	powder	max. part. size 45 µm	-	GF63788079-1EA
Cobalt	powder	particle size 2 µm	99.8% trace metals basis	266639-25G 266639-100G 266639-500G

For Cold Spray

Name	Form	Size	Purity	Cat. No.
Boron carbide	powder	<10 µm	98%	378119-50G
Tricalcium phosphate	powder	4 µm	-	900205-50G
Hydroxyapatite	powder	-	-	900195-50G
	powder	10 µm	-	900203-50G
	powder	5 µm	-	900204-50G
Carbon nanotube, single-walled	powder (freeze-dried)	average diameter 0.83 nm	≥90% carbon basis (≥77% as carbon nanotubes)	704121-250MG 704121-1G
	powder (freeze-dried)	average diameter 0.78 nm	≥95% carbon basis (≥95% as carbon nanotubes)	773735-250MG 773735-1G
	powder or flakes	-	<1% (ash) ≥98% carbon basis	900711-5G
	powder	-	>99%, TGA (carbon content, EDX) ≥93%, TGA (carbon as SWNT by TEM)	901634-25G
Carbon nanotube, multi-walled	powder	-	>90% carbon basis	659258-2G 659258-10G
	powder	-	>98% carbon basis	698849-1G
Carbon nanotube, double-walled	powder	-	50-80% carbon basis	637351-250MG 637351-1G
Polyethylene	powder	particle size 40 - 48 µm	-	434272-100G 434272-500G
Zirconium(IV) oxide-yttria stabilized	powder	particle size <100 nm	-	544779-25G